Studies of Influence of Compositional Modification on Electrical and Optical Properties of Inorganic Materials

Makoto KUMATORIYA

2012

Contents

General Introduction

1. Objectives of this study

Over the last several decades, inorganic materials have been extensively researched and developed for electronics and photonics [1,2]. Particular focus has been placed on applications such as generation [3-7], filtering [8-12], detection [13-17], amplification [18,19], modulation [20-24], conversion [25-28] and so on. Accordingly, many oxide single crystals have been investigated along with other materials.

In general, because oxide single crystals and ceramics [29] are both inorganic materials, they have been concurrently developed for electrical and optical instruments as they have complementary properties. For electrical and optical applications, the dielectric [30-33], ferroelectric [34-36], piezoelectric [37,38], pyroelectric [39-42], electro-optical [43-48], nonlinear optical [49-52], and magnetic [53-55] properties of these materials have been improved by their modification. Conventional methods for improvements include researching new materials, developing new synthetic processes, partially substituting the existing material with other elements, and so on.

Ceramics offer greater freedom and flexibility in terms of material design and modification. Typical examples incorporating ceramic materials include capacitors [56-58], piezoelectric [37,59,60], and ferrite materials [53]. Most materials for capacitors and piezoelectrics have the perovskite structure (Fig. 1), which is known to be the most versatile ceramic structure [61]. By appropriately modifying the composition, the electroceramic dielectric ($BaTiO_3$ and its relatives) phases can be

turned into metallic conductors and superconductors [62]. Consequently, significant numbers of studies on the application of these materials to actuators, sounders, transformers, sensors, resonators, and so on, have been undertaken. The composition of the perovskite material is expressed by the general formula ABO_3, where the A-site cation and B-site cation are located at the corners and center of the unit cell, respectively. A schematic illustration of the perovskite ABO_3 structure is presented in Fig. 1.

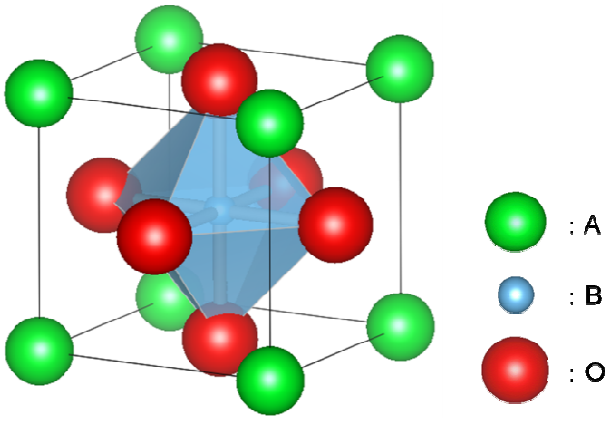

Fig. 1 Schematic illustration of the perovskite ABO_3 structure.
The crystal structure was drawn with VESTA 3 [63].

Members of the perovskite family such as $SrTiO_3$, $CaTiO_3$, and $BaTiO_3$ readily form a solid solution with each other [61]; thus, in the case of these oxide single crystals, material modification is markedly more difficult than modification of ceramics. Modification of oxide single crystals is more difficult than that of ceramics because of certain requirements, including segregation of impurities, congruent melting, and thermal management of crystal growth.

Crystal growth is a three-dimensional atomic arrangement toward a generation of a solid substance by a heterogeneous or homogeneous chemical process in a solid phase, a liquid phase, or a gas phase. It is also generated in their phases individually or in combination. Various types of crystal growth techniques have been developed, depending upon the chemical process involved and the phase equilibriums. All crystal growth processes can be broadly classified according to the scheme presented in Table 1 [64].

In the growth of a high quality and a large crystal, which is suitable for practical use, the liquid-solid method (shown in Table 1) is advantageous. The liquid-solid method is roughly classified into melt growth and solution growth. The melt growth is the process in which a chemical composition of the melt coincides with that of the target crystal (Namely the congruently melting composition). Accordingly, a degree of supercooling works as a driving force of crystallization in the melt growth. The control of thermal environment in the growing system is much important during a crystal growth. The melt growth is widely used for commercial single crystals of semiconductors, metals, oxides, fluorides and so on. Many crystal growth techniques [65] such as Czochralski method [66,67], Bridgeman method [68,69], and Verneuil method [70-72] have been developed in several decades. The melt growth is one of the most popular methods with growing large crystal at relatively high growth rate. The solution growth is also widely used for not only commercial single crystals but also material research, foods, and so on. Solution growth can be used for crystals with incongruent melt composition. The disadvantages of the solution growth, which compared with the melt growth, are lower growth rate and smaller crystal size. In the solution growth, a degree of slow cooling and supersaturation work as driving forces of

crystallization. The solution growth is classified into some solution methods such as a top-seeded solution growth method and Kyropoulos method [73-76], a hydrothermal method [77,78], and a flux method such as a liquid phase epitaxy method and a traveling solvent method [79-81].

Table 1 Classification of crystal growth processes [64]

1. Solid-Solid	Solid	T →	Solid
			Devitrification Strain annealing Polymorphic phase change Precipitation from solid solution
2. Liquid-Solid			
i) Melt growth	Molten material	Dec. T →	Crystal
			Bridgman-Stockbarger Kyropoulos Czochralski Zoning Vernuil
II) Flux Growth	Solid(s)+ Flux agent(s)	Dec. T →	Crystal(s)
iii) Solution growth	Sold(s) + Solvent	Low T →	Crystal(s)
			Evaporation Slow cooling Boiling solutions
iv) Hydrothermal growth	Solid(s)+ Solvent	High T High p →	Crystal(s)
			Hydrothermal sintering Hydrothermal reactions Normal temperature gradient Reversed temperature gradient Boiling solutions Reversed temperature gradient Boiling solutions
v) Gel growth	Solution + Gel medium	Low T →	Crystal
			Reaction Complex decomplex Chemical Reduction Solubility reaction Counter-flow diffusion
	Solution	→	Crystal(s)
3. Gas-Solid	Vapor(s)	→	Solid
			Sublimation-condensation Sputtering Epitaxial processes Ion-implantation

Modification in chemical composition such as solid solution, cation doping, and cation substitution is important for single crystal to improve its physical properties. However, it is more difficult for the melt growth to control chemical composition except for crystal growth from a congruent composition. The main problem is inhomogeneity of cation distribution in a crystal. Mateika et al. measured the distribution coefficient, k_0 for each cation in garnet crystals and perovskite crystals [82,83]. The distribution coefficient defined as the ratio (Eq. (1)) of the cation concentration in the crystal (C_s) to its concentration in the melt (C_l).

$$k_0 = \frac{C_s}{C_l} \quad (1)$$

They showed that the ionic radii of the guest ions as well as their concentration act an important role in the optimization of the distribution coefficient. It is also important for growing a homogeneous crystal to optimize the melt composition, to choice appropriate guest cations and to choice appropriate growth method.

Over the last decades, photoinduction phenomena in transparent materials generated by ultrashort laser pulses, such as femtosecond laser pulses, and the application of these phenomena to microprocessing have received considerable attention. When a femtosecond laser pulse is focused inside the bulk of a transparent material, the intensity in the focal volume can become high enough to cause absorption through nonlinear processes, inducing to modification in the material. Because the absorption is strongly nonlinear, this modification can be localized in the focal volume inside the material. Recently, various three-dimensional optics such as waveguides [84], gratings [85] and couplers [86] have been fabricated inside various transparent materials using this method. In this way, the modification of inorganic materials using ultrashort laser

pulses is also an expectable method to improve physical properties without destruction of crystal structure.

This study focuses on approaches for the chemical modification of inorganic materials by crystal growth techniques and ultrashort pulse laser processing to improve physical properties of inorganic materials.

2. Organization of the dissertation

In Chapter 1, three important technologies that relate to this thesis are reviewed. The first two technologies are concerned with crystal growth: one is the Czochralski method, which is one of the most suitable and widely applied methods for the production of crystalline materials for electrical and optical components, while the other is a modified Czochralski method with continuous material supply. The third technology involves femtosecond laser pulses. This technology differs from the others but is a powerful tool for the modification of transparent materials.

In Chapter 2, the substitution of Al into $La_3Ga_5SiO_{14}$ (langasite) is described. The development of langasite as a new piezoelectric material fifteen years ago represented a significant advancement. For example, it satisfied the need for a material with a larger electromechanical coupling factor and lower temperature coefficient of frequency for surface acoustic wave (SAW) devices. Currently, langasite is still used in a variety of applications [87]. Al-substituted langasite-type crystals recently attracted attention as a material with significant heat resistance.

In Chapter 3, another approach for the chemical modification of crystals is introduced. Lithium tantalate, $LiTaO_3$, is one of the best ferroelectric crystalline

materials. It is widely used for piezoelectric, pyroelectric, electro-optical, and nonlinear optical applications. Although the $LiTaO_3$ phase has a wide solid-solution range, high-quality crystals can only be grown for commercial use at the congruent melting composition (i.e., Li: 48.5 mol% and Ta: 51.5 mol%). In this chapter, homogeneous and large crystal growth of $LiTaO_3$ with non-congruent composition and the resultant optical properties are described.

Chapter 4 describes the use of a femtosecond laser to modify transparent materials such as single crystals. Here, the direct writing of waveguides in $LiTaO_3$ using a femtosecond laser is described. Applications for the waveguides formed in $LiTaO_3$ are also proposed.

References

[1] H. J. Scheel, in *Crystal Growth Technology*, edited by H. J. Scheel and T. Fukuda (Wiley, West Sussex, 2003), p. 3

[2] I. Sunagawa, in *50 years Progress in Crystal*, edited by R. S. Feigelson (Elsevier, Amsterdam, 2004), p. 35.

[3] S. H. Gold and G. S. Nusinovich, Rev. Sci. Instrum., **68**, 3945 (1944).

[4] P. A. Franken, A. E. Hill, C. W. Peters, and G. Weinreich, Phys. Rev. Lett., **7**, 118 (1961).

[5] D. P. Devor, I. J. D'Haenens, and C. K. Asawa, Phys. Rev. Lett., **8**, 432 (1962).

[6] R. C. Miller, Phys. Rev. A, **134**, 1313 (1964).

[7] K. Mizuuchi, K. Yamamoto, and K. Kato, Electron. Lett, **33**, 806 (1997).

[8] R. Aigner, Proc. IEEE Int. Ultrason. Symp., **8**, 582 (2008).

[9] D. P. Morgan, Proc. IEEE Int. Freq. Control Symp., 439 (1998).

[10] R. Weigel, D. P. Morgan, J. M. Owens, A. Ballato, K. M. Lakin, K. Hashimoto, and C. C. Ruppel, IEEE Trans. Microwave Theory Tech., **50**, 738 (2002).

[11] R. Aigner, J. Ella, H. J. Timme, and L. Elbrecht, Int. Electron. Devices Meeting Digest., 897 (2002).

[12] K. M. Lakin, IEEE Microwave Magazine **4**, 61 (2003).

[13] F. Caruso, E. Rodda, D. N. Furlong, K. Niikura, and Y. Okahata, Anal. Chem., **69**, 2043 (1997).

[14] J. F. Alder and J. J. McCallum, Analyst, **108**, 1169 (1983).

[15] C. Fredriksson, S. Kihlman, M. Rodahl, and B. Kasemo, Langmuir, **14**, 248 (1998).

[16] K. Arshak, E. Moore, G. M. Lyons, J. Harris, and S. Clifford, Sensor Rev., **24**, 181 (2004).

[17] C. K. O'Sullivan and G. G. Guilbault, Biosens. Bioelectron., **14**, 8 (1999).

[18] I. Baumann, S. Bosso, R. Brinkmann, R. Corsini, M. Dinand, A. Greiner, K. Schafer, J. Sochtig, W. Sohler, H. Suche, and R. Wessel, IEEE J. Select. Topics Quantum Electron., **2**, 355 (1996).

[19] D. Andreou, Opt. Commun., **27**, 171 (2002).

[20] E. L. Wooten, K. M. Kissa, A. Yi-Yan, E. J. Murphy, D. A. Lafaw, P. F. Hallemeier, and D. Maack, IEEE J. Select. Topics Quantum Electron., **6**, 69 (2000).

[21] I. P. Kaminow and W. M. Sharpless, Appl. Phys., **6**, 351 (1967).

[22] I. P. Kaminow, IEEE Trans. Microwave Theory Tech., **23**, 57 (1975).

[23] R. C. Alferness, IEEE Trans. Microwave Theory Tech., **30**, 1121 (1982).

[24] M. N. Armenise, IEE Proc., **135**, 85 (1988).

[25] K. Suizu and K. Kawase, IEEE J. Select. Topics Quantum Electron., **14**, 295 (2008).

[26] K. S. Rao and K. H. Yoon, J. Mater. Sci., **38**, 391 (2003).

[27] X. F. Cao, R. V. Ramaswamy, and R. Srivastava, J. Lightwave Technol., **10**, 1302 (1992).

[28] J. F. Lam and H. W. Yen, Appl. Phys. Lett., **45**, 1172 (1984).

[29] J. Rödel, A. B. N. Kounga, M. Weissenberger-Eibl, D. Koch, A. Bierwisch, W. Rossner, M. J. Hoffmann, R. Danzer, and G. Schneider, J. European Ceram. Soc., **29**, 1549 (2009).

[30] X. M. Chen, Y. Suzuki, and N. Sato, J. Mater. Sci., **5**, 244 (1994).

[31] M. T. Sebastian, J. Mater. Sci., **10**, 475 (1999).

[32] H. Kagata, T. Inoue, J. Kato, and I. Kameyama, Jpn. J. Appl. Phys., **31**, 3152 (1992).

[33] H. Ogawa and A. Kana, J. Eur. Ceram. Soc., **23**, 2485 (2003).

[34] W. Cochran, Adv. Phys., **9**, 387 (1960).

[35] R. E. Cohen, Nature, **358**, 136 (1992).

[36] G. H. Haertling, J. Am. Ceram. Soc., **82**, 797 (1999).

[37] T. Tanaka, Ferroelectrics, **40**, 167 (1982).

[38] A. BaIlato, Proc. IEEE Int. Freq. Control Symp., 575 (1996).

[39] R. W. Whatmore, Rep. Prog. Phys., **49**, 1335 (1986).

[40] C. B. Roundy and R. L. Byer, J. Appl. Phys., **44**, 929 (1973).

[41] S. W. Choia, R. T. R. Shrouta, S. J. Janga, and A. S. Bhallaa, Ferroelectrics **100**, 29 (1989).

[42] M. Okuyama, Y. Togami, Y. Hamakawa, M. Kimata, and S. Uematsu, Sens. Act., **16**, 263 (1989).

[43] A. Yariv and P. Yeh, *Optical Waves in Crystals* (Wiley, New York, 1984), p. 220.

[44] J. E. Geusic, S. K. Kurtz, L. G. V. Uitert, and S. H. Wemple, Appl. Phys. Lett., **4**, 141 (1964).

[45] J. J. Amodei and D. L. Staebler, Appl. Phys. Lett., **18**, 540 (1971).

[46] J. D. Bierlein and C. B. Arweiler, Appl. Phys. Lett., **49**, 917 (1986).

[47] L. Xu, X.-C. Zhang, and D. H. Auston, Appl. Phys. Lett., **61**, 1784 (1992).

[48] Q. Wu and X. C. Zhang, Appl. Phys. Lett., **68**, 1604 (1996).

[49] R. W. Bond, *Nonlinear Optics*, 2nd ed. (Acadmic Press, New York, 2003), p.

67.

[50] D. F. Eaton, Science **253**, 281 (1991).

[51] V. I. Malinovski, S. V. Mednikov, L. A. Shuvalov, B. I. Sturman, and T. R. Volk, Ferroelectrics, **39**, 1209 (1990).

[52] Y. Furukawa, K. Kitamura, S. Takekawa, K. Niwa, and H. Hatano, Opt. Lett., **23**, 1892 (1998).

[53] A. Goldman, *Modern Ferrite Technology* (Springer, New York, 2006), p. 217.

[54] R. C. Booth and E. A. D. White, J. Phys. D, **17**, 579 (1984).

[55] J. Lenz and S. Edelstein, IEEE Sensors J., **6**, 631 (2006).

[56] Y. Sakabe, Curr. Opin. Solid State Mater. Sci., **2**, 584 (1997).

[57] E. C. Subbaraoa, Ferroelectrics, **35**, 143 (1981).

[58] H. Kishi, Y. Mizuno, and H. Chazono, Jpn. J Appl. Phys., **42**, 1 (2003).

[59] J. G. Gualtieri, J. A. Kosinski, and A. Ballato, IEEE Trans. Ultrason. Ferroelectr. Freq. Control, **41**, 53 (1991).

[60] A. Ballato, IEEE Trans. Ultrason. Ferroelectr. Freq. Control, **42**, 916 (1995).

[61] A. S. Bhalla, R. Guo, and R. Roy, Mater. Res. Innovations, **4**, 3 (2000).

[62] A. J. Moulson and J. M. Herbert, *Electroceramics*, 2nd ed. (Wiley, West Sussex, 2003), p. 135.

[63] K. Momma and F. Izumi, J. Appl. Crystallogr., **44**, 1272 (2011).

[64] G. Dhanaraj, K. Byrappa, V. Prasad, and M. Dudley, in *Handbook of Crysatl Grwoth* edited by G. Dhanaraj, K. Byrappa, V. Prasad, and M. Dudley (Springer, Berlin, 2010), p. 7.

[65] H. J. Scheel, J. Cryst. Growth, **211**, 1 (2000).

[66] J. Czochralski, Z. Phys. Chem., **92**, 219 (1917).

[67] H. Li and J. Xu, in *Springer Handbook of Crystal Growth*, edited by G. Dhanaraj, K. Byrappa, V. Prasad, and M. Dudley (Splinger, Berlin, 2010), p. 479.

[68] A. G. Petrosyan, J. Cryst. Growth, **139**, 372 (1994).

[69] D. Schulz, S. Ganschow, D. Klimm, M. Neubert, M. Roßberg, M. Schmidbauer, and R. Fornari, J. Cryst. Growth, **296**, 27 (2006).

[70] R. E. D. L. Rue and F. A. Halden, Rev. Sci. Instrum., **31**, 35 (1960).

[71] F. A. Halden and R. Sedlacek, Rev. Sci. Instrum., **34**, 622 (1963).

[72] R. W. Bartlett, F. A. Halden, and J. W. Fowler, Rev. Sci. Instrum., **38**, 1313 (1967).

[73] V. Belruss, J. Kalnajs, A. Linz, and R. C. Folweiler, Mater. Res. Bull., **6**, 899 (1971).

[74] M. H. Garrett and I. Mnushkina, J. Cryst. Growth, **166**, 550 (1996).

[75] K. Polgár, L. Kovács, G. Corradi, and Z. Szaller, J. Cryst. Growth, **177**, 211 (1997).

[76] D. Rytz, B. A. Wechsler, C. C. Nelson, and K. W. Kirby, J. Cryst. Growth, **99**, 864 (1990).

[77] F. Iwasaki and H. Iwasaki, J. Cryst. Growth, **237-239**, 820 (2002).

[78] R. A. Laudise, E. D. Kolb, and A. J. Caporaso, J. Am. Ceram. Soc., **47**, 9 (1964).

[79] J. W. Nielsen and E. F. Dearborn, J. Phys. Chem. Solids, **5**, 202 (1958).

[80] W. Tolksdorf, J. Cryst. Growth, **3-4**, 463 (1968).

[81] B. M. Wanklyn, J. Mater. Sci., **7**, 813 (1972).

[82] D. Mateika, E. Völkel, and J. Haisma, J. Cryst. Growth, **102**, 994 (1990).

[83] D. Mateika, H. Kohler, H. Laudan, and E. Völkel, J. Cryst. Growth, **109**, 441 (1991).

[84] K. M. Davis, K. Miura, N. Sugimoto, and K. Hirao, Opt. Lett., **21**, 3 (1996).

[85] N. Takeshima, Y. Narita, S. Tanaka, Y. Kuroiwa, and K. Hirao, Opt. Lett., **30**, 3 (2005).

[86] W. Watanabe, T. Asano, K. Yamada, K. Itoh, and J. Nishii, Opt. Lett., **28**, 3 (2003).

[87] H. Takeda, S. Tanaka, S. Izukawa, H. Shimizu, T. Nishida, and T. Shiosaki, Proc. IEEE Ultrason. Symp., **1**, 560 (2005).

Chapter 1.

Three Key Technologies for Modifying Composition of Crystals

1.1. Introduction

In this chapter, three important technologies that are related to this dissertation will be discussed to facilitate future reference in ensuing chapters. The first two technologies are concerned with crystal growth: one is the Czochralski method, which is the one of the most suitable and widely applied methods for the production of crystalline materials for electrical and optical components, while the other is a modified Czochralski method with continuous material supply. The third technology involves femtosecond laser pulses. This technology differs from the others, but is a powerful tool for the modification of transparent materials.

1.2. Crystal growth technology

1.2.1. Czochralski method

1.2.1.1 Growth technique

The Czochralski method [1] is a technique that involves crystal pulling from the melt. Currently, it is used to produce the majority of commercially available semi-conductive and oxide single crystals, such as Si, GaAs, sapphire, Nd:YAG, and $LiNbO_3$, for electrical and optical instruments. The process is based on a liquid-solid phase transition driven by a seed crystal in contact with the melt [2].

Fig. 1.1 shows a schematic diagram of the crystal growth apparatus for the Czochralski method. The furnace comprises a crucible, insulators, a heating source, and a pulling system. For oxide crystals, noble metals such as platinum or iridium are used for the crucible depending on the melting point of the oxides. The insulators that surround the crucible are commonly made of alumina-silica, pure alumina, or zirconia ceramics. The design of the hot zone, which is composed of these insulators, is very important for the stable growth of crystals because it determines the thermal ambience. In this study, induction heating was chosen as the heat source; induction heating uses an RF generator to produce current in a coil surrounding the crucible, which acts as a susceptor. To control the thermal gradient in the furnace, a tube made from noble metals is often used as an additional heater (i.e., an after-heater, as shown in Fig. 1.1) above the crucible.

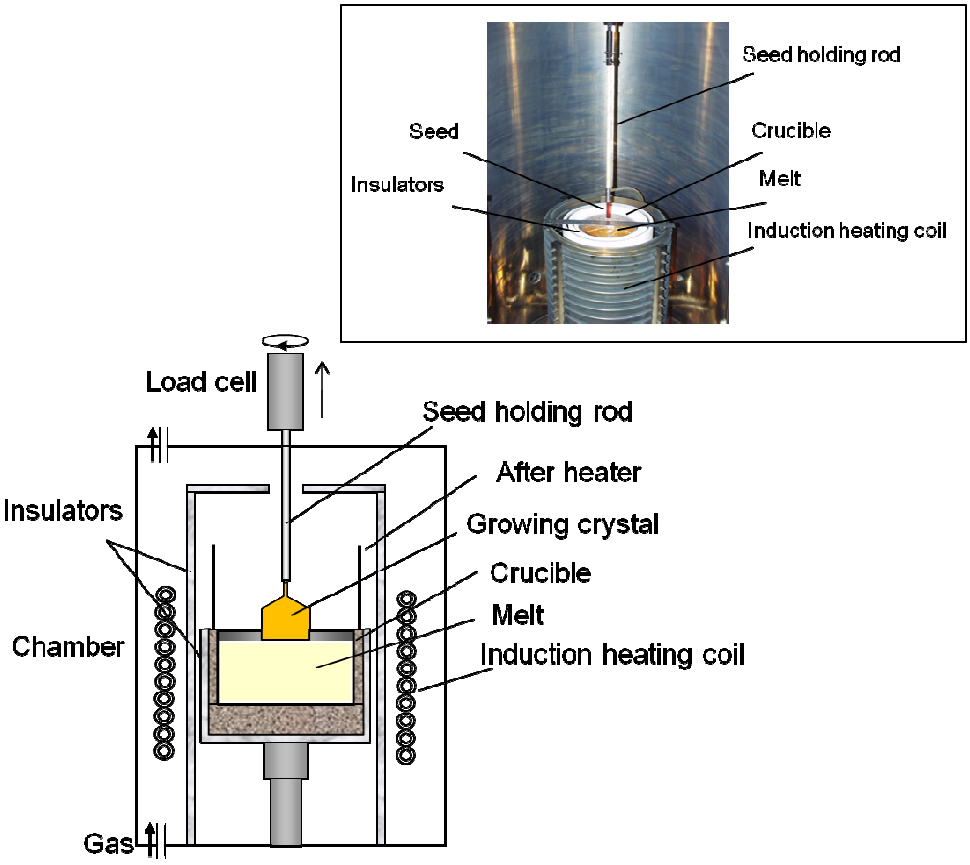

Fig. 1.1 Schematic diagram of the typical apparatus for the Czochralski technique.

There are three key process parameters for crystal growth: the pulling rate, the crystal rotation rate, and the thermal gradient. The pulling rate must be accurately controlled because it determines the growth rate of the diameter of the crystal, as shown in Eq. (1-1). Crystal rotation is necessary to prevent asymmetry in the temperature distribution and to control fluid flow in the melt.

Control of the diameter is required to obtain high-quality crystals [3]. The crystal diameter is automatically controlled by periodically monitoring the weight of the growing crystal using a load cell.

The ideal mass growth rate, G_{Grow}, is calculated using the following equation:

$$G_{Grow} = G_{Pull} \frac{0.25\pi\rho_{Melt}\rho_{Crystal}D_{Crucible}^2}{\rho_{Melt}D_{Crucible}^2 - \rho_{Crystal}D_{Crystal}^2} \quad (1\text{-}1)$$

where ρ_{Melt} and $\rho_{Crystal}$ are the melt and the crystal density, respectively, and $D_{Crucible}$ and $D_{Crystal}$ are the diameters of the crystal and crucible, respectively. To minimize the difference between the real mass growth rate and the weight increment, the heating power is regulated.

1.2.1.2 Solid–liquid interface control

All of the components of the crystal growth apparatus, such as the crucible and the insulators, are set up with the axis of symmetry being the seed axis, as shown Fig. 1.1. Crystal rotation during growth is required to grow a high-quality single crystal using the Czochralski growth process. The shape of the growth interface also influences the quality of the crystal.

Shape control of the growth interface was first reported by Cockayne et al. in 1968 [4]. They showed that under the proper conditions, the shape of the growth interface could be controlled via the crystal rotation rate.

Fig. 1.2 shows the schematics of typical flows observed in an oxide melt at various crystal rotation rates. The outer annular area consists of fluid flow driven by the natural convective forces of the heated fluid, whereas the main driving force for the inner area is convection driven by the rotating crystal. Fig. 1.3 shows the flow pattern that appeared on the melt surface of a $La_3Ga_5SiO_{14}$ crystal (described in Chapter 2) as a result of the conditions shown in Fig. 1.2 (b).

Fig. 1.4 shows the as-grown $La_3Ga_5SiO_{14}$ (langasite) crystal and its cross section, which was observed under polarized light. Fig. 1.4 (b) exhibits an example of the sudden melt back of the body part of a boule (indicated by the red arrow), which occurs as a result of the reversal of fluid flow due to crystal rotation [5].

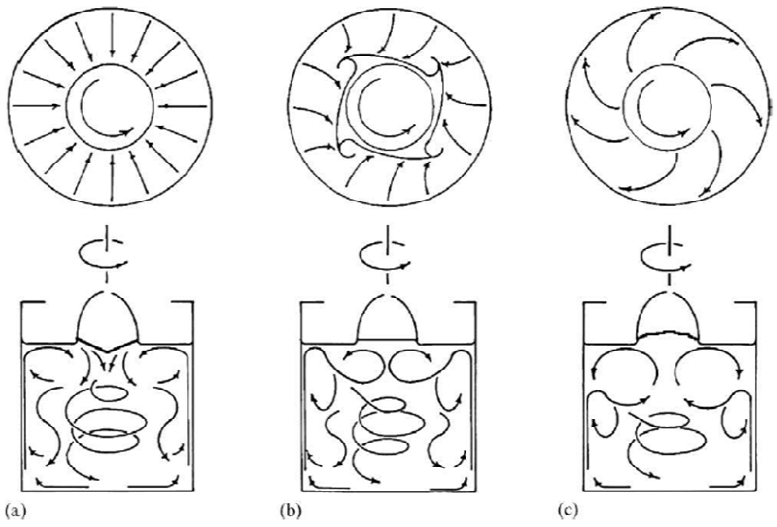

Fig. 1.2 Surface and bulk flow observed in water/glycerin simulations: (a) slow rotation, (b) moderate rotation, (c) fast rotation [6].

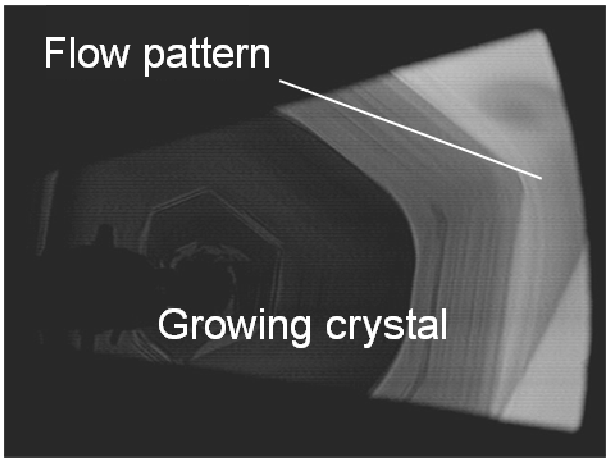

Fig. 1.3 Apparent flow pattern on the melt surface during growth of $La_3Ga_5SiO_{14}$ crystal (Chapter 2).

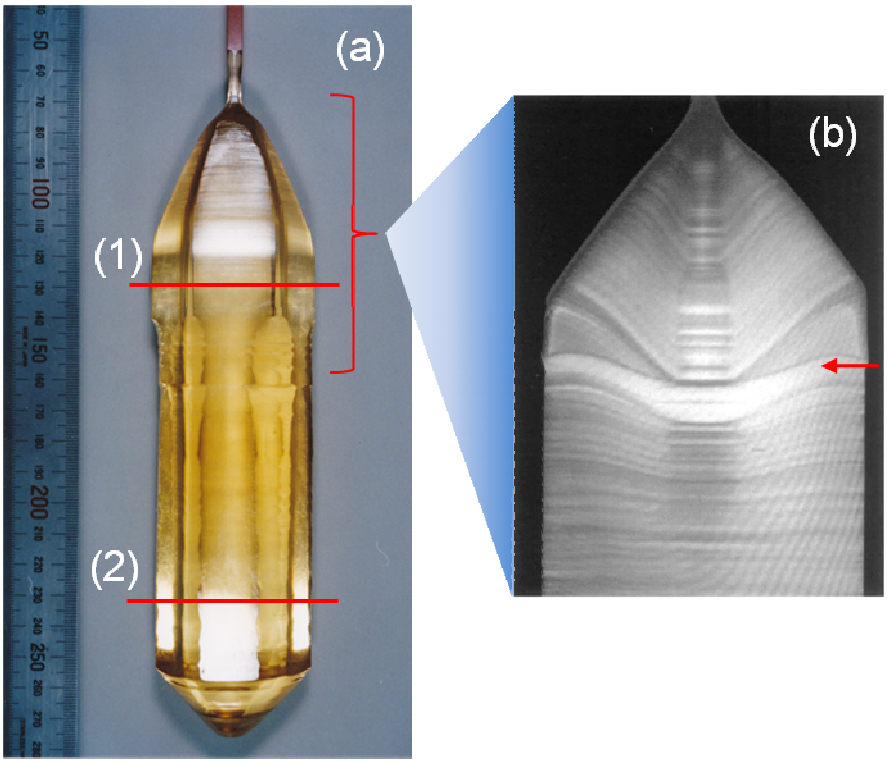

Fig. 1.4 (a) As-grown langasite crystal and (b) a cross-nicol image of $(2\bar{1}\bar{1}0)$ wafer cut from the body. (1) and (2) indicate the position of the wafers sampled for the X-ray topograph shown in Fig. 1.5. The scale of the ruler in Fig. 1.4 (a) is mm.

At the beginning of the body part of the crystal, as indicated by (1) in Fig. 1.4(a) (R_c = 10 rpm), the shape of the growth interface was convex to the melt. The resultant (0 0 0 1) wafer had a core dislocation of concentric circles, as shown in the X-ray topographic image in Fig. 1.5(1). The leaky surface acoustic wave (LSAW) velocity, which was measured using a line-focused beam acoustic microscope [7], was varied for 10 ms^{-1} on wafer (1); accordingly, the shape of the velocity distribution reflected a concentric form of core dislocation (Fig. 1.6(1)). When the R_c was accelerated to 19 rpm, the growth interface converted to concave with a concomitant decrease in the crystal weight. Subsequently, the interface gradually transformed into a flat shape. No core dislocation, and a homogeneous distribution of LSAW velocity were observed in the wafer that grew at a flat growth interface (Fig. 1.5(2) and Fig. 1.6(2)). It is very important for the quality of the crystal that a flat shape be maintained in the growth interface.

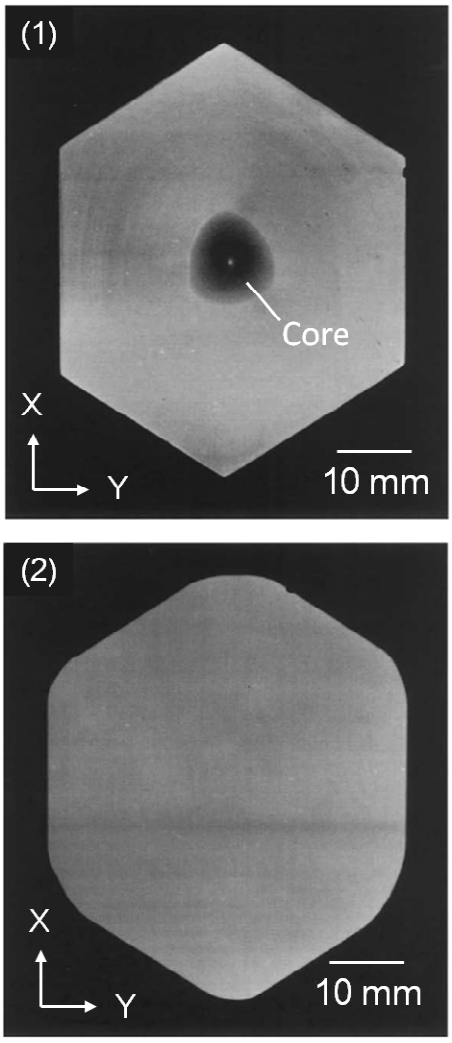

Fig. 1.5 X-ray topographic images of the (0 0 0 1) wafer: (1) cut from the beginning of the body part and (2) cut from the end of the body part shown in Fig. 1.4.

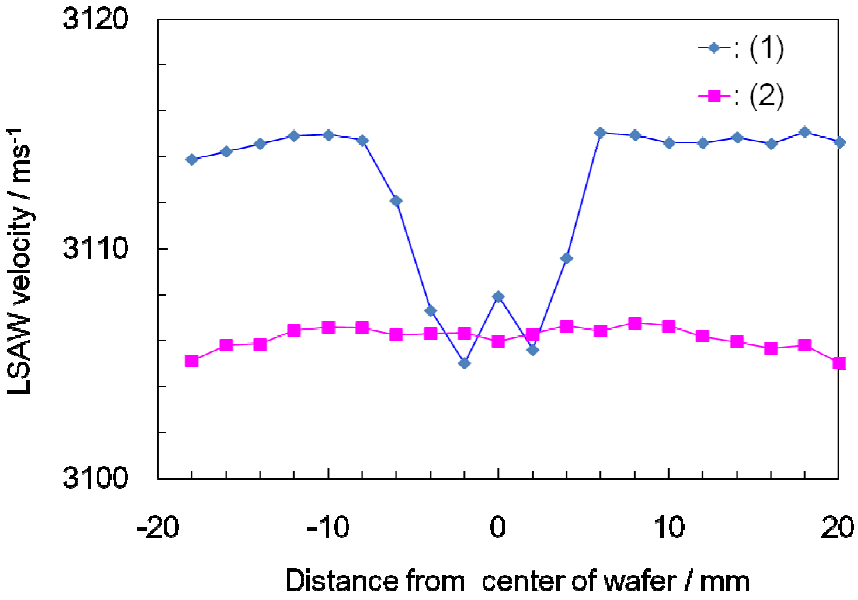

Fig. 1.6 Dependence of the LSAW velocity on the distance from the center of the (0 0 0 1) wafers cut from the boule in Fig. 1.3.

1.2.2. Modified Czochralski method

Congruent melting means that the liquidus and solidus curves merge at a single point of the temperature-composition phase diagram as shown in Fig. 1.7. This point is very important for the growth of high-quality crystals for commercial applications. If the composition melt is not congruent (i.e., off-congruent composition), the composition of the grown crystal will vary from the top to the end, as indicated in Fig. 1.7.

Alternatively, in a growing crystal with doping elements (or impurities), the concentration of doping agent in the crystal, C_S, is less than the concentration in the adjacent melt, C_L. The distribution coefficient, C_S/C_L, depends on the doping elements. Crystal growth by the Czochralski method results in an increased or decreased concentration of doping elements in the melt during the growth of the crystal. The concentration of impurities at any point along the length of the growing crystal is given by the following equation:

$$C = kC_0(1-g)^{k-1} \tag{1-2}$$

where k is the segregation coefficient, C_0 is the initial concentration of impurities in the melt, and g is the fraction of the total solidified melt. When $k \neq 1$, the concentration of impurities in the crystal is heterogeneous. For example, in the case of $k < 1$, C in Eq. (1-2) is approximately inversely proportional to the fraction remaining in the melt.

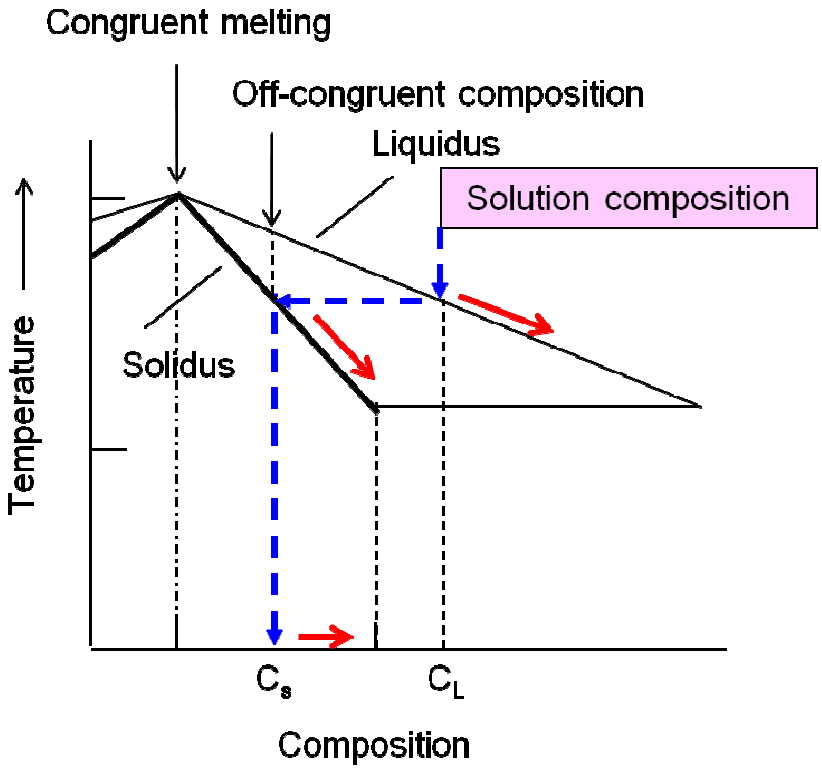

Fig. 1.7 Phase diagram of a binary compound with congruent melting.

A method for the growth of a homogeneous crystal with an off-congruent composition has been proposed [8]. The development of a practical oxide single crystal growth process was investigated by Kitamura et al. in 1992 [9]. They adopted a double-crucible Czochralski method (DC-CZ) and a continuous material charging technique to grow stoichiometric $LiNbO_3$.

The DC-CZ apparatus shown in Fig. 1.8 consists of three parts: a double crucible, an automatic powder supply system, and the Czochralski growth apparatus. Their descriptions are as follows:

(1) Double crucible: The crucible has a double chamber structure, i.e., it is composed of an inner cylindrical crucible and an outer crucible. The inner crucible is placed on the bottom of the outer crucible thereby dividing the outer crucible into two spaces. During growth, the melt in the outer crucible flows into the inner crucible through the bottom of the inner crucible.

(2) Material supply system: In this system, a granular material with the same composition as the crystal is placed in a holding container known as a hopper at the top of the apparatus (shown in Fig. 3.4). The granular material in the hopper is automatically supplied into the outer crucible at a rate equal to that of the mass growth rate during crystal growth.

(3) Growth apparatus: The growth apparatus is the same as that for the Czochralski method, as described above in Section 1.2.1.

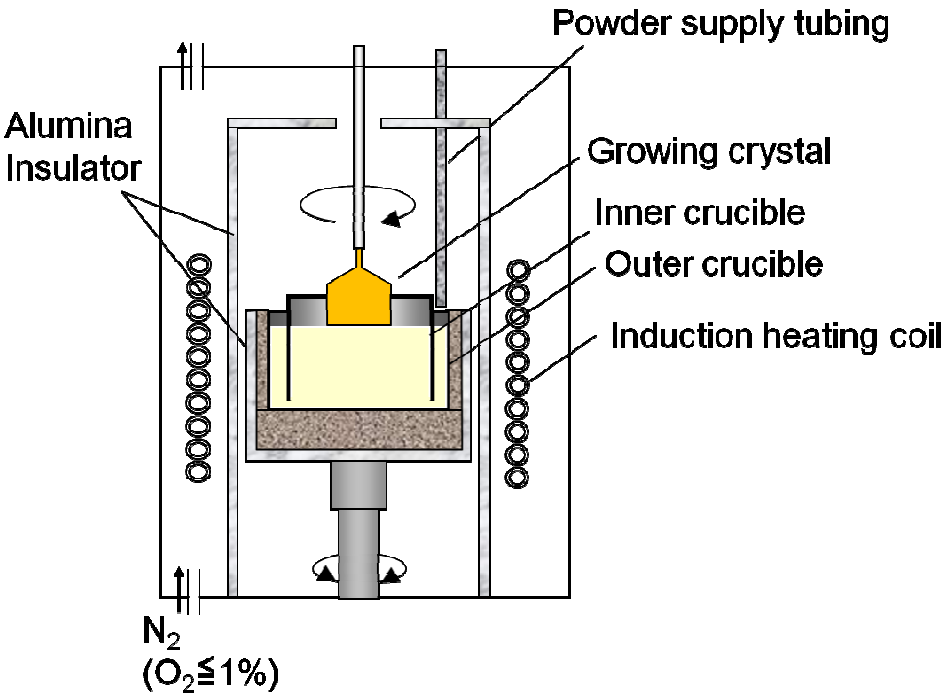

Fig. 1.8 Schematic of the apparatus for the modified Czochralski (DC-CZ) method with an automatic powder supply system.

1.3. Microstructure fabrication by femtosecond laser

Over the last decade, the construction of localized structural changes within a transparent material using ultra-short laser pulses has received considerable attention [10-13]. Due to the required high power density, the interaction of femtosecond laser beams with materials is mainly based on nonlinear optical processes such as multiphoton ionization. The multiphoton absorption process is characterized by a specific laser-power density threshold. For a focused beam with a Gaussian intensity profile, the heat-affected volume becomes smaller than the focus size when the laser fluence is at or just above the threshold value. Once the free-electron plasma is generated by multiphoton absorption and ionization reaches sufficient density, irreversible material breakdown and ablation begin. The electrons transfer energy to the ions and lattice and the material is heated to higher temperatures than it is when long pulses are used. Due to the very short pulse duration, heat diffusion to the surrounding material is negligible and a large fraction of the material in the small interaction volume rapidly vaporizes through the melt phase. When femtosecond laser pulses are used, the thickness of the melt layer is very small because most of the heated material reaches the vaporization temperature and there is rapid cooling due to the steep temperature gradient. Accordingly, a large amount of the absorbed laser energy is removed via direct vaporization. As a result, ablation and material removal is very precise, which contrasts the results using long pulses, and the ablated area is significantly smaller than the focused beam size. Fig. 1.9 shows the experimental set-up of the femtosecond laser processing system. The irradiation source employed was a regeneratively amplified 800 nm Ti-sapphire laser that emits 1 kHz or 250 kHz mode-locked pulses [14]. The average

laser-beam power at the sample location was controlled between 1 and 700 mW by neutral-density filters inserted between the laser and the microscope objective lens. A sample was put on an XYZ translation stage, which was controlled by a computer. Using the XYZ stage, the samples were transported at a rate of 10–1,000 $\mu m \cdot s^{-1}$ either parallel or perpendicular to the incident laser beam.

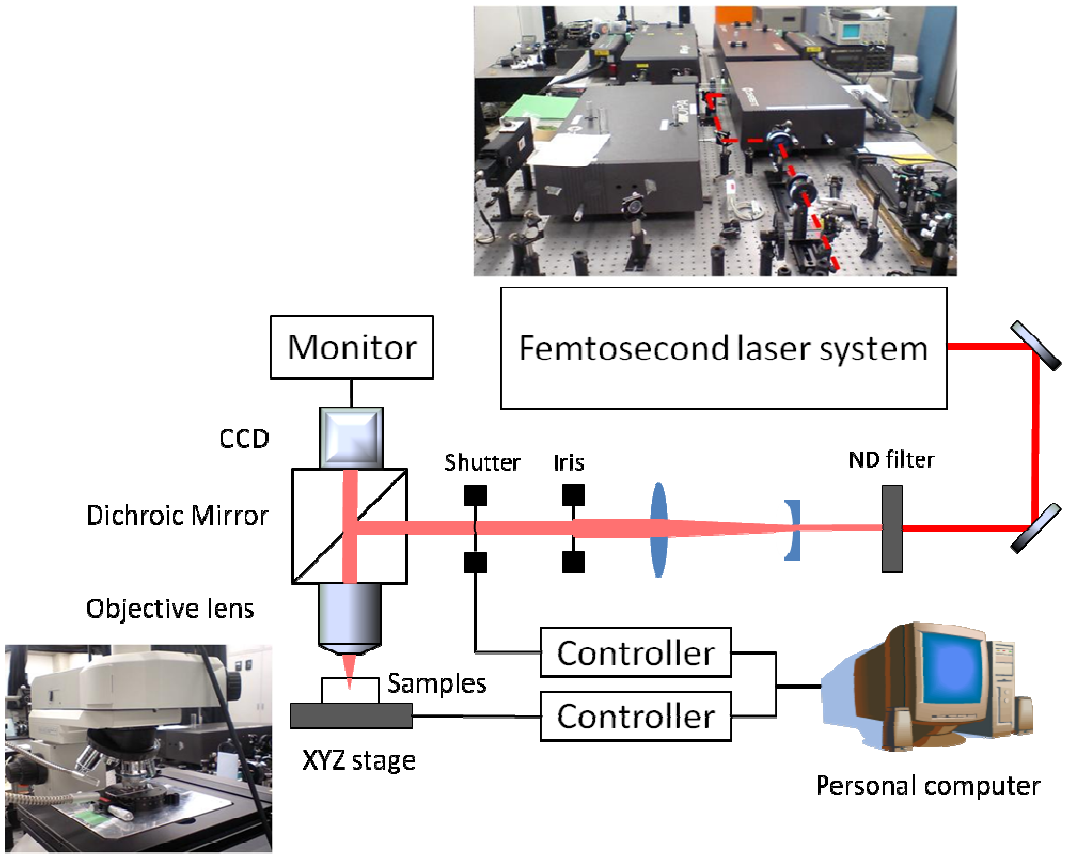

Fig. 1.9 Schematic diagram of the femtosecond laser processing system.

1.4. Conclusion

In this chapter, three important technologies that are related to this thesis were outlined to facilitate future reference in subsequent sections. This thesis focuses primarily on the composition control related to crystal growth. The first two technologies, a Czochralski method and the double-crucible Czochralski method with continuous material charging system, are widely applied methods for the production of crystalline materials. In the Czochralski method, control of the solid-liquid interface is one of the most important factors for growth of high-quality crystals. The high crystallographic quality and homogeneity of the sound velocity of a grown crystal having a flat interface shape was also demonstrated. Crystals with off-congruent compositions can be grown by the modified Czochralski method with continuous material supply. This method utilizes a continuous supply of granular material having a composition equivalent to the composition of the growing crystal. The third technology involves femtosecond laser pulses. This technology differs from the others, but is a powerful tool for the modification of transparent materials.

References

[1] J. Czochralski, Z. Phys. Chem., **92**, 219 (1917).

[2] E. Diéguez, J. L. Plaza, M. D. Aggarwal, and A. K. Batra, in *Handbook of Crystal Growth*, edited by G. Dhanaraj, Kullaiah Byrappa, V. Prasad, and M. Dudley (Springer, Berlin, 2010), p. 245.

[3] D. T. J. Hurle, J. Cryst. Growth, **42**, 473 (1977).

[4] B. Cockayne, M. Chesswas, and D. B. Gasson, J. Mater. Sci., **3** (1968).

[5] K. Takagi, T. Fukazawa, and M. Ishii, J. Cryst. Growth, **32**, 89 (1976).

[6] C. D. Brandle, J. Cryst. Growth, **42**, 400 (1977).

[7] J. Kushibiki and N. Chubachi, IEEE Trans. Sonics Ultrason., **32**, 189 (1985).

[8] W. F. Leverton, J. Appl. Phys., **29**, 1241 (1958).

[9] K. Kitamura, J. K. Yamamoto, N. Iyi, S. Kirnura, and T. Hayashi, J. Cryst. Growth, **116**, 327 (1992).

[10] D. Du, X. Liu, G. Korn, J. Squier, and G. Mourou, Appl. Phys. Lett., **64**, 3071 (1994).

[11] C. B. Schaffer, A. Brodeur, and E. Mazur, Meas. Sci. Technol., **12**, 1784 (2001).

[12] E. A. Stach, V. Radmilovic, D. Deshpande, A. Malshea, D. Alexander, and D. Doerr, Appl. Phys. Lett., **83**, 3 (2003).

[13] G. A. Torchia, P. F. Meilán, A. Rodenas, D. Jaque, C. Mendez, and L. Roso, Opt. Express, **15**, 13266 (2007).

[14] P. M. W. French, Rep. Prog. Phys., **58**, 169 (1995).

Chapter 2.

Crystal Growth and Electromechanical Properties of Al-Substituted Langasite ($La_3Ga_{5-x}Al_xSiO_{14}$)

2.1. Introduction

The use of mobile communication equipment has rapidly expanded worldwide. The next generation of advanced digital communication systems will need to operate at higher frequencies and have wider bandwidths and higher bit rates. To fulfill these requirements, new materials must be developed for electrical devices. As an example, surface acoustic wave (SAW) devices require a material with a large electromechanical coupling factor and a low temperature coefficient of frequency, which would be favorable for miniaturizing the devices and improving the flexibility in designing a SAW device.

Along with $Li_2B_4O_7$, langasite ($La_3Ga_5SiO_{14}$; LGS) is one of the most attractive single crystals of the recognized potential piezoelectric materials [1,2]. It was determined that LGS has planes with suitable orientations that exhibit good SAW performance. For example, the electromechanical coupling factor of LGS is about three times larger than that of quartz, and its temperature dependence of frequency is also stable.

The langasite crystal lattice comprises four kinds of sublattices that are represented as $\{E\}_3[A](F)_3\langle D\rangle_2O_{14}$. The most interesting aspect of the material design of this structure is improving its piezoelectricity through substitution with other metal ions.

The effective replacement of an E site with an alkaline earth (i.e., Ba or Sr), and of an A site with a group 5 metal (i.e., Ta or Nb) have already been reported [3]. In these studies, an improvement of the piezoelectricity was predicted via substitution with an element that enlarges the crystal lattice size. Because Al and Ga are homologous elements, it is possible to substitute Ga with Al without such compensation. Al substitution is expected to elucidate the intrinsic effect of lattice size on piezoelectricity. However, there are no reports on the crystal growth of Al-substituted LGS ($La_3Ga_{5-x}Al_xSiO_{14}$; LGAS) and the effects of Al substitution on the piezoelectric properties. Accordingly, this chapter describes the growth of LGAS crystals using a Czochralski method and compares the piezoelectric properties of LGAS with those of LGS.

2.2. $Ca_3Ga_2Ge_4O_{14}$-type structure

Langasite, $La_3Ga_5SiO_{14}$, is isostructural with $Ca_3Ga_2Ge_4O_{14}$ [4], which was discovered first. Both of these mixed-oxides belong to the trigonal system and have a space group of P321. The langasite crystal lattice is composed of four kinds of cation sites, which are represented as $\{E\}_3[A](F)_3\langle D\rangle_2O_{14}$. The schematic projections of an $\{E\}_3[A](F)_3\langle D\rangle_2O_{14}$-type structure are shown in Fig. 2.1 and Fig. 2.2. The physical properties of $La_3Ga_5SiO_{14}$ are also shown in Table 2.1. In this chemical formula, $\{E\}$ and $[A]$ respectively represent a decahedral (i.e., twisted Thomson cube) site coordinated by eight oxygen atoms, and an octahedral site coordinated by six oxygen atoms. Both (F) and $\langle D\rangle$ represent tetrahedral sites coordinated by four oxygen atoms, although the $\langle D\rangle$ site is slightly smaller than the (F) site. In the case of langasite, the $\{E\}$ site is occupied by La^{3+}, the $[A]$ site is occupied by Ga^{3+}, the (F) site is occupied

by Ga^{3+}, and the ⟨D⟩ site is occupied by Ga^{3+} and Si^{4+} as shown in Fig. 2.1 [5].

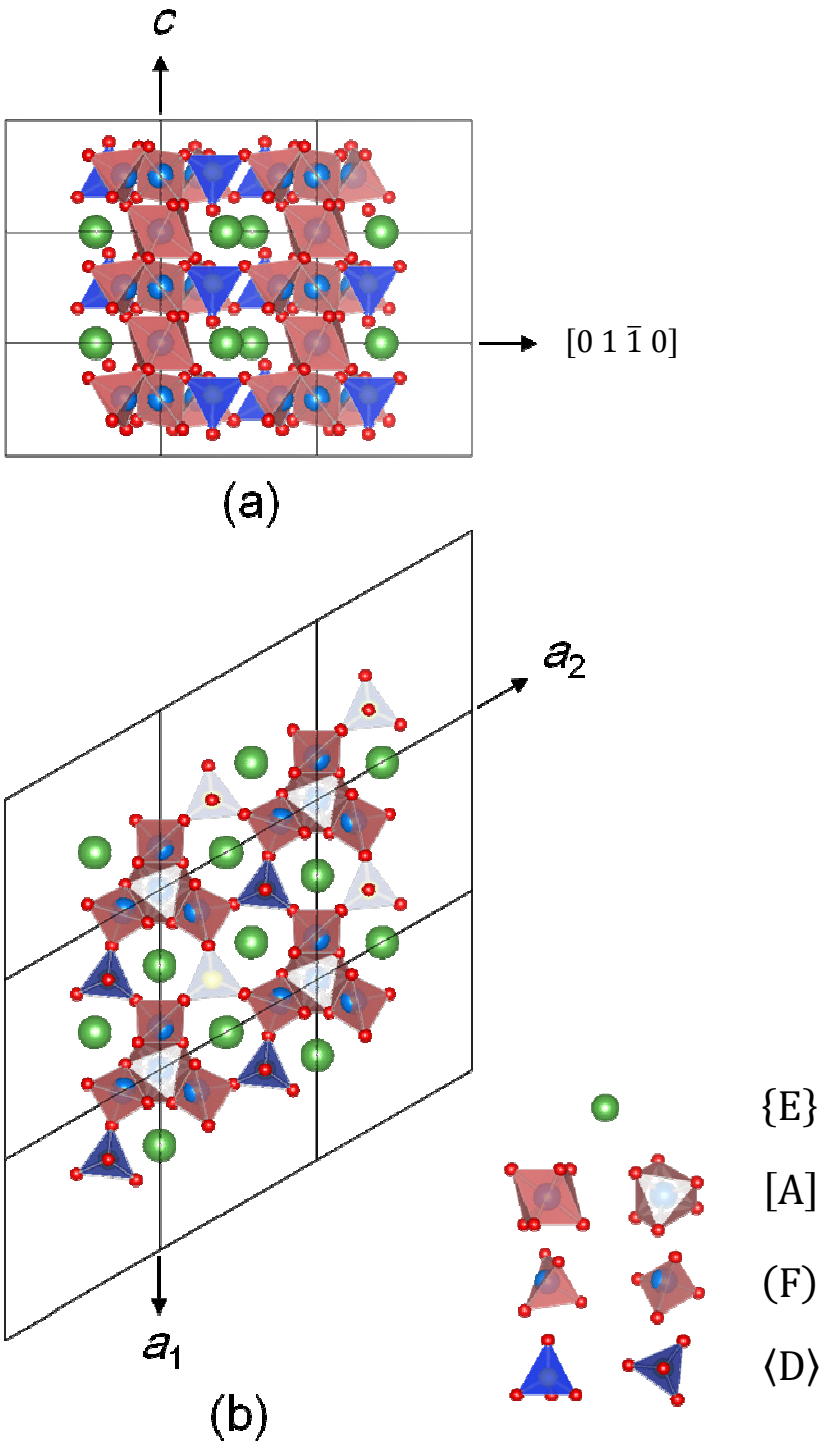

Fig. 2.1 Schematic illustrations of an $\{E\}_3[A](F)_3\langle D\rangle_2O_{14}$-type structure viewed along the (a) [0001] and (b) [2110] directions. The crystal structures were drawn with VESTA 3 [6].

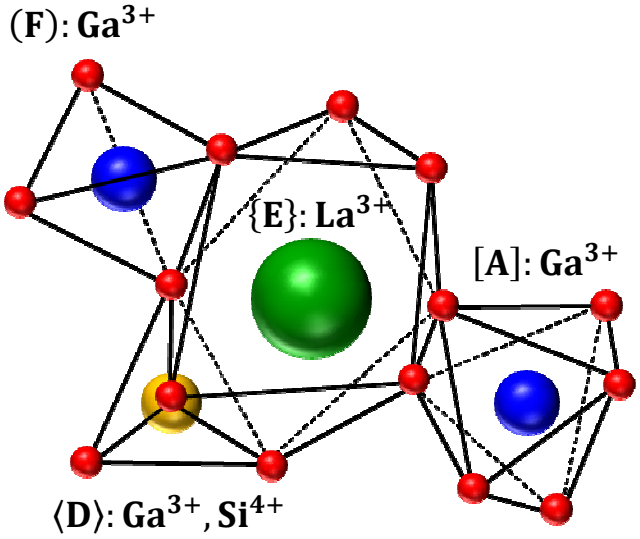

Fig. 2.2 Schematic coordination polyhedra of O atoms around the cationic atoms of the $\{E\}_3[A](F)_3\langle D\rangle_2O_{14}$-type structure.

Table 2.1 Physical properties of $La_3Ga_5SiO_{14}$

	$La_3Ga_5SiO_{14}$
crystal system	Trigonal
point group	32
lattice constant (nm) [7]	a = 0.8162 c = 0.5087
density ($kg \cdot m^{-3}$)	5754
melting point (ºC)	~1500
Curie temperature (ºC)	—
Mohs hardness [8]	6.6
thermal expansion coefficient ($\times 10^{-6}$ ºC^{-1})	α_{11} = 6.09 α_{33} = 4.43
piezoelectric constant at 25 ºC ($\times 10^{-12}$ C·N^{-1})	d_{11} = – 6.06 d_{14} = 5.65
dielectric constant at 25 ºC	$\varepsilon_{11}^{T}/\varepsilon_0$ = 19.0 $\varepsilon_{33}^{T}/\varepsilon_0$ = 50.3

2.3. Experimental procedure

2.3.1. Solid-state reaction

The target phase formation in oxide mixtures of various compositions was studied using a solid-state reaction technique. Highly pure La_2O_3 (99.99% grade), Ga_2O_3 (99.99% grade), Al_2O_3 (99.99% grade), and SiO_2 (99.995% grade) were used for the starting materials, which were prepared by mixing the respective 99.99% pure oxide powders at stoichiometric composition and pressing them into pellets. Polycrystals with $\{E\}_3[A](F)_3\langle D\rangle_2O_{14}$-type structures were synthesized using a resistance furnace with SiC heating elements. The temperature used for the syntheses ranged from 1400–1520 °C depending on the starting material. The holding times for the reactions were 2 h. The phases of the resultant crystals were identified via powder X-ray diffraction.

The determination of the solid solubility of Al in LGS was done using the solid-state reaction. First, the appropriate amounts of each powder required to correspond to the chemical formula of $La_3Ga_{5-x}Al_xSiO_{14}$ (with x = 0.0 - 5.0) were weighed. Each mixed powder sample was then fired for 6 h at temperatures between 1400 and 1520 °C. The phase identification and lattice constants measurements for each sample were done by the x-ray powder diffraction method. Lattice constants were calculated by Cohen's method.

2.3.2. Crystal growth

The LGAS crystals (25 mm diameter) with various contents of Al were grown

via the conventional Czochralski method using an Ir or a Pt–Rh (10%) crucible (50 mm in diameter and height). The pulling direction was <001>, the pulling rate was 1–5 mm h^{-1}, and the rotation rate was 10–40 rpm. About 80 wt% of the melt was crystallized in each growth.

2.4. Characterization

2.4.1. Solid-phase reaction

The solid solubility of Al in LGS was determined via a solid-state reaction. Highly pure La_2O_3 (99.99% grade), Ga_2O_3 (99.99% grade), Al_2O_3 (99.99% grade), and SiO_2 (99.995% grade) were used as starting materials. Appropriate amounts of these powders were weighed out to correspond to the chemical formula of $La_3Ga_{5-x}Al_xSiO_{14}$ (x = 0.0–5.0). Each mixed powder sample was fired for 6 h at temperatures between 1400 and 1520 °C. The phase identification and lattice constant measurements for each sample were done via X-ray powder diffraction. The lattice constants were calculated using Cohen's method.

The Al content in each grown crystal was determined via the fundamental parameter–group method using an X-ray fluorescence analyzer (Rigaku SYS3270). Five 1 mm thick sample wafers were cut at intervals of around 20 mm between the top and bottom of the constant diameter part of the crystal. The accuracy of the measured quantitative values for Al was less than 0.4%.

2.4.2. Crystal structure analysis

The structures of the grown crystals were examined via single-crystal X-ray diffraction using a four-circle diffractometer (Rigaku AFC6) with Mo K_α radiation (λ = 0.071069 nm). Single crystals cut from the grown boule were ground into spheres with 0.11–0.14 mm diameters and used for structural analysis. The integrated intensity data was collected up to $2\theta = 90°$ at a scan speed of 4° min^{-1}. The data were corrected for Lorentz and polarization effects. Crystal refinements were carried out using the full matrix least-squares program SHELXL93 [9]. The unit cell parameters were determined by the least-squares calculation of twenty 2θ values in the range of $20° \leq 2\theta \leq 30°$. The final residual factor, R, and weighted factor, R_w (F^2), values for the refinement with anisotropic temperature factors ranged from 0.034–0.038 and 0.074–0.089, respectively.

2.4.3. Dielectric, piezoelectric and elastic properties

The fundamental piezoelectric and elastic equations are expressed as follows:

$$S_\mathrm{i} = s_\mathrm{ij}^\mathrm{E} T_\mathrm{j} + d_\mathrm{ki} E_\mathrm{k} \tag{2-1}$$

$$D_\mathrm{m} = d_\mathrm{mj} T_\mathrm{j} + \varepsilon_\mathrm{mk}^\mathrm{T} E_\mathrm{k} \tag{2-2}$$

where the notations represent: S, strain; T, stress; E, electric field; D, electric displacement; s_ij^E, elastic compliance (constant field); d_mj, piezoelectric constant (strain constant); and $\varepsilon_\mathrm{mk}^\mathrm{T}$, dielectric constant (stress free).

Langasite belongs to the crystal class 32; the material constants for this crystal class consist of two independent dielectric constants ε_{11} and ε_{33}, two independent

piezoelectric constants d_{11} and d_{14} and seven independent elastic compliance constants s_{11}, s_{12}, s_{13}, s_{14}, s_{33}, s_{44}, and s_{66} as shown Table 2.2.

Table 2.2 Elast-piezo-dielectric matrix for crystal class 32 [10]

$$\left|\begin{array}{cccccc|ccc} s_{11} & s_{12} & s_{13} & s_{14} & 0 & 0 & d_{11} & 0 & 0 \\ s_{12} & s_{11} & s_{13} & -s_{14} & 0 & 0 & -d_{11} & 0 & 0 \\ s_{13} & s_{13} & s_{33} & 0 & 0 & 0 & 0 & 0 & 0 \\ s_{14} & -s_{14} & 0 & s_{44} & 0 & 0 & d_{14} & 0 & 0 \\ 0 & 0 & 0 & 0 & s_{44} & 2s_{14} & 0 & -d_{14} & 0 \\ 0 & 0 & 0 & 0 & 2s_{14} & s_{66} & 0 & -2d_{11} & 0 \\ \hline d_{11} & -d_{11} & 0 & d_{14} & 0 & 0 & \varepsilon_{11} & 0 & 0 \\ 0 & 0 & 0 & 0 & -d_{14} & -2d_{11} & 0 & \varepsilon_{11} & 0 \\ 0 & 0 & 0 & 0 & 0 & 0 & 0 & 0 & \varepsilon_{33} \end{array}\right|$$

These materials constants were determined based on the impedance and phase characteristics (shown in Fig. 2.3) of certain vibrating elements cut from a crystal [11]. In the case of the langasite crystal, these material constants are determined with this method by using four oriented elements with their thickness direction along the X-axis, and with their lengths at orientations ranging from –30° to +60° around the X-axis of the crystal as shown in Fig. 2.4. In addition to these X-axis measurements, a Y-cut crystal is also used to measure the resonance and anti-resonance frequencies in the face-shear and thickness shear modes.

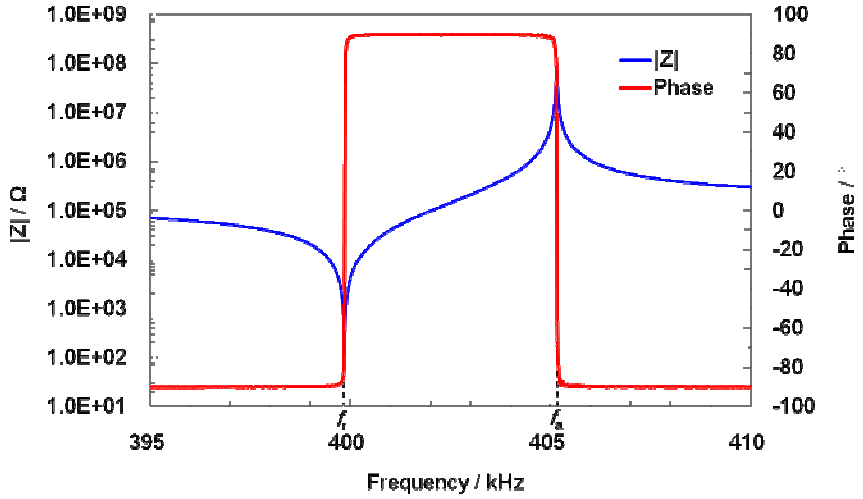

Fig. 2.3 Impedance and phase characteristics of a piezoelectric crystal around the resonance and anti-resonance frequencies.

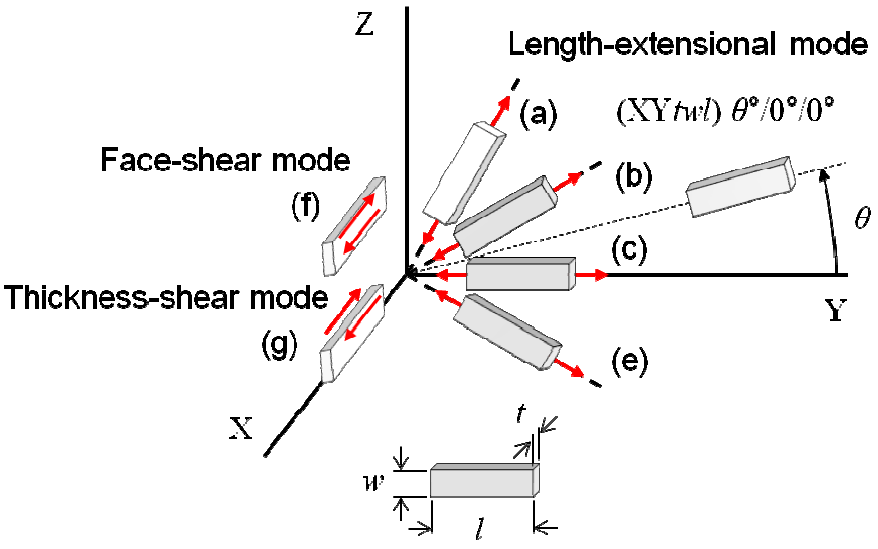

Fig. 2.4 Shapes and orientations of crystals for the investigation of material constants. Notation of (XY*twl*) θ°/0°/0° follows the definition in Ref. [12].

The vibration modes excited using each element and the constants obtained are listed in Table 2.3.

Table 2.3 Effective elastic and piezoelectric constants

Specimen	Vibration mode	Constants
(XY*tw*l) 0°/0°/0° bar	Length-extensional	k_{12}, d_{11}, s_{11} (= s_{22})
(XY*tw*l) θ°/0°/0° bar θ = –30°, 0°, +30°, +60°	Length-extensional	d_{14}, s_{33}, $2s_{13} + s_{44}$, s_{14}
Y-cut bar	Face-share	k_{25}, s_{44} (= s_{55})
	Thickness-share	k_{26}
X-cut square plate	—	ε_{11}
Z-cut square plate	—	ε_{33}

The elastic constants and piezoelectric constants were obtained by measuring the resonance and anti-resonance frequencies of the vibrating elements by applying the formulas (2-3) to (2-5) [11].

$$f_s = \frac{1}{2l\sqrt{\rho s_{11}^E}} \tag{2-3}$$

$$s_{22}^{E'} = s_{22}^E \cos^4\theta + s_{33}^E \cos^4\theta - s_{14}^E \cos^4\theta \sin\theta + (2s_{13}^E + s_{44}^E)\sin\theta \tag{2-4}$$

$$d_{12}' = \frac{1}{2}[-d_{11}(1 + \cos 2\theta) + d_{14}\sin 2\theta] \tag{2-5}$$

Vibrating elements were cut out of the crystal oriented within ± 0.1° using an X-ray technique and were carefully polished. The dimensions of the elements were: w = 1–2.5 mm, l = 10–30 mm, and t = 0.5–2.0 mm. Aluminum electrodes were fabricated by applying a vacuum deposition technique on both sides of the cut crystal perpendicular to the X-axis for the elements (a), (b), (c), and (d), and perpendicular to the Y-axis for elements (e) and (f) shown in Fig. 2.4. Resonance and anti-resonance frequencies of the vibrating elements were measured with an impedance gain phase analyzer (Agilent 4294A). Coaxial probes shown in Fig. 2.5 were also applied to reduce stray capacitance. The dielectric constants ε_{11} and ε_{33} were measured at 1 kHz.

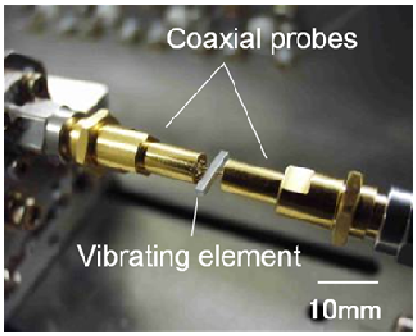

Fig. 2.5 Coaxial probes for measuring impedance characteristics.

Examples of measured data for $La_3Ga_5SiO_{14}$ are listed in Table 2.4 and Table 2.5.

Table 2.4 Measured resonance and anti-resonance frequencies for length-extensional mode of vibrating elements cut from $La_3Ga_5SiO_{14}$ as shown in Fig. 2.4

Cut	Dimension (mm)			f_r (Hz)	f_a (Hz)	Q_m	k_{12}'	$s_{22}^{E}{}'$	d_{11}'
	l	*w*	*t*						
(XY*twl*)–30°/0°/0°	20.010	2.507	0.523	132019	132240	32297	0.064	6.241	2.135
(XY*twl*)0°/0°/0°	20.010	2.501	0.523	111179	112333	13671	0.159	8.800	6.058
(XY*twl*)30°/0°/0°	20.010	2.503	0.523	100710	101852	27435	0.166	10.72	6.980
(XY*twl*)60°/0°/0°	20.012	2.510	0.523	121645	122293	31622	0.114	7.350	4.013

Table 2.5 Measured resonance and anti-resonance frequencies for face-shear and thickness-shear modes of vibrating elements cut from $La_3Ga_5SiO_{14}$ as shown in Fig. 2.4

Cut	Mode	Dimension (mm)			f_r (Hz)	f_a (Hz)	Q_m
		l	*w*	*t*			
Y-cut	thickness-shear	20.038	2.525	1.030	579110	580732	13434
	face-shear	19.969	2.520	1.037	1315364	1327087	14584

2.5. Results and discussion

2.5.1. Solubility limit of Al in Langasite

The LGAS phases produced by solid-state reactions at various temperatures are shown in Fig. 2.6. No secondary phase was observed at mole fractions of Al (x values) up to 1.5; however, when x > 1.5, an aluminum-gallate, $La(GaAl)O_3$, phase appeared.

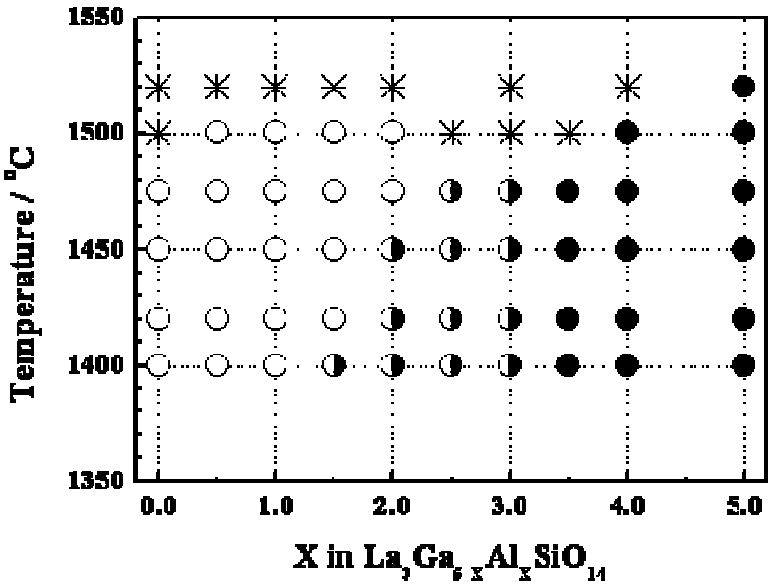

Fig. 2.6 Results of the solid-state reactions of $La_3Ga_{5-x}Al_xSiO_{14}$ where ○ : LGS, ● : $La(GaAl)O_3$, ◑ : mixed phase of LGS and $La(GaAl)O_3$, ✳: molten.

The dependence of the lattice constants on the Al content is shown in Fig. 2.7. Powder samples synthesized at 1475 °C were used for the measurements. Both lattice constants, i.e., the a and c axes, decreased linearly with increasing x in the range of $0 \leq x \leq 1.5$. Both a and c have an inflection point at around x = 1.5. The variation of the lattice constants when x > 1.5 agree with the formation of a $La(GaAl)O_3$ phase, as shown in Fig. 2.6. Based on these results, the solid-solubility limit of Al in LGS was determined to be 1.5. Therefore, crystal growth was performed under x < 1.5 conditions.

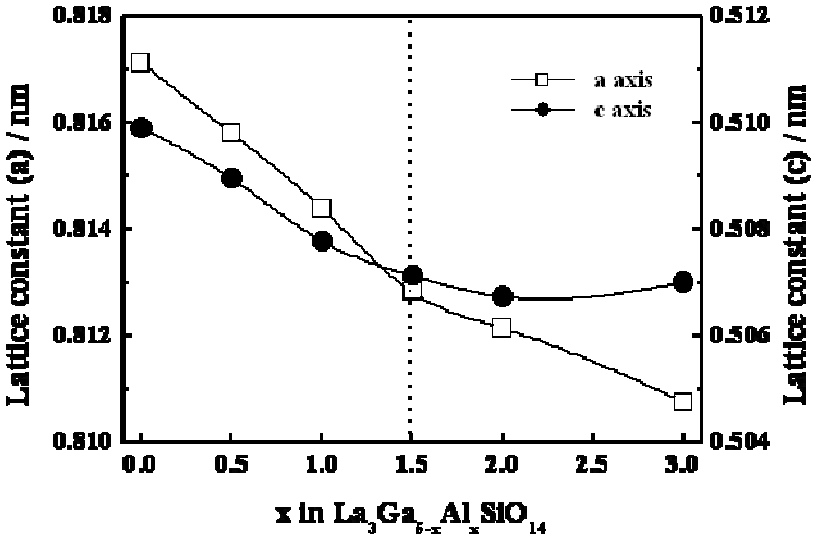

Fig. 2.7 Dependence of lattice constants on Al content in $La_3Ga_{5-x}Al_xSiO_{14}$.

The photograph of an LGAS (x = 1.0) crystal grown at a pulling rate of 1 mm h^{-1} shown in Fig. 2.8 (a) shows many cracks and inclusions during the initial growth stage. However, LGAS with a smaller content of Al (x = 0.9) produced a good quality crystal under the same growth conditions, as shown in Fig. 2.8 (b). The growth of

Al-substituted LGS at x values ranging from 0–0.9 occurred as easily as that of LGS regardless of the Al content. The discrepancy in the results between the solid-solubility limit of Al in the solid-state reaction and the Al content of the good quality grown crystal is likely because the LGS phase was metastable in the range of $1.0 \leq x \leq 2.0$ and easily decomposed the $La(GaAl)O_3$ and other phases above the melting point.

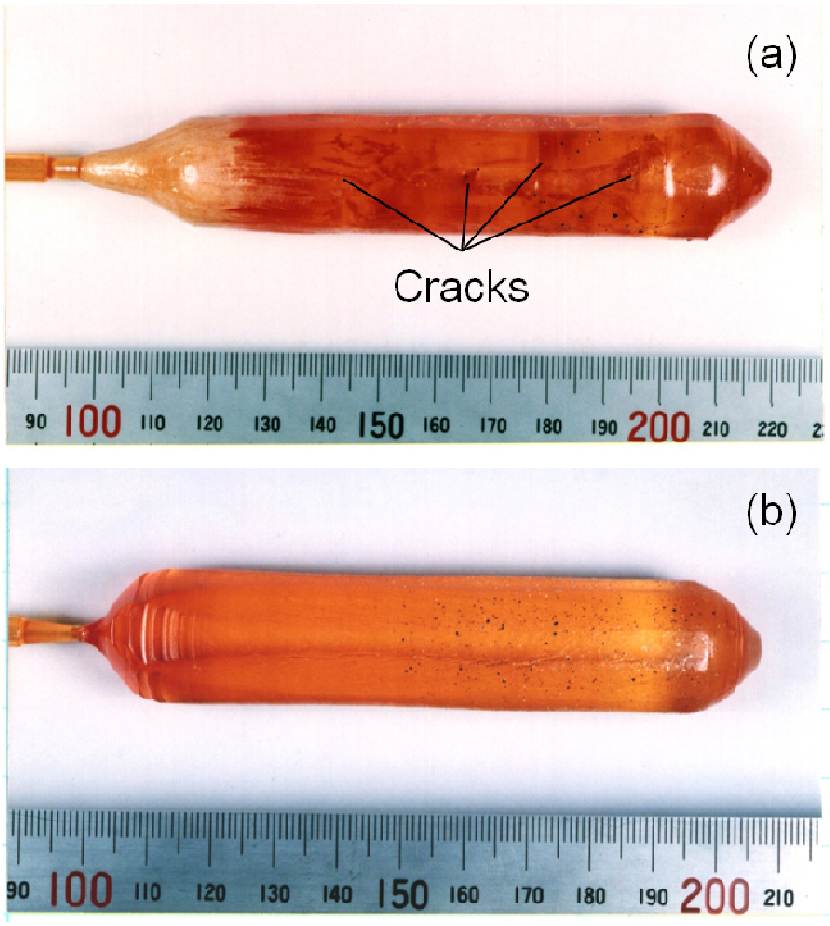

Fig. 2.8 Photographs of as-grown crystals: (a) $La_3Ga_{4.0}Al_{1.0}SiO_{14}$, (b) $La_3Ga_{4.1}Al_{0.9}SiO_{14}$. The left side is the initial stage of crystal growth. The scale of the ruler is mm.

It is important to evaluate the homogeneity along the pulling direction of Al in a single crystal because the homogeneity of the SAW velocity and the electromechanical coupling factor of the substrate are dependent on it. Therefore, we estimated the effective-segregation coefficient, k_{eff}, using the following equation:

$$C_s = k_{eff} C_0 (1 - g)^{k_{eff}-1} \quad (2\text{-}6)$$

where C_s, C_0, and g represent the concentration in the solid phase, the initial concentration, and the solidification factor, respectively [13]. Fig. 2.9 shows the relationship between k_{eff} and the growth rate with various Al contents. The k_{eff} decreases slightly with increased growth rate and Al content. From these results, k_{eff} was determined to be between 1.03 and 1.07.

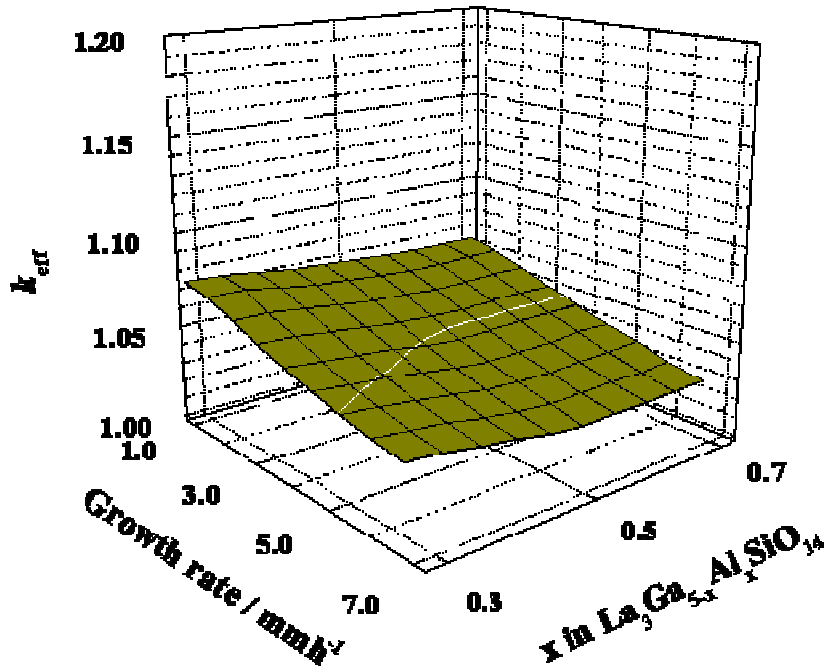

Fig. 2.9 Dependence of the effective segregation coefficient, k_{eff}, on Al content and growth rate.

2.5.2. Structural analysis of Al-substituted Langasite

Table 2.6 Lattice constants, site occupancy, mean oxo-bond distances, and structural distortion of $La_3Ga_{5-x}Al_xSiO_{14}$ crystals gives the structural refinement results for $La_3Ga_{5-x}Al_xSiO_{14}$ crystals, which include the lattice constants and site occupancies along with other relevant structural information. Both lattice constants, i.e., a and c, decrease with increasing Al content in the crystals. This result is likely caused by the difference in the cation size ($r_{Al} < r_{Ga}$) [14]. The distributions of Al and Ga in the LGAS crystals were analyzed via common site–multiplicity refinement. Although the distribution of Al into either octahedral (Ga1) or tetrahedral (Ga2 and Ga3) sites was examined first, the structural parameters obtained suggest that Al atoms occupy all cation sites except for the La sites. Finally, for LGAS crystals with x = 0.6 and 1.0, the distribution model in which the Al atom partially occupies the Ga sites produced the smaller R values, as mentioned in the third paragraph. Moreover, the chemical compositions, which were determined using the site occupancy data in this model (see Table 2.6), of $La_3Ga_{4.41}Al_{0.59}SiO_{14}$ for LGAS (x = 0.6) and $La_3Ga_{4.03}Al_{0.97}SiO_{14}$ for LGAS (x = 1.0) agreed well with those determined using chemical analysis. Therefore, the Al and Ga atoms coexist in one octahedral and two tetrahedral sites, as shown in Fig. 2.10. The Al occupancy ratio, Al/(Ga + Al), was highest in the Ga3 site (i.e., 0.18 and 0.28 for LGAS (x = 0.6) and (x = 1.0), respectively) (see Table 2.6). Furthermore, there is a significant preference for the Ga1 site over the Ga2 site. Al also favors the octahedral site in $Y_3Ga_{5-x}Al_xO_{12}$ [15], and $Gd_3Ga_{5-x}Al_xO_{12}$ [16], which have similar coordination polyhedrons. The mean cation–oxygen distances, D_i (i = 4, 4', 6, and 8), are summarized in Table 2.6. The D_8 value remains constant at about 0.2592 nm while

the D_4, $D_{4'}$, and D_6 values clearly decrease with increasing Al content. The magnitude of the distance changes [$(\Delta D_6/\Delta x):(\Delta D_4/\Delta x):(\Delta D_{4'}/\Delta x) \approx 1.7:1:2.7$] is consistent with that of the Al occupancy ratio (1.6:1:1.9) in the corresponding sites, as derived from the site-multiplicity refinement results. This variation in the cation–oxygen distances results from the displacement of the oxygen anions caused by the preference of the smaller cation (Al^{3+}) for the tetrahedral Ga3 site. Table 2.6 also shows the structural distortion, Δ, [3] of each coordination polyhedron unit, which is defined by $\Delta = (1/\mathrm{N})\sum(R_i - \bar{R}/\bar{R})^2$, where N is the coordination number (i.e., 8 for the La decahedron, 6 for the Ga1 octahedron, and 4 for the Ga2 and Ga3 tetrahedrons), R_i is the individual bond length, and $\bar{R}$ is the average bond length. The La decahedron maintains a constant Δ; therefore, its distortion is independent of the Al substitution. However, the distortion of the Ga3 tetrahedron is dependent on the Al content. Because the structural distortion of the La site and mean La^{3+}–O distances did not change, the Al substitution was determined to only affect the occupied sites (i.e., Ga1, Ga2, and Ga3 sites).

Table 2.6 Lattice constants, site occupancy, mean oxo-bond distances, and structural distortion of $La_3Ga_{5-x}Al_xSiO_{14}$ crystals

Al content (x)		0.0	0.6	1.0
Unit cell (±0.0001 nm)				
a		0.8161	0.8154	0.8146
c		0.5094	0.5083	0.5071
V [nm^3]		0.2938	0.2927	0.2914
Site occupancies (±0.01)				
Ga1 site	Al:Ga	—	0.14:0.86	0.24:0.76
Ga1 site	Al:Ga	—	0.09:0.91	0.15:0.85
Ga1 site[a]	Al:Ga	—	0.09:0.41	0.14:0.36
Mean oxo-bond distances, Di [nm]				
$(La-O)_{ave}$	D_8	0.2590	0.2592	0.2592
$(La-O)_{ave}$	D_6	0.1994	0.1989	0.1980
$(Ga2-O)_{ave}$	D_4	0.1854	0.1848	0.1844
$(Ga3-O)_{ave}$	$D_{4'}$	0.1741	0.1729	0.1719
Distortion, Δ (magnified by 10^4)				
La site		54	54	54
Ga1 site[b]		0	0	0
Ga2 site		7.1	8.4	7.5
Ga3 site		0.2	0.3	0.6

[a] On the basis of the results of the LGS samples, the occupancy of the Si atom in the Ga3 site was fixed at 0.5 during the refinement process.

[b] The structural distortion around the Ga1 site was not determined because all the cation – oxygen interatomic distances were the same. The coordinating oxygens are placed at an equivalent position (6 g).

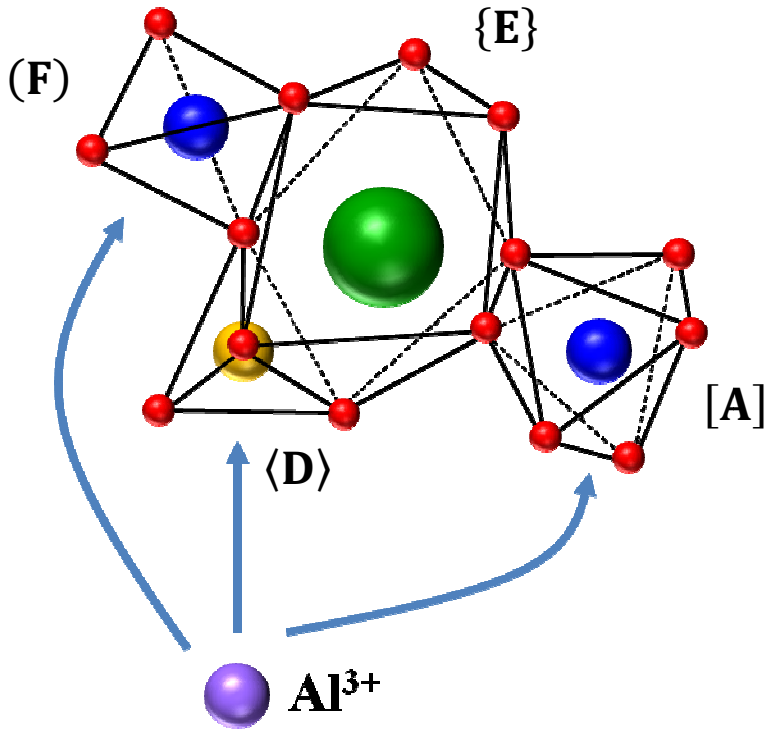

Fig. 2.10 Schematic of a portion of the langasite crystal lattice.

2.5.3. Effects of Al-substitution on piezoelectric properties of Langasite

Fig. 2.10 shows the changes in the piezoelectric constants as a function of the mole fraction of Al (x) in LGAS. With increasing Al content, the absolute piezoelectric strain modulus, $|d_{11}|$, increases by about 1.3% while d_{14} decreases by 7.7%. The piezoelectric modulus, $|d_{11}|$, of LGS decreased with the increasing atomic number of the rare-earth element occupying the decahedral site, e.g., when La is replaced by Pr and Nd [17]. In these crystals, the D_8 value decreased with decreasing ionic radii of the rare earth element ($r_{La} > r_{Pr} > r_{Nd}$) [3] while the other distances did not change. Similar observations were made for $AE_3Ga_2Ge_4O_{14}$ (AE = Ca and Sr) crystals [4]. In the LGAS crystals, the D_8 value appears to extend relative to the reduction of the D_4, $D_{4'}$, and D_6 value (Table 2.6). Based on these results, it is probable that the piezoelectric modulus, $|d_{11}|$, of the $Ca_3Ga_2Ge_4O_{14}$-type crystals would increase with the extension of D_8. Because there are few reports about the d_{14} of these compounds, this tendency was not realized until now.

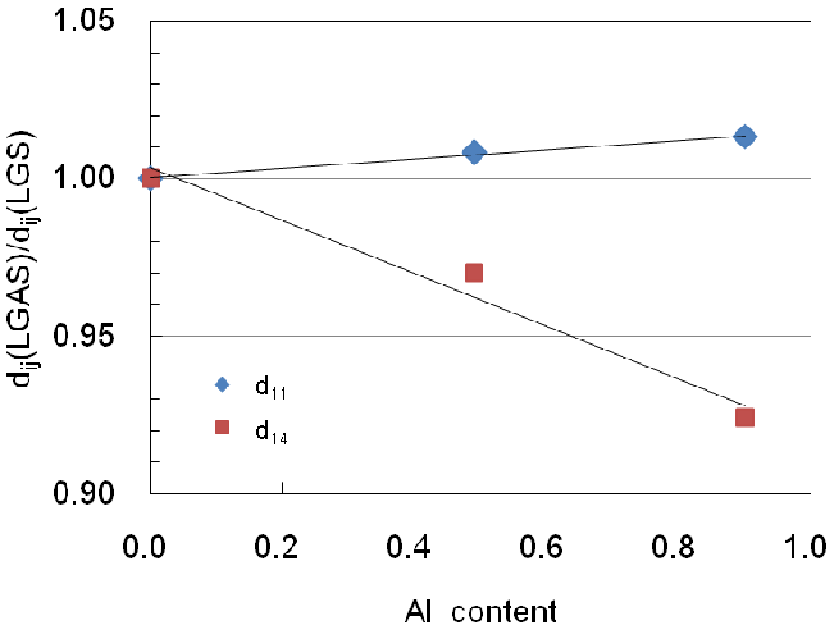

Fig. 2.11 Dependence of the piezoelectric constants, $|d_{11}|$, and d_{14} of $La_3Ga_{5-X}Al_XO_{14}$ on Al substitution. The solid lines are included as visual guides.

Table 2.7 shows the material constants of the LGAS single crystals compared with those of LGS, $La_3Nb_{5.5}Ga_{0.5}O_{14}$ (LNG), and $La_3Ta_{5.5}Ga_{0.5}O_{14}$ (LTG). LNG and LTG crystals are included because they are superior piezoelectric materials that have advantages such as ease of growth to a large size and larger k_{ij} [3]. All the factors of the LGAS with x = 0.6 are greater than those of LGS while excess Al substitution (x = 1.0) decreased the factors. In addition, the LGAS crystal with x = 0.6 has piezoelectric properties comparable to those of LNG and LTG crystals. Al substitution enables the use of a lower amount of expensive gallium oxide as a raw material. For the LGAS crystal with x = 0.6, a large reduction (~20%) of the requisite amount of Ga_2O_3 as compared to that for LTG is expected. Therefore, Al substitution of LGS is useful for obtaining preferable piezoelectric materials with $Ca_3Ga_2Ge_4O_{14}$-type structures for both bulk and surface acoustic wave applications.

Table 2.7 Material constants of $La_3Ga_{5-x}Al_xSiO_{14}$ compared with those of other $Ca_3Ga_2Ge_4O_{14}$-type crystals

	LGS	LGAS (x = 0.6)	LGAS (x = 0.9)	LNG[a]	LTG[a]
ρ	5740	5672	5553	5905	6145
d_{11}	–6.06	–6.11	–6.14	–7.41	–7.06
d_{14}	5.65	5.48	5.22	6.16	4.32
s_{11}^{E}	8.80	8.73	8.68	9.08	9.18
s_{12}^{E}	–3.86	–4.41	–3.95	–4.58	–4.53
s_{13}^{E}	–1.60	–1.48	–1.69	–1.72	–1.84
s_{14}^{E}	–3.45	–3.44	–3.39	–3.68	–3.66
s_{33}^{E}	5.04	5.00	5.21	5.17	5.23
s_{44}^{E}	20.36	19.77	19.53	22.08	21.45
s_{66}^{E}	25.33	26.11	25.25	27.35	27.37
$\varepsilon_{11}^{T}/\varepsilon_0$	19.0	18.5	18.1	20.7	19.6
$\varepsilon_{33}^{T}/\varepsilon_0$	50.3	48.0	46.7	79.0	76.5
k_{12}	0.159	0.162	0.162	0.160[b]	0.187[c]
k_{25}	0.083	0.088	—	0.080[b]	0.072[c]
k_{26}	0.147	0.152	—	0.140[b]	—

ρ, density ($kg \cdot m^{-3}$); d_{ij}, piezoelectric moduli ($pC \cdot N^{-1}$); s_{ij}^{E}, elastic compliances ($pm^2 \cdot N^{-1}$); $\varepsilon_{ij}^{T}/\varepsilon_0$, relative dielectric coefficients; k_{ij}, electromechanical coupling factors.

[a] [18]; [b] [19], [c] [3].

2.6. Conclusion

We have grown $La_3Ga_{5-x}Al_xSiO_{14}$ single crystals without any inclusions and cracks up to x = 0.9 using a Czochralski method. The effective segregation coefficient (k_{eff}) of Al fell between 1.03 and 1.07. The results of the single-crystal x-ray structure analysis indicated that Al atoms occupy both octahedral and two tetrahedral sites, keeping the magnitude of the site preference. The piezoelectric constant $|d_{11}|$ was slightly larger, but d_{14} was smaller than those of LGS. The electromechanical coupling factors (k_{12}, k_{25}, and k_{26}) of LGAS (x = 0.6) were larger than those of LGS. The LGAS (x = 0.6) crystal is currently the most promising material with respect to piezoelectric properties. On the basis of this research, investigations of LGAS for certain applications are still ongoing [20,21].

References

[1] M. Kadota, J. Nakanishi, T. Kitamura, and M. Kumatoriya, Jpn. J. Appl. Phys., **38**, 5 (1999).

[2] S. Uda, A. Bungo, and C. Jian, Jpn. J. Appl. Phys., **38**, 5516 (1999).

[3] Y. V. Pisarevsky, P. A. Senyushenkov, B. V. Mill, and N. A. Moiseeva, Proc. IEEE Int. Freq. Cont. Symp., 742 (1998).

[4] A. A. Kaminskii, E. L. Belokoneva, B. V. Mill, Y. V. Pisarevskii, S. E. Sarkisov, I. M. Silvestrova, A. V. Butashin, and G. G. Khodzhabagyan, Phys. Stat. Sol. (a), **86**, 345 (1984).

[5] K. Shimamura, H. Takeda, T. Kohno, and T. Fukuda, J. Cryst. Growth, **163**, 388 (1996).

[6] K. Momma and F. Izumi, J. Appl. Crystallogr., **44**, 1272 (2011).

[7] A. A. Kaminskii, B. V. Mill, G. G. Khodzhabagyan, A. F. Konstantinova, A. I. Okorochkov, and I. M. Silvestrova, Phys. Stat. Sol. (a), **80**, 387 (1983).

[8] E. Ansorgea, S. Schimpfa, S. Hirscha, J. Sauerwaldb, H. Fritzeb, and B. Schmidta, Sensors and Actuators A, **132**, 271 (2006).

[9] G. M. Scheldrick, Computer code SHELXL93, Georg-August- University Gottingen, Germany (1993).

[10] J. F. Nye, *Physical Properties of Crystals* (Oxford University Press, Oxford, 1957), p. 299.

[11] W. P. Mason, *Piezoelectric Crystals and Their Application to Ultrasonics* (D. Van Nostrand, New York, 1950), p. 204.

[12] IEEE Standard on Piezoelectricity, ANSI/IEEE Std, 176-1987 (1988).

[13] B. Chalmers, *Principles of Solidification* (Wiley, New York, 1964), p. 131.

[14] R. D. Shannon, Acta Crystallogr. A, **32**, 751 (1976).

[15] M. Marezio, J. P. Remeika, and P. D. Dernier, Acta Crystallogr. B, **24**, 1670 (1968).

[16] H. Kimura, T. Numazawa, M. Sato, and H. Maeda, Jpn. J. Appl. Phys., **28**, 1644 (1989).

[17] J. Sato, H. Takeda, H. Morikoshi, K. Shimamura, P. Rudolph, and T. Fukuda, J. Cryst. Growth, **191**, 746 (1998).

[18] J. Bohm, E. Chilla, C. Flannery, H.-J. Fröhlich, T. Hauke, R. B. Heimann, M. Hengst, and U. Straube, J. Cryst. Growth, **216**, 293 (2000).

[19] I. M. Sil'vestrova, Y. V. Pusarevsky, A. A. Kaminski, and B. V. Mill, Sov. Phys. Solid State, **29**, 870 (1987).

[20] H. Takeda, S. Tanaka, S. Izukawa, H. Shimizu, T. Nishida, and T. Shiosaki, Proc. IEEE Ultrason. Symp., **1**, 560 (2005).

[21] H. Takeda, T. Kuze, T. Nishida, K. Uchiyama, and T. Shiosaki, Mater. Res. Bull., **43**, 6 (2008).

Chapter 3.

Growth and Optical Characterization of Zero-Birefringence-Controlled $LiTaO_3$ Crystal

3.1. Introduction

Lithium tantalite (LT), $LiTaO_3$, is one of the best ferroelectric crystalline materials. It is widely used for piezoelectric, pyroelectric, electro-optical, and nonlinear optical applications. Although the $LiTaO_3$ phase has a wide solid-solution range, a high-quality crystal for commercial applications can be grown at the congruent melting composition (Li: 48.5 mol% and Ta: 51.5 mol%).

The wide range of the solid-solution phase enables the modification of the properties of lithium tantalate by changing the [Li]/[Ta] ratio in the crystal. Furukawa et al. reported the successful growth of an off-congruent crystal with a stoichiometric composition using the double-crucible Czochralski method, which is described in Chapter 1 [1]. Excess Li in the composition decreases the number of Ta anti-site defects and cation vacancies. Such control of the defects via the [Li]/[Ta] ratio in $LiTaO_3$ improves the performance of wavelength conversion and holographic data storage devices.

The composition ratio in $LiTaO_3$ can potentially affect other characteristics as well. $LiTaO_3$ has a higher refractive index and transmittance up to the near-ultraviolet region than optical glass materials. However, at the congruent melting composition, $LiTaO_3$ is a uniaxial crystal and has a small birefringence. This birefringence depends

on the [Li]/[Ta] ratio of the crystal composition and can be eliminated at an optimum [Li]/[Ta] ratio [2]. Until now, there have only been a few fundamental reports about the zero-birefringence properties of $LiTaO_3$.

In this chapter, the growth of large and homogeneous crystals and the optical properties of $LiTaO_3$ with zero birefringence are described with a focus on practical applications.

3.2. $LiTaO_3$ crystal structure

$LiTaO_3$, which is a ferroelectric crystalline material, belongs to the trigonal crystal system and has a space group of 3m. It has the pseudo-ilmenite structure shown in Fig. 3.1 [3]. The structure of $LiTaO_3$ comprises planar sheets of oxygen atoms in a distorted hexagonal close-packed configuration. One-third of the octahedral interstices formed in this structure are filled with lithium atoms, one-third are filled with niobium atoms, and one-third are vacant. The charge separation that results from the shift of the lithium and niobium ions relative to the oxygen octahedra causes $LiTaO_3$ to exhibit spontaneous polarization at the Curie temperature (~600–700 °C) [4].

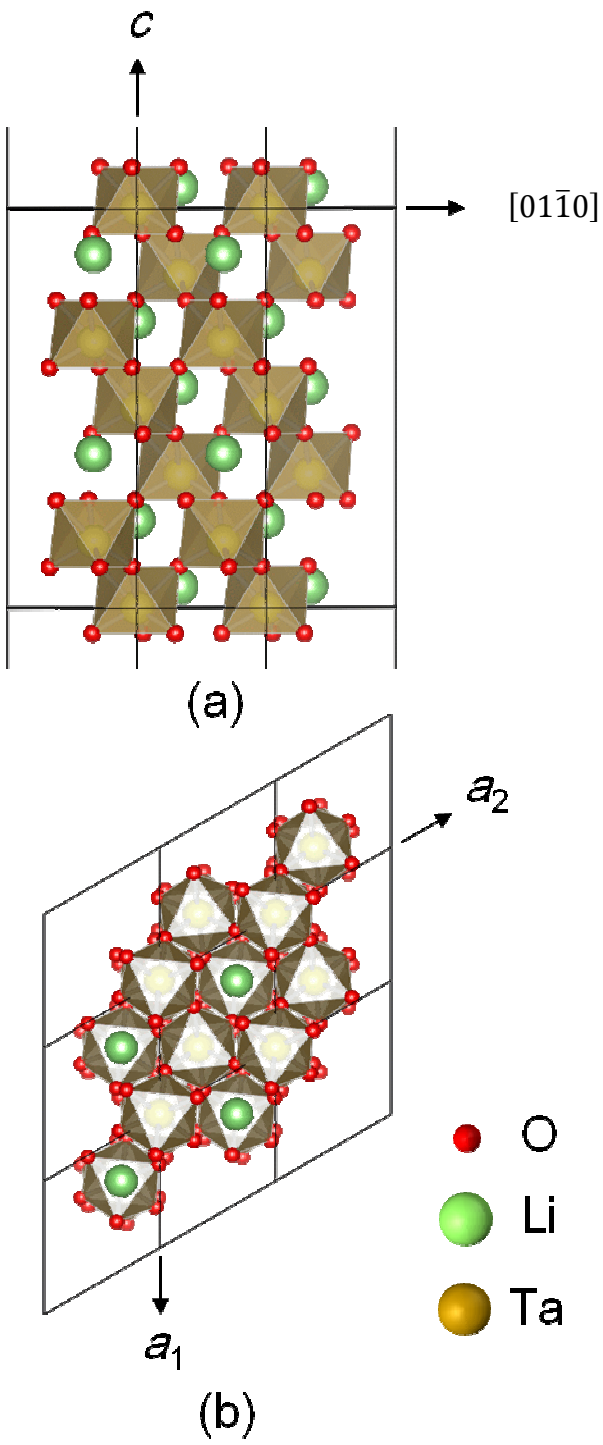

Fig. 3.1 Schematic illustration of the pseudo-ilmenite structure of $LiTaO_3$. The crystal structures were drawn with VESTA 3 [5].

Table 3.1 Physical properties of $LiTaO_3$

	$LiTaO_3$
crystal structure	Trigonal
point group	3m
lattice constant (nm) [6]	a = 0.51543 c = 1.37835
density ($kg \cdot m^{-3}$)	7454
melting point (ºC)	1650
Curie temperature (ºC)	605
Mohs hardness [7]	6 ~ 6.7
thermal expansion coefficient ($\times 10^{-6}$ ºC^{-1}) [6]	α_{11} = 16.1 α_{33} = 4.1
piezoelectric constant ($\times$pC·N^{-1}) [8]	d_{15} = 26 d_{22} = 7 d_{31} = – 2 d_{33} = 8
electrooptic coefficient at 632.8 nm (pm·V^{-1})	r_{13} = 7 r_{33} = 30.3
dielectric constant [9]	$\varepsilon_{11}^{T}/\varepsilon_0$ = 51 $\varepsilon_{33}^{T}/\varepsilon_0$ = 45
refractive index at λ = 600 nm [10]	n_o = 2.1834 n_e = 2.1878

3.3. Phase relation in Li_2O-Ta_2O_5 system

Phase relation in the vicinity of $LiTaO_3$ was first reported by Miyazawa et al. in 1971 [11]. A wide solid-solution range is present in this system, as shown in Fig. 3.2. The $LiTaO_3$ phase appears from 45.5 to 50.0% in the range of Li_2O [12]. The congruent melting composition was determined to be 49.75 mol% as per $Li_2O/(Ta_2O_5 + Li_2O)$.

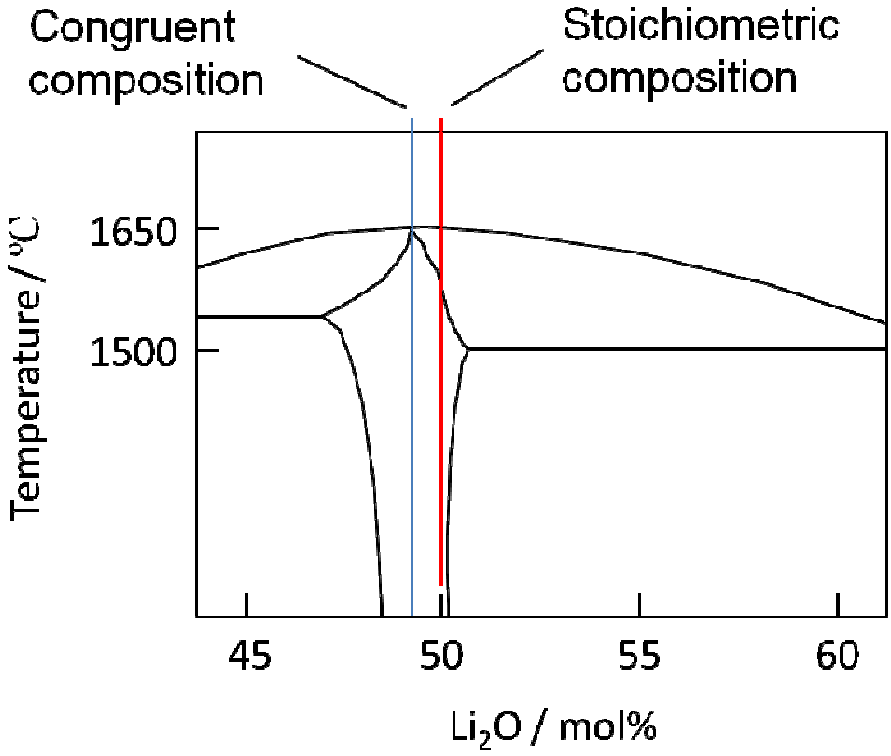

Fig. 3.2 Phase diagram of Li_2O-Ta_2O_5.

The variation of birefringence in $LiTaO_3$ was first investigated by Ballman et al. in 1967 [2] and was found to depend on the [Li]/[Ta] ratio. In fact, the birefringence becomes zero at a nearly stoichiometric [Li]/[Ta] ratio, as shown in Fig. 3.3. Because the composition of zero-birefringence $LiTaO_3$ is off-congruent, the general Czochralski technique could not be applied to the growth of its crystal, as mentioned in Chapter 1. Therefore, the DC-CZ technique was employed to grow this crystal.

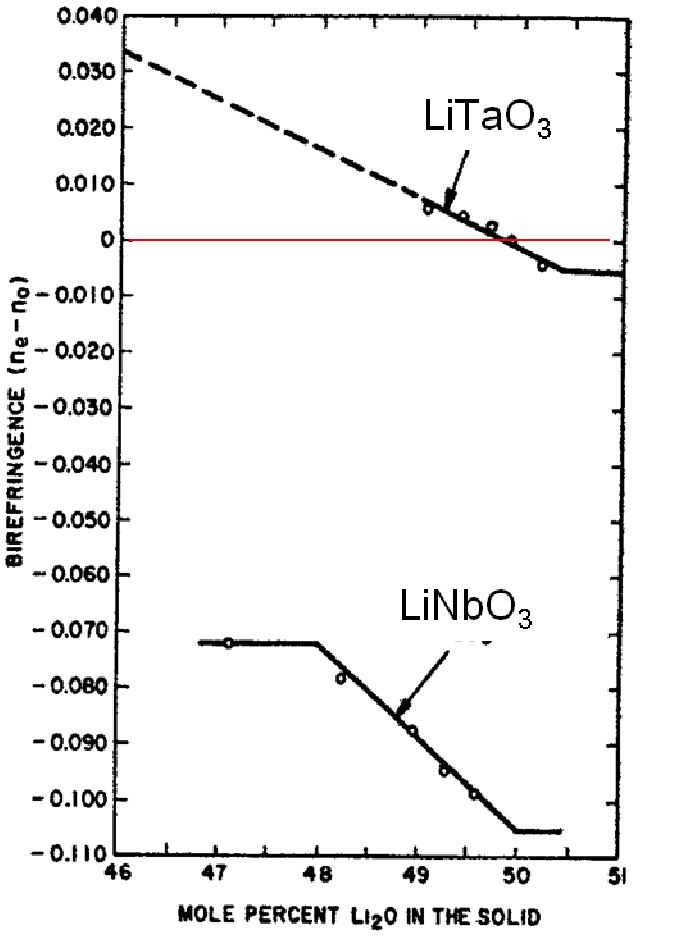

Fig. 3.3 Dependence of the birefringence on the solid composition of $LiNbO_3$ and $LiTaO_3$ [13].

3.4. Experimental procedure

3.4.1. Crystal growth

To determine the ideal solution composition for the growth of the zero birefringence crystal, the Czochralski method described in Chapter 1 was applied because this method enables faster determination of the crystal and solution composition. Accordingly, small crystals (diameters of 20 mm) were grown from various solution compositions (Li_2O ~ 53.0–57.0 mol%). The crystals were sufficient to measure their basic properties including composition, refractive indices, transmittance, and so on. The resultant crystals have a multi-domain structure of ferroelectric properties; therefore, a polling treatment was necessary. An as-grown crystal was placed in an alumina ceramic container and sandwiched by two platinum electrodes with the $LiTaO_3$ powder. After being heated at 700 °C for several hours with an electric current of ~0.1 mA cm^{-2}, the entire system were cooled at a rate of 20 °C h^{-1}. Samples that were sliced from the crystals were used to determine the [Li]/[Ta] ratio, measure the refractive indices, etc.

After determining the solution and crystal composition for a zero birefringence $LiTaO_3$ crystal using the small crystals, larger crystals were grown using the DC-CZ method with an auto supply system (shown in Fig. 3.4). To grow the crystals, the materials for the solution were prepared from Li_2O_3 (99.99%) and Ta_2O_3 (99.99%) powders by mixing these powders under a dry atmosphere and heating them for 8 h at 1300 °C in air. The synthesized material was pressed and loaded in the iridium double crucible described in Chapter 1. The material charged into the crucible was melted

under a nitrogen atmosphere using an RF induction heating system.

The material for the supply system was also prepared by weighing and mixing Li_2O_3 (99.99%) and Ta_2O_3 (99.99%) powders at the [Li]/[Ta] ratio of the zero-birefringence crystal. The mixture was placed in a rubber mold and pressed at a hydrostatic pressure of 1.0 ton·cm^{-2}. The pressed powder was then calcined at 1500 °C in air and the coarse grains were passed through a sieve (about 200 μm) to be used as the feed material.

After the materials were melted and homogenized for a sufficient period of time, a $< 01\bar{1}0 >$ seed made of congruent $LiTaO_3$ was placed on the surface of the melt and pulled up at a speed of 1 mm h^{-1}. The seed rotation rate was 5 rpm. The crucible was also rotated at 1 rpm during growth using the accelerated crucible rotation technique (ACRT) [14]. The feed material was continuously supplied to the solution at the same rate as the mass growth. An automatic diameter control system was used to define the shape of the crystal. Crystal growth was performed under the flow of 1 vol% of oxygen-mixed nitrogen gas. At the end of the process, the crystal was quickly removed from the melt and slowly cooled.

The polling treatment was carried out on the as-grown crystals using the same procedure as for the small crystals.

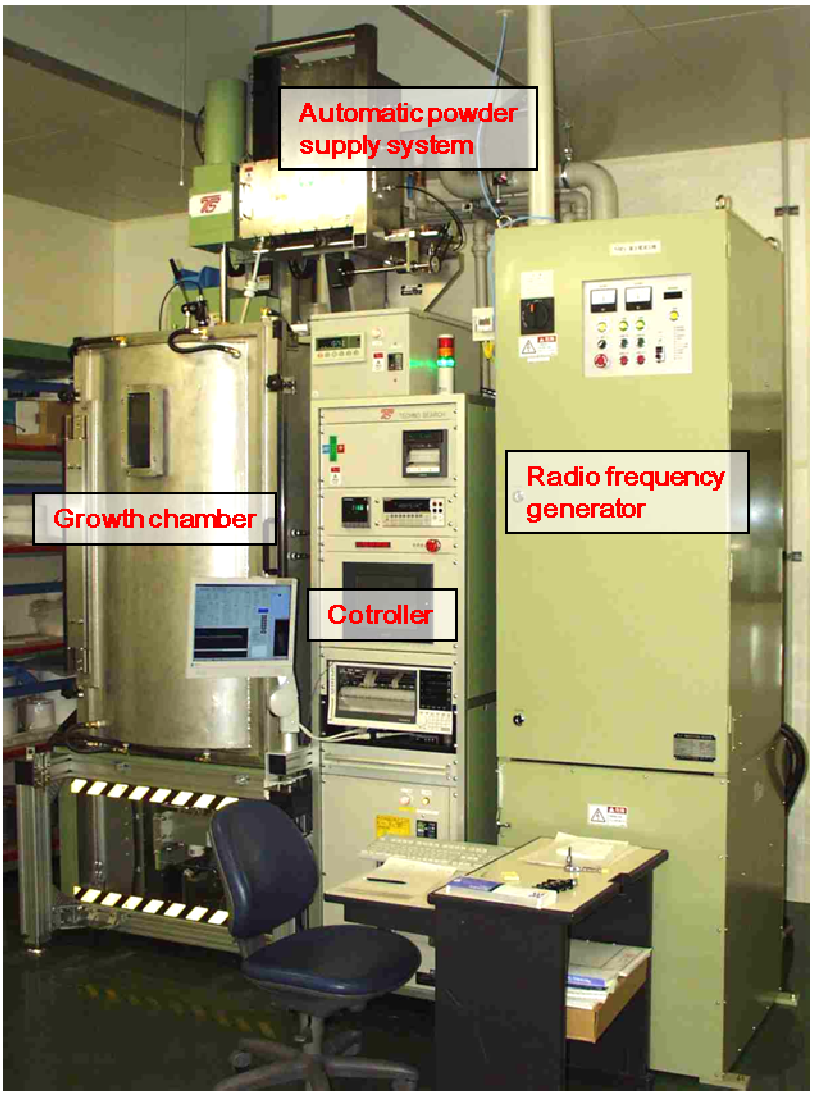

Fig. 3.4 DC-CZ crystal growth furnace.

3.4.2. Characterization

The [Li]/[Ta] ratios of the grown crystals were determined by measuring the Curie temperature [2]. Samples cut from the grown crystals were ground and put into a differential thermal analysis (DTA) furnace with a reference sample (i.e., α-alumina). The increasing and decreasing temperature rate for the scan was ±20 °C min^{-1}. The Li content of each sample was determined via the relationship between the [Li]/[Ta] ratio of the crystals and their Curie temperature.

The ordinary, n_o, and extraordinary, n_e, refractive indices of the crystals at room temperature were measured by the prism-coupling technique [15] at wavelengths of 450, 632.8, 1300, and 1550 nm. Y-cut wafers (0.5 mm thick), which were optically polished on both surfaces, were used for the measurement. The standard deviation of the refractive indices measured using this technique was ±0.0001. The obtained data were used to determine the [Li]/[Ta] ratio for zero birefringence.

To evaluate the homogeneity and birefringence of the crystals, precise measurement of the refractive indices was performed using the method of minimum deviation of the prism [10]. Prism samples with 40° vertical angles were cut from large crystals grown using the DC-CZ method. The accuracy of the refractive indices measured using this method is ±0.00001.

3.5. Results and discussion

Fig. 3.5 shows the relationship between the [Li]/[Ta] ratio and the refractive indices (ordinary, n_o, and extraordinary, n_e refractive indices) of the crystals measured at

a wavelength of 632.8 nm. n_e is more sensitive to variations in the [Li]/[Ta] ratio than n_o is. The point at which n_o and n_e lines intersect is the zero-birefringence point of the crystal. We determined that a [Li]/[Ta] ratio of 0.979 gives a crystal with zero birefringence. Fig. 3.6 shows the relationship between the crystal composition in Fig. 3.5 and the corresponding solution composition. From this data, we determined that the required composition of the solution to grow a zero-birefringence crystal is 55.0 mol% Li_2O.

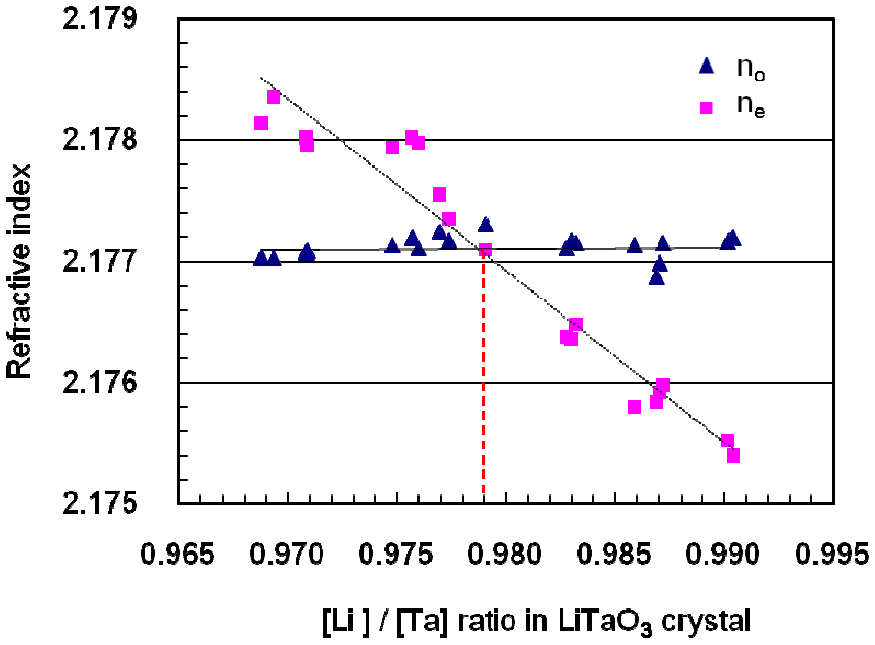

Fig. 3.5 Dependence of refractive indices on [Li]/[Ta] ratio.

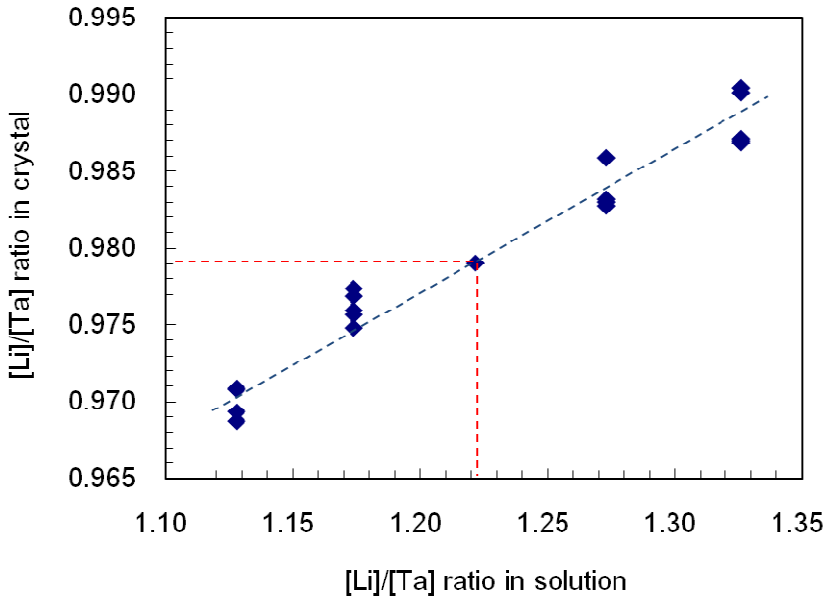

Fig. 3.6 Relationship between the [Li]/[Ta] ratios of the solution and the resultant crystals.

Fig. 3.7 shows zero birefringence $LiTaO_3$ boules grown using the DC-CZ method. The boules were slightly yellow but transparent and crack-free with a size of 80 mm in diameter and 80 mm in length.

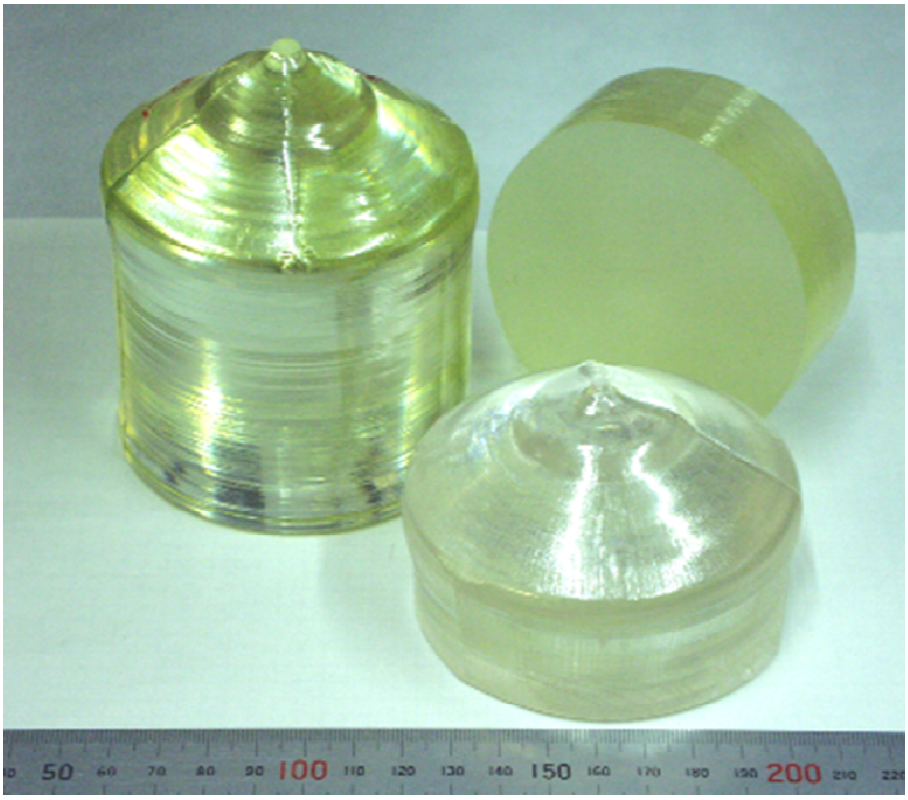

Fig. 3.7 As-grown zero birefringence $LiTaO_3$ crystals. The scale of the ruler is mm.

Conoscopic observation of uniaxial crystals such as $LiTaO_3$ using a polarizing microscope enables convenient characterization of the optical quality of the crystal. Conoscopic figures perpendicular to the optical axis are shown in Fig. 3.8. The observation was done using an optical transmittance microscope (Axio imager A1m; Carl Zeiss) with an objective lens of NA = 0.55. The samples had a thickness of 10 mm.

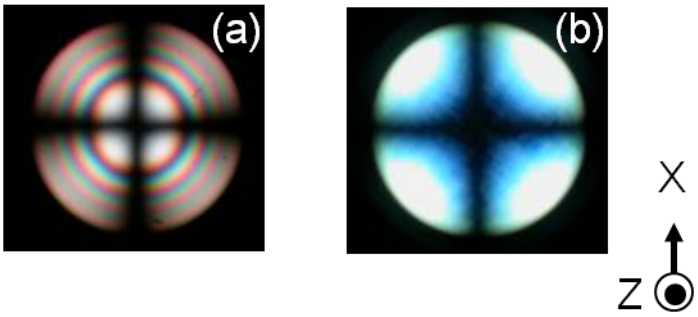

Fig. 3.8 Conoscopic interference patterns of $LiTaO_3$ crystal plates perpendicular to the optical axis (Z): (a) 48.3 mol% (i.e., congruent composition) and (b) 49.5 mol% (i.e., zero birefringence composition).

Interference patterns consist of two phenomena: isogyres and isochromates [16]. Both crystals shown in Fig. 3.8 clearly show isogyres. However, isochromates were not observed for the zero birefringence crystal in the same field of vision. The characteristics of interference patterns depend on many factors including birefringence, refractive index, orientation of the crystal, wavelength, sample thickness, and optical setup. In this case, the smaller birefringence of the crystal resulted in a decrease of the stripe patterns of the isochromates. These results show that the birefringence of $LiTaO_3$ with a [Li]/[Ta] ratio of 0.98 is very small compared with that of congruent $LiTaO_3$.

Fig. 3.9 shows the refractive indices (n_o and n_e) of the zero-birefringence $LiTaO_3$ crystal in the wavelength range from 350 nm to 1200 nm. Both refractive indices are almost the same and exhibit a decreasing trend as the wavelength becomes longer.

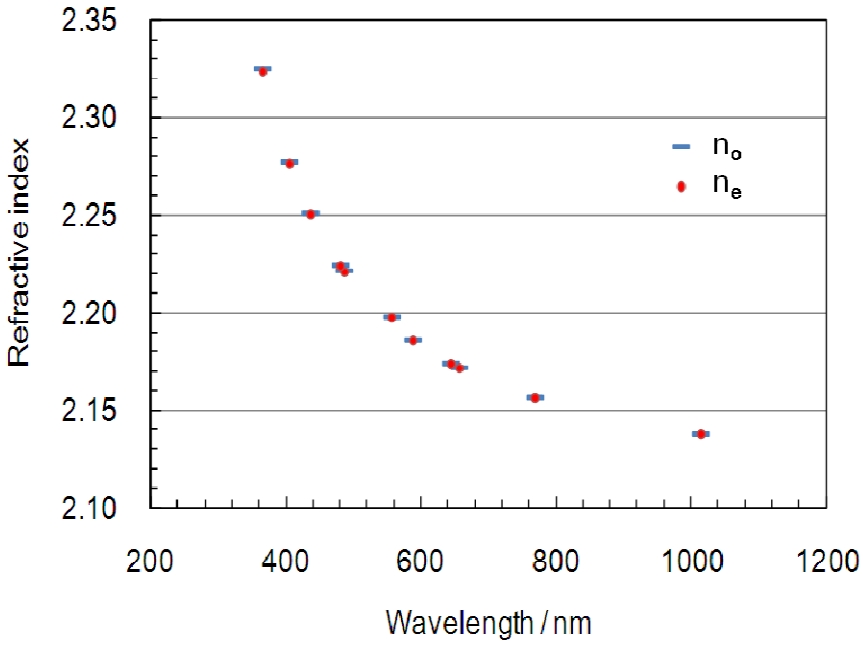

Fig. 3.9 Dependence of refractive indices on wavelength.

Fig. 3.10 shows |Δn| (= $|n_e - n_o|$) of the congruent $LiTaO_3$ and the zero-birefringence $LiTaO_3$ crystal in the wavelength range from 350 nm to 1200 nm. At a given wavelength, Δ*n* of the zero-birefringence $LiTaO_3$ is ten times as small as that of the congruent $LiTaO_3$.

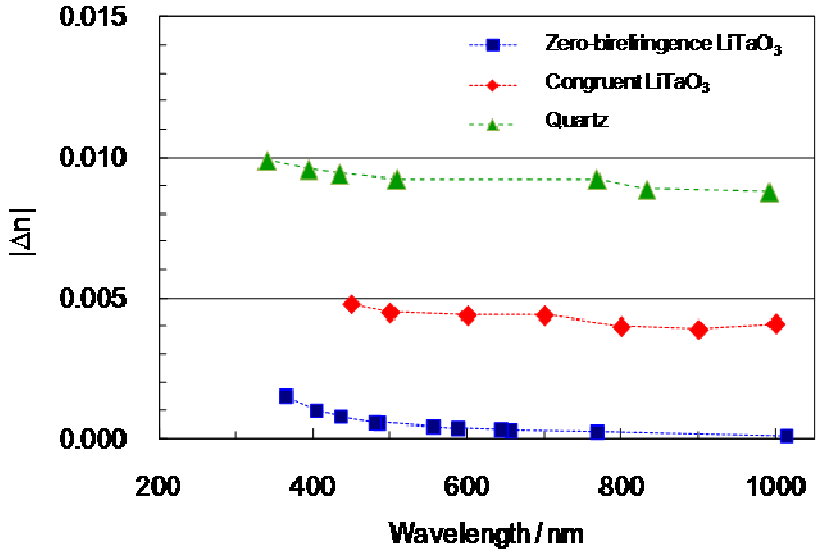

Fig. 3.10 Dependence of birefringence, Δ*n*, on wavelength. Δ*n* values of congruent $LiTaO_3$ were based on data from [10].

Fig. 3.11 shows the homogeneity of the zero-birefringence crystal characterized by the refractive indices. The distributions of refractive indices n_o and n_e along the growing direction of the boule are within ±0.0002.

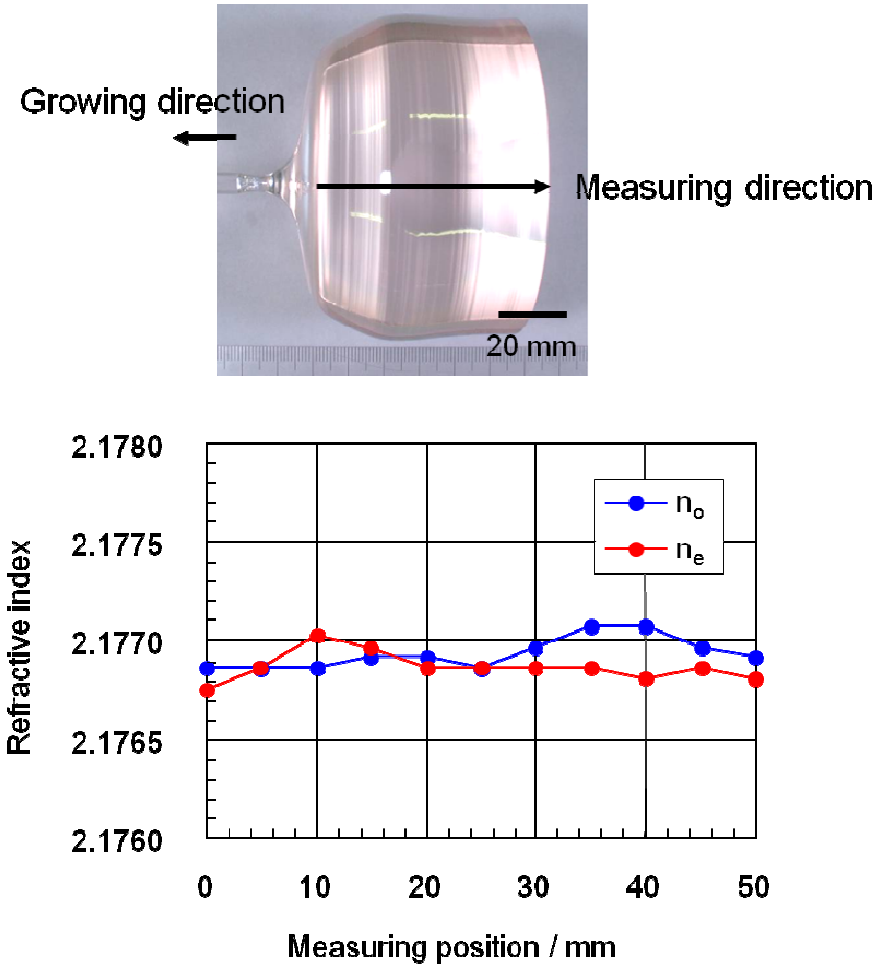

Fig. 3.11 Homogeneity of the refractive indices in the boule along the growing direction.

To evaluate the quality of the crystals, strain observation was carried out under polarized light. Fig. 3.12 shows wafers cut from the body region of the boule perpendicular to the y-axis. Subgrain lines were observed on the plate in Fig. 3.12(a). The crystal shown in Fig. 3.12(a) was grown at the early stage under unoptimized growth conditions. The quality of the crystal is influenced by the temperature field around the growing crystal; stronger fluctuations of temperature in the growth interface lead to the formation of more subgrains during growth. Fig. 3.12(b) shows the crystal grown under optimized conditions; no subgrain is evident.

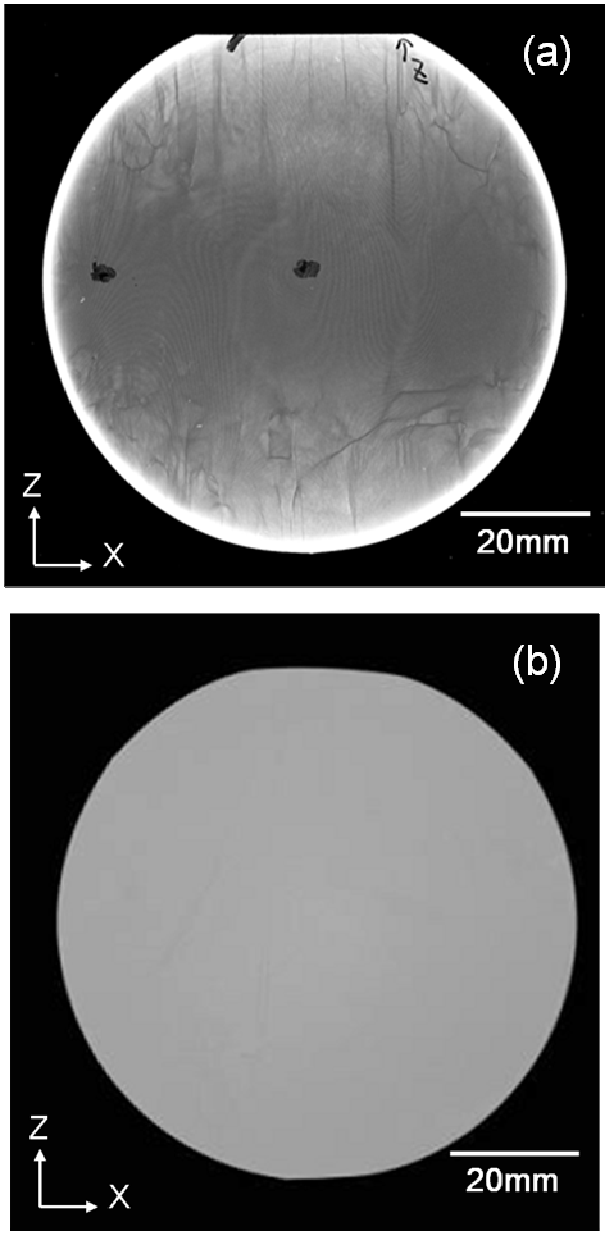

Fig. 3.12 Cross-nicol images of the zero−birefringence $LiTaO_3$ wafers cut from the body part of the boule: (a) crystal grown at the early stage and (b) crystal grown under optimized conditions.

Fig. 3.13 shows the transmittance of the zero-birefringence and congruent crystals on the $\{0\ 1\ \bar{1}\ 0\}$ plane sample at wavelengths in the range of 200–800 nm, measured using a spectrophotometer. The absorption edges of the crystals are 268 and 273 nm, respectively. The relative shift of the spectra is related to the number of defects in the $LiTaO_3$ lattice.

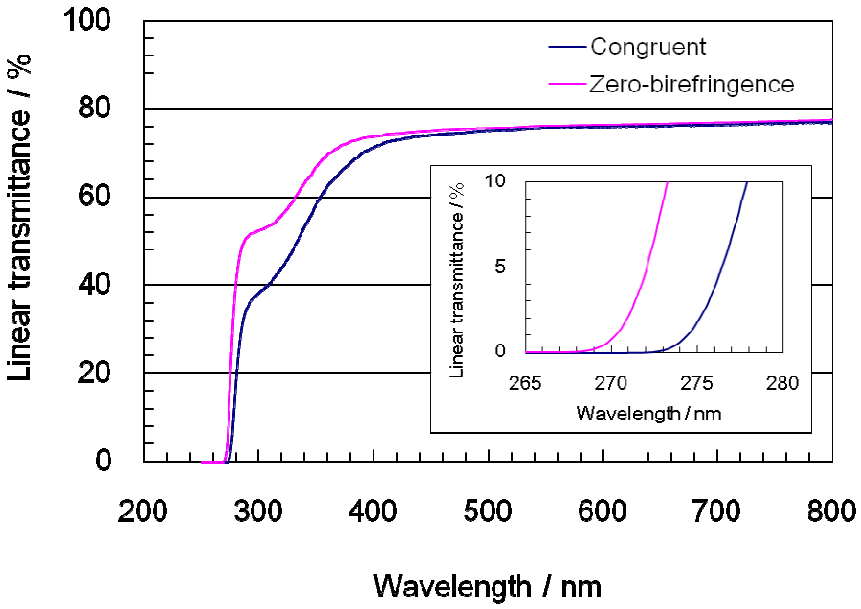

Fig. 3.13 Linear transmittance of the zero birefringence and congruent $LiTaO_3$ crystals. The samples are 2.0 mm thick.

3.6. Applications

3.6.1. Optics applications for transparent materials with high refractive indices

In order to miniaturize optical units and realize optical disk memory with a higher capacity, optics such as lens and prisms require new materials with a high refractive index and a high transmittance in the near–ultraviolet region [17,18]. $LiTaO_3$ also has a high refractive index and transmittance up to the near-ultraviolet region, which are higher than those of glass materials, as shown in Fig. 3.14.

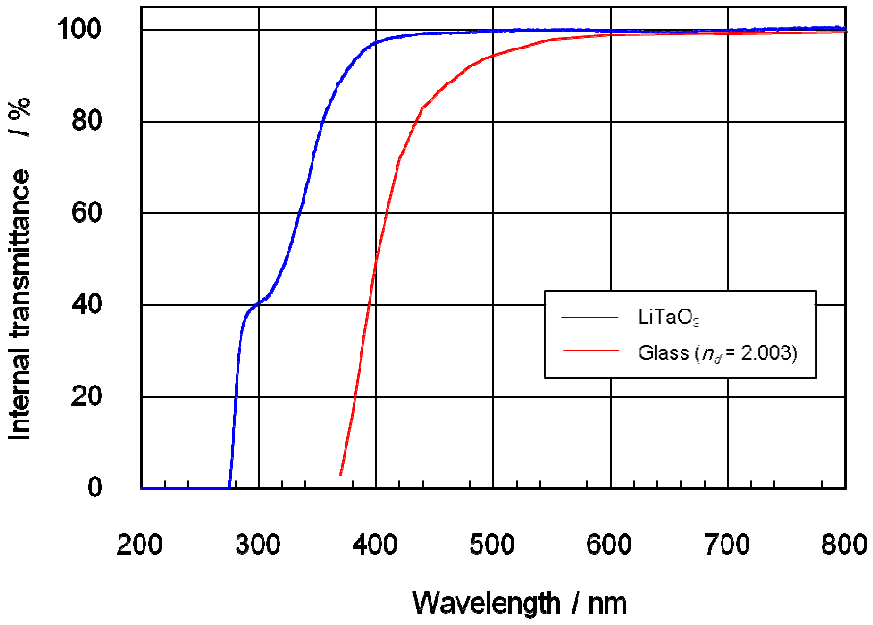

Fig. 3.14 Internal transmittance of the zero-birefringence $LiTaO_3$ single crystal and optical glass with a high refractive index (S-LAH79).

Fig. 3.15 shows the position of $LiTaO_3$ in an Abbe diagram, which is produced by plotting the Abbe number, v_d, of a material versus its refractive index, n_d. The Abbe number is a measure of the dispersion of a material (i.e., the variation of refractive index with wavelength) with respect to the refractive index. Both parameters (v_d and n_d) are very important for the design of optics including lenses, prisms, etc.

The Abbe number, v_d, of a material is defined as follows:

$$v_d = \frac{n_d - 1}{n_F - n_C} \tag{3-1}$$

where n_d, n_F, and n_C are the refractive indices of the material at the wavelengths of the Fraunhofer d-, F-, and C- spectral lines, respectively (i.e., 587.6, 486.1, and 656.3 nm, respectively). From this diagram, it is evident that, like flint glasses, $LiTaO_3$ has optical characteristics such as a large dispersion and high refractive index. However, no glass material has a refractive index as high as that of $LiTaO_3$. Optical materials with higher refractive indices are used to make miniaturized optical components.

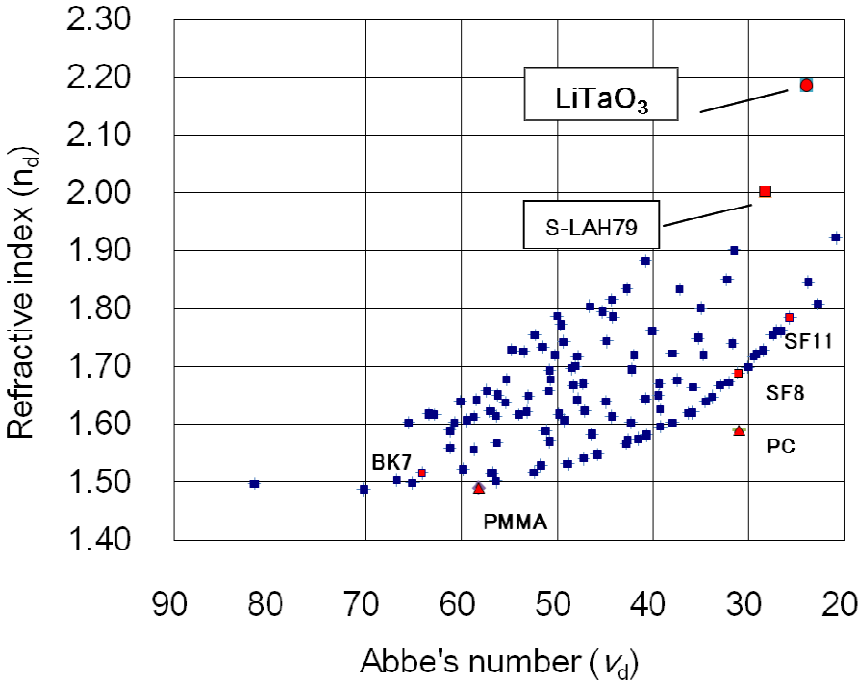

Fig. 3.15 Abbe diagram of the Abbe number versus the refractive index of a range of different glasses including other optically transparent materials. S-LAH79 is a high–refractive-index optical glass produced by OHARA Inc.

Zero-birefringence LT is one of the few materials with both high transmission and a high refractive index. Therefore, this material is expected to be useful for the miniaturization of optical systems (Fig. 3.16).

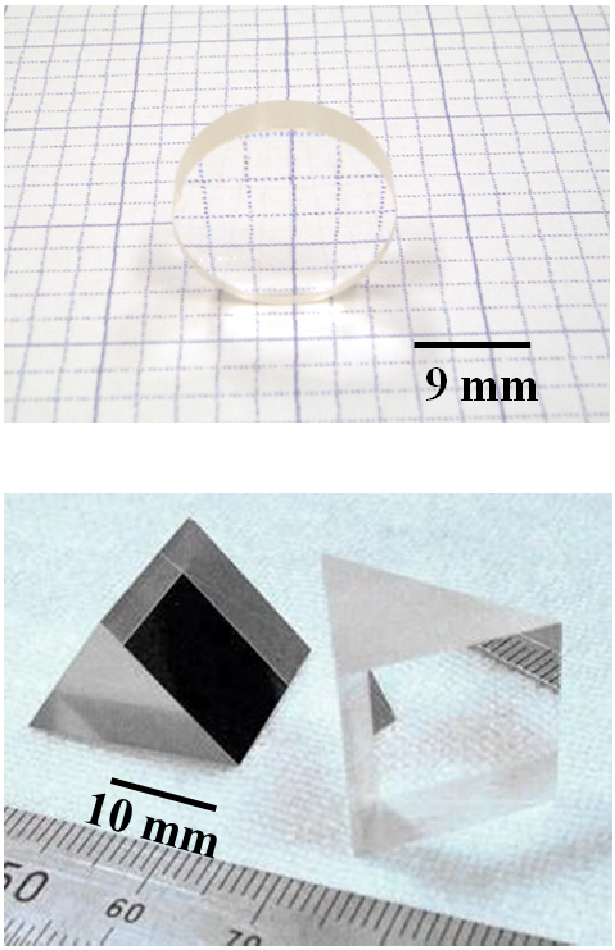

Fig. 3.16 Example of an optical application: Optical plano-convex lens and prisms made of zero-birefringence $LiTaO_3$.

3.6.2. Fabrication of optical polarization modulator using zero-birefringence-controlled $LiTaO_3$ crystal

An optical polarization modulator/controller is a basic yet important device in photonic/quantum electric systems. Optical polarization modulators based on the electro-optic (EO) effect are attractive because they can be operated at high-frequency ranges (>10 GHz) unlike mechanical devices. Several types of EO polarization modulator/controllers have been proposed and implemented. $LiTaO_3$ and $LiNbO_3$ have large r_{42} Pockels coefficients (~30 pm V^{-1}), which are applicable for polarization controller/conversion. A key point for highly efficient polarization control using the r_{42} Pockels coefficient is phase matching between two orthogonally polarized modes with birefringence. Murata et al. proposed a high-speed EO polarization modulator using a double periodic poling structure by adopting quasi-phase matching (QPM) and quasi-velocity matching (QVM) techniques [19].

Fig. 3.17 shows the basic structure of the traveling-wave EO polarization modulator , which consists of a single-mode waveguide and coplanar traveling-wave electrodes fabricated on a z-cut $LiTaO_3$ or $LiNbO_3$ crystal substrate. The light propagation direction is oriented to the x-axis of the $LiTaO_3$ crystal. An electric field for optical modulation is applied along the y-axis across the waveguide, as shown in the cross-sectional view in Fig. 3.16. With this configuration, coupling between the TE and TM modes propagating in the waveguide is induced through the r_{42} Pockels coefficient.

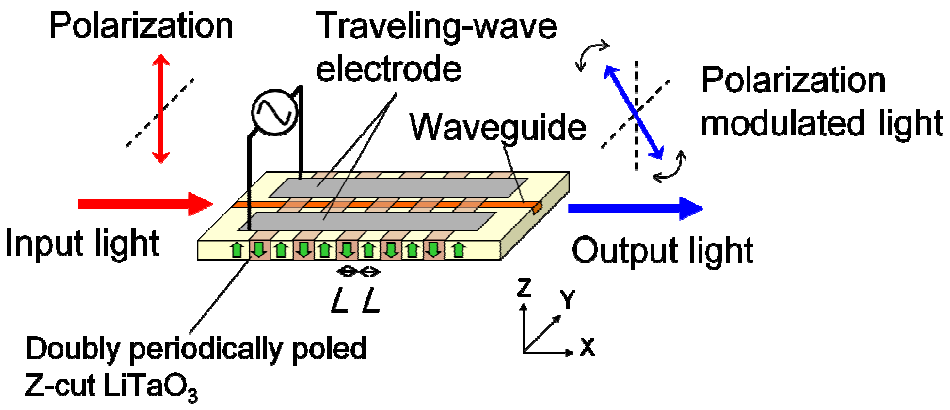

Fig. 3.17 Basic structure of the traveling-wave EO polarization modulator with a double periodic poling structure.

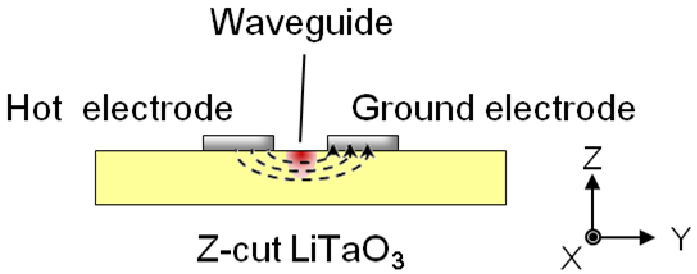

Fig. 3.18 Applied electrical field in a cross section of a Z-cut $LiTaO_3$ crystal.

The polarization reversal period, 2L, for the QPM between the TE and TM modes is determined by using the following equation:

$$2L = \frac{2\pi}{|\beta_{TE} - \beta_{TM}|} \tag{3-2}$$

where β_{TE} and β_{TM} are the propagation constants for the TE and TM modes, respectively. Eq.(3-2) can be also represented as follows:

$$2L = \frac{\lambda}{|N_{TE} - N_{TM}|} \tag{3-3}$$

where N_{TE} and N_{TM} are the effective indices of the fundamental TE and TM modes, respectively, and λ is the free space wavelength of the optical signal. According to Eq. (3-3), a smaller $|N_{TE} - N_{TM}|$ value, i.e., birefringence, leads to a wider polarization reversal period, 2L. For example, 2L is 150–400 μm for $LiTaO_3$ and 7–20 μm for $LiNbO_3$ in the wavelength range of 600–1500 nm, as shown in Table 3.2 The polarization reversal period, 2L, for various substrate materials. Because the birefringence of the zero-birefringence $LiTaO_3$ is one tenth that of the congruent $LiTaO_3$ as shown in Fig. 3.10 and one hundredth that of $LiNbO_3$, the double periodic poling structure can be fabricated and no phase matching, such as is necessary with the polarization reversal structure, is required.

Table 3.2 The polarization reversal period, 2L, for various substrate materials

	Δn	2L (μm)
$LiNbO_3$	0.08	7–20
Congruent $LiTaO_3$	0.004	150–400
Zero-birefringence $LiTaO_3$	≤0.0001	≥8000

Fig. 3.19 Calculated wavelength dependence of EO polarization modulators using $LiTaO_3$ or $LiNbO_3$ with a periodic poling structure.shows the calculated wavelength dependence of polarization modulation for $LiNbO_3$- and $LiTaO_3$-based devices with a periodic poling structure; the center operational wavelength was 1550 nm and the total electrode length for modulation was 10 mm. It is clearly evident that the bandwidth of modulation broadens with smaller birefringence of the substrate.

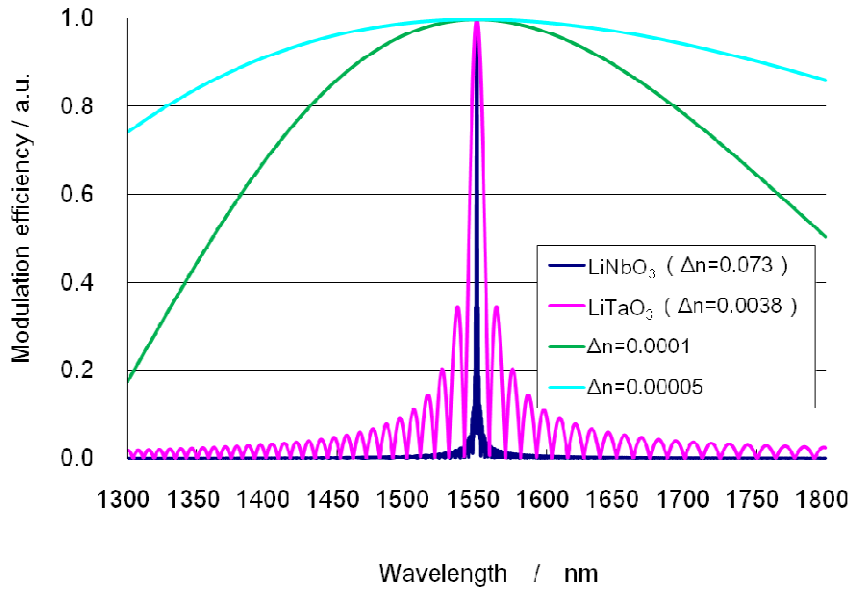

Fig. 3.19 Calculated wavelength dependence of EO polarization modulators using $LiTaO_3$ or $LiNbO_3$ with a periodic poling structure.

3.6.2.1 Experimental procedure

The steps for the fabrication of the designed polarization modulator are as follows. First, a 20 mm long x-propagating optical waveguide was fabricated on a z-cut zero birefringence $LiTaO_3$ crystal substrate using the Ni diffusion method [20]. The thickness and width of the Ni strip used for waveguide fabrication were 35 nm and 5 μm, respectively. The substrate with the Ni strip was sandwiched by two platinum electrodes with the $LiTaO_3$ powder. After being heated at 700 °C for several hours, they were cooled at a rate of 20 °C h^{-1} with an electrical current of ~0.1 mA cm^{-2}. These conditions were determined from the preliminary experimental results of the Ni waveguides to result in a single mode for both TE and TM in the operational wavelength of 1550 nm. Secondly, a 0.2 μm thick SiO_2 buffer layer was deposited on the surface of the substrate using the sputtering method. Finally, 15 mm long Al coplanar electrodes were formed on the surface (Fig. 3.20).

The modulation characteristics of the fabricated optical polarization modulators were tested using linearly polarized light with a wavelength of 1550 nm.

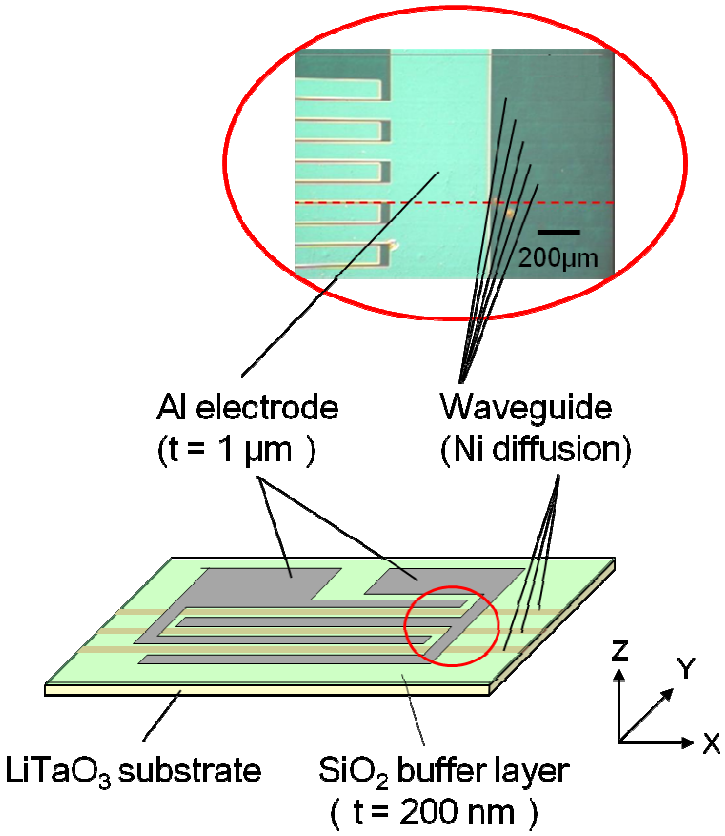

Fig. 3.20 Schematic configuration of the polarization modulator

3.6.2.2 Results and discussion

Fig. 3.21 shows the near-field patterns for 1550 nm laser light through the waveguide. Laser light was coupled into the waveguide using a hemispherical-end fiber. The output end of the waveguide was imaged onto a beam profiler using an objective lens with NA = 0.40. The light propagated through the waveguide by single modes for both TE and TM. From the intensity data of the beam profile, we determined that the difference in the refractive index of the core of the waveguide and the surrounding material is about 1×10^{-3} for the TE mode and 2.5×10^{-3} for the TM mode [21].

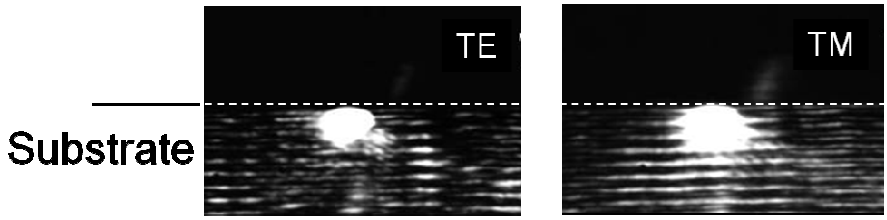

Fig. 3.21 Near-field patterns for 1550 nm light of the waveguide.

The modulation performance was tested using the experimental arrangement shown in Fig. 3.22. The basic measurement system was the same as that used for the near-field patterns. TE polarized input light was coupled to the waveguide through a hemispherical-end fiber.

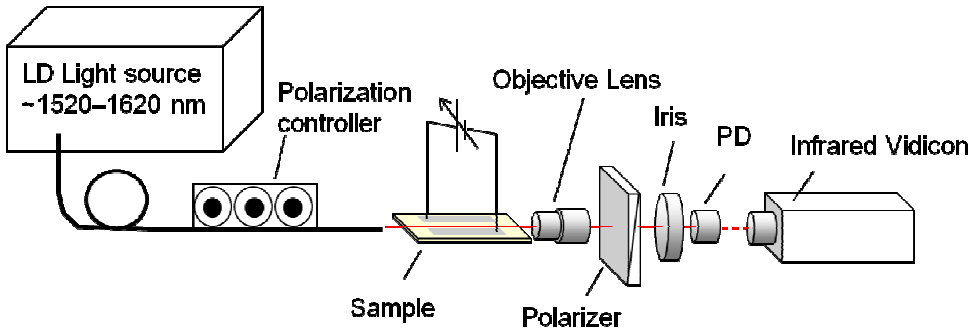

Fig. 3.22 Experimental setup for the modulation measurements.

Fig. 3.23 shows an example of the polarization modulation response after loading with AC voltage at a frequency of 200 Hz. The signal was switched off and on by loading the voltage without the double periodic poling structure for phase matching.

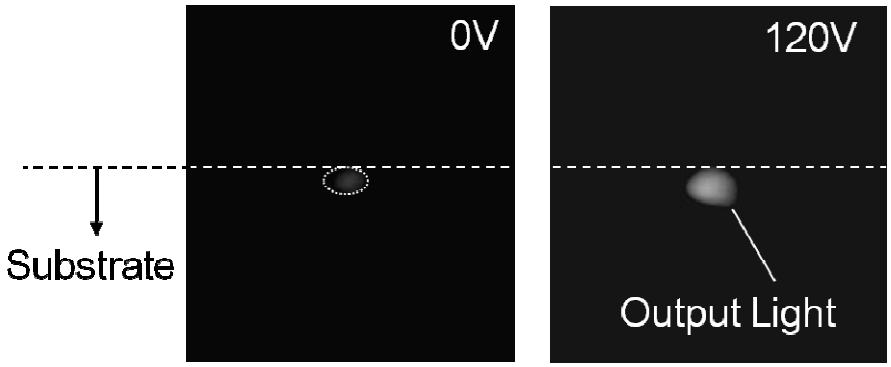

Fig. 3.23 Polarization modulation response to loading of voltage.

Fig. 3.24 shows the modulator performance towards loading with AC with a voltage of ±50 V at a frequency of 200 Hz. The signal followed the loading voltage but gave rise to an asymmetrical curve due to the difference between the index changes for TE and TM that were mentioned above.

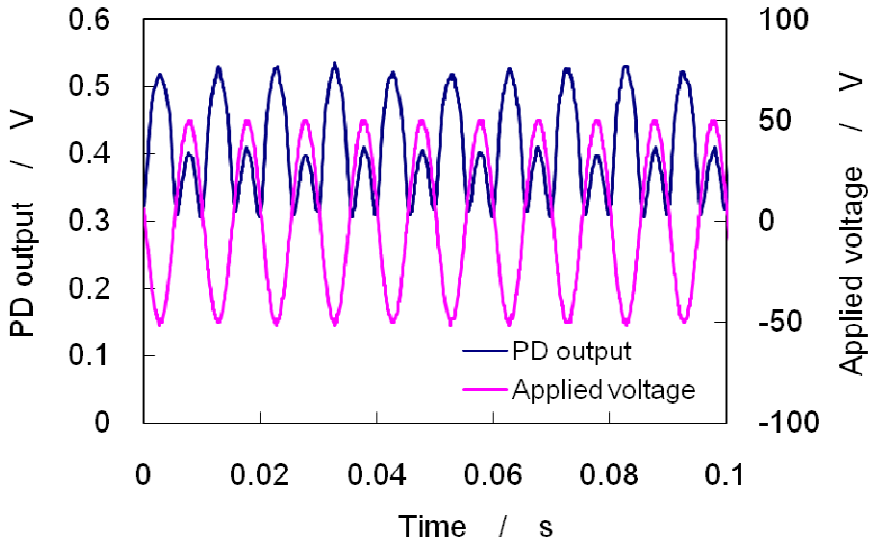

Fig. 3.24 Performance of a modulator at a wavelength of 1550 nm towards the loading of AC voltage with a frequency of 200 Hz.

Fig. 3.25 shows the wavelength dependence of the measured modulation intensity. As shown in Fig. 3.19, a wide range of bandwidths was observed in this modulator using zero birefringence $LiTaO_3$.

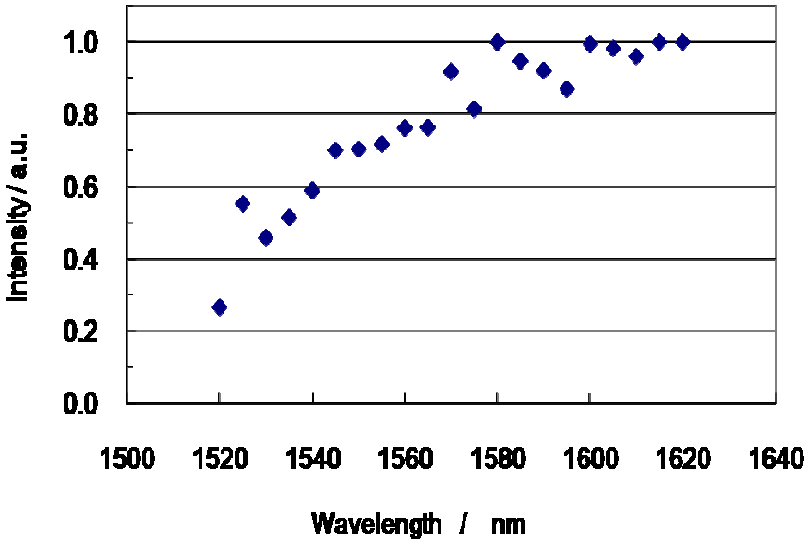

Fig. 3.25 Wavelength dependence of measured modulation intensity.

3.7. Conclusion

Zero-birefringence $LiTaO_3$ single crystals with 80 mm diameters and 80 mm lengths were grown by using the DC-CZ method with an automatic powder supply system. The crystals were grown from an off-congruent Li-rich solution (Li_2O, 55.0 mol%). The crystal was determined to have a chemical composition with a [Li]/[Ta] ratio of 0.98 based on the Curie temperature and refractive indices.

Δn of the zero-birefringence $LiTaO_3$ single crystal is more than ten times smaller than that of a conventional (congruent) $LiTaO_3$ crystal in the visible to near–infrared wavelength region. The homogeneity of the refractive indices (i.e., n_o and n_e) in a boule is within ±0.0002.

Two potential applications for zero birefringence $LiTaO_3$ were proposed. The first is as an optical material for optics such as lenses, prisms, etc. Zero-birefringence $LiTaO_3$ has a high refractive index and transmittance spanning the ultra-violet to visible wavelength range. This is an important characteristic for miniaturizing optical components. The second application is as a material substrate for EO devices such as the optical polarization modulator.

References

[1] Y. Furukawa, K. Kitamura, E. Suzuki, and K. Niwa, J. Cryst. Growth, **197**, 7 (1999).

[2] A. A. Ballman, H. J. Levinstein, C. D. Capio, and H. Brown, J. Am. Ceram. Soc., **50**, 657 (1967).

[3] D. A. Scrymgeour, V. Gopalan, A. Itagi, A. Saxena, and P. J. Swart, Phys. Rev. B, **71**, 13 (2005).

[4] R. S. Weis and T. K. Gaylord, Appl. Phys. A, **37**, 191 (1985).

[5] K. Momma and F. Izumi, J. Appl. Crystallogr., **44**, 1272 (2011).

[6] Y. S. Kim and R. T. Smith, J. Appl. Phys., **40**, 4637 (1969).

[7] D. N. Nikogosyan, *Nonlinear Optical Crystals: A Complete Survey* (Springer, New York, 2005), p. 185.

[8] A. W. Warner, M. Onoe, and G. A. Coquin, J. Acoust. Soc. Am., **42**, 1223 (1967).

[9] P. V. Lenzo, E. H. Turner, E. G. Spencer, and A. A. Ballman, Appl. Phys. Lett., **8**, 81 (1966).

[10] W. L. Bond, J. Appl. Phys., **36**, 4 (1965).

[11] S. Miyazawa and H. Iwasaki, J. Cryst. Growth, **10**, 3 (1971).

[12] I. G. Kim, S. Takekawa, Y. Furukawa, M. Lee, and K. Kitamura, J. Cryst. Growth, **229**, 5 (2001).

[13] J. R. Carruthers, G. E. Peterson, M. Grasso, and P. M. Bridenbaugh, J. Appl. Phys., **46**, 1846 (1971).

[14] H. J. Scheel, J. Cryst. Growth, **13-14**, 560 (1972).

[15] P. K. Tien, R. Ulrich, and R. J. Martin, Appl. Phys. Lett., **14**, 291 (1969).

[16] A. L. Bajor, L. Sałbut, A. Szwedowski, and T. Piatkowski, Rev. Sci. Instrum., **69**, 1476 (1998).

[17] Y. Kintaka, S. Kuretake, N. Tanaka, K. Kageyama, and H. Takagi, J. Am. Ceram. Soc., **93**, 1114 (2010).

[18] M. Shinoda, K. Saito, T. Kondo, M. Furuki, M. Takeda, A. Nakaoki, M. Sasaura, and K. Fujiura, Jpn. J. Appl. Phys., **45**, 1332 (2006).

[19] H. Murata, A. Takahashi, and Y. Okamura, IEICE Trans. Electron., **E92-C**, 5 (2009).

[20] W.-L. Chen, D.-J. Chen, and W.-S. Wang, IEEE Photon. Technol. Lett., **7**, 203 (1995).

[21] I. Mansour and F. Caccavale, J. Lightwave Technol., **14**, 6 (1996).

Chapter 4.

Local Modification of Optical Properties of $LiTaO_3$ Crystal by Irradiation with Focused Femtosecond Laser Pulses

4.1. Introduction

Ferroelectric crystals such as $LiTaO_3$ are important for producing integrated optics with various functions because crystals with channel waveguides can function as modulators , switches, and frequency convertors. $LiTaO_3$ is particularly appropriate for electro-optical applications because its birefringence is about 20 times less than that of $LiNbO_3$. This small birefringence enables the fabrication of modulators with a simple electrode structure [1]. A well known and commercially established process for the fabrication of waveguides is the metal diffusion technique [2]. However, the required heat treatment process prevents the fabrication of waveguides with nonlinear optical effects in $LiTaO_3$ because the temperature required for the diffusion of metal ions (~1000 °C) exceeds the Curie temperature of this crystal (~600 °C); as a result, multiple ferroelectric domains form in the crystal [3].

The direct writing of waveguides using a femtosecond laser is a potential method of fabricating waveguides inside a $LiTaO_3$ crystal while maintaining the single ferroelectric domain. Using this method, a region of a waveguide with a high refractive index can be created by inducing nonlinear ionization inside transparent materials only in the focal volume of the femtosecond laser pulses . To date, various three-dimensional optics such as waveguides [4,5], gratings [6], and couplers [7] have been fabricated

inside a variety of transparent materials using this method.

The localized photoexcitation that is induced inside a transparent solid by a focused femtosecond laser pulse allows thermal energy to diffuse from the photoexcited region at a much faster rate than the material diffusion rate. Therefore, it is expected that the single ferroelectric domain would be preserved in the crystal after photoexcitation by a femtosecond laser pulse. Accordingly, a waveguide with a nonlinear optical effect may be created inside a $LiTaO_3$ crystal using the femtosecond laser writing method.

In this chapter, the formation of a waveguide via direct writing using femtosecond laser pulses is discussed. Additionally, applications using the formed waveguides in $LiTaO_3$ are proposed.

4.2. Experimental procedure

4.2.1. Femtosecond laser writing of waveguides

The experimental setup for femtosecond laser irradiation inside a crystal is shown in Fig. 4.1. The laser pulses used to induce photoexcitation inside the crystal originate from a regeneratively amplified mode-locked titanium:sapphire laser (Coherent MIRA and RegA 9000) operating at a repetition rate of 250 kHz. The pulse duration was controlled in the range of 100–900 fs by operating the pulse compressor in the laser system. The beam was focused inside an x-cut $LiTaO_3$ sample (Yamaju Ceramics) using a ×10 objective lens with a numerical aperture of 0.3 (Nikon LU Plan Fluor). The surface of the sample was optically polished before laser irradiation. In all experiments, the lines of the induced structure (i.e., the waveguides) were formed by

scanning the sample in the beam axis during exposure to laser pulses. In this experiment, the beam axis was parallel to the x-axis of the $LiTaO_3$ crystal. Scanning in the beam axis enabled the formation of a circularly symmetric waveguide because the transverse intensity distribution of the laser pulse is circularly symmetric. The scanning velocity in these experiments ranged from 10–100 μm s^{-1} while the pulse energy ranged from 0.05–2.0 μJ. After writing the waveguides, the end surface of the sample was cut and polished to expose the waveguide on the surface.

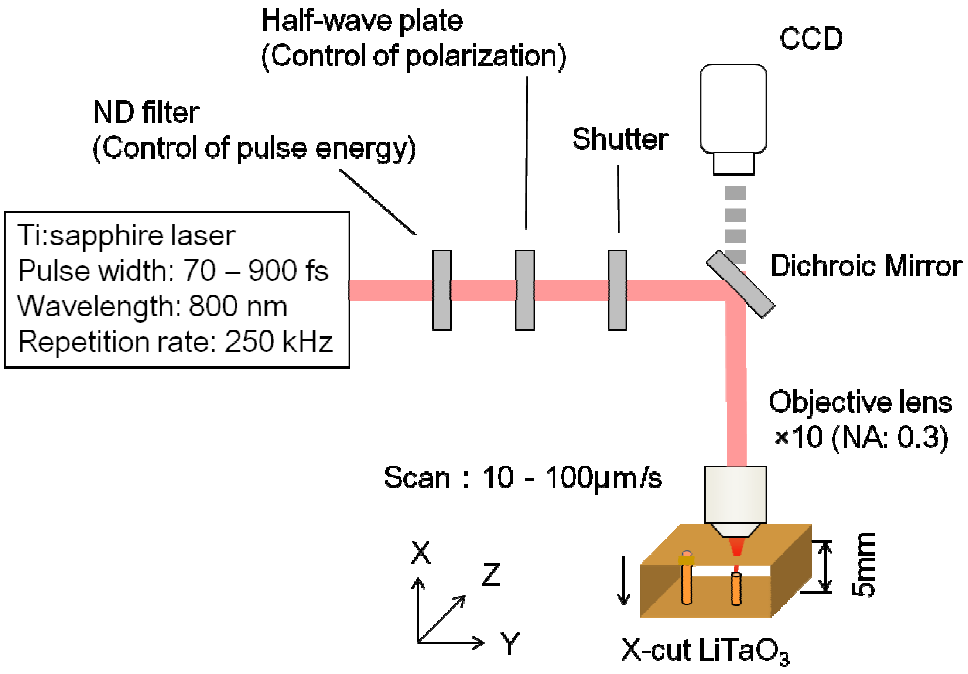

Fig. 4.1 Schematic of the experimental setup.

4.2.2. Analysis of refractive index profiles in waveguides

The refractive index profiles in the waveguides were determined according to the procedure described by Mansour and Caccavale [8]. In this procedure, the distribution of the refractive index change, Δn (y, z), is calculated from the near-field (NF) pattern of the light guided through the waveguide. The field power intensity, I (y, z), of a guided TE-polarized He-Ne laser at the near-field was magnified using an objective lens and imaged on the charge-coupled device of a laser beam profiler (Newport LBP-2). The normalized electric field intensity, A (y, z), was calculated using the following equation:

$$A(\mathrm{y},\mathrm{z}) = \sqrt{\frac{I(y,z)}{\mathrm{I_{max}}(y,z)}} \tag{4-1}$$

where I_{max} (y, z) is the maximum power intensity of the measured NF pattern.

According to ref. [8], Δn (y, z) is given by the following equation:

$$\Delta n(y,z) = \sqrt{n_{\mathrm{s}}^2 - \frac{1}{k^2 A(y,z)}\nabla_{\mathrm{t}}^2 A(y,z)} - n_{\mathrm{s}} \tag{4-2}$$

where k (= $2\pi/\lambda$) is the propagation constant in a vacuum, λ is the wavelength, and n_s is the refractive index of the $LiTaO_3$ crystal. The effective index change, Δn_{eff}, was estimated from the peak-to-valley of the plotted Δn (y, z) values.

4.3. Results and discussion

Fig. 4.2 shows the NF pattern of the light guided through the waveguide written inside a $LiTaO_3$ crystal at a pulse energy of 1.0 μJ, a pulse duration of 200 fs, and a scanning velocity of 10 μm s^{-1}. The pattern was almost Gaussian. The 1/e mode-field diameter along the major axis was about 11 μm with an ellipticity of 0.75. Fig. 4.2(b) shows the Δn (y, z) distribution that was reconstructed from the NF pattern of Fig. 4.2(a). For this experiment, the Δn_{eff} value was determined to be ~7×10^{-4}.

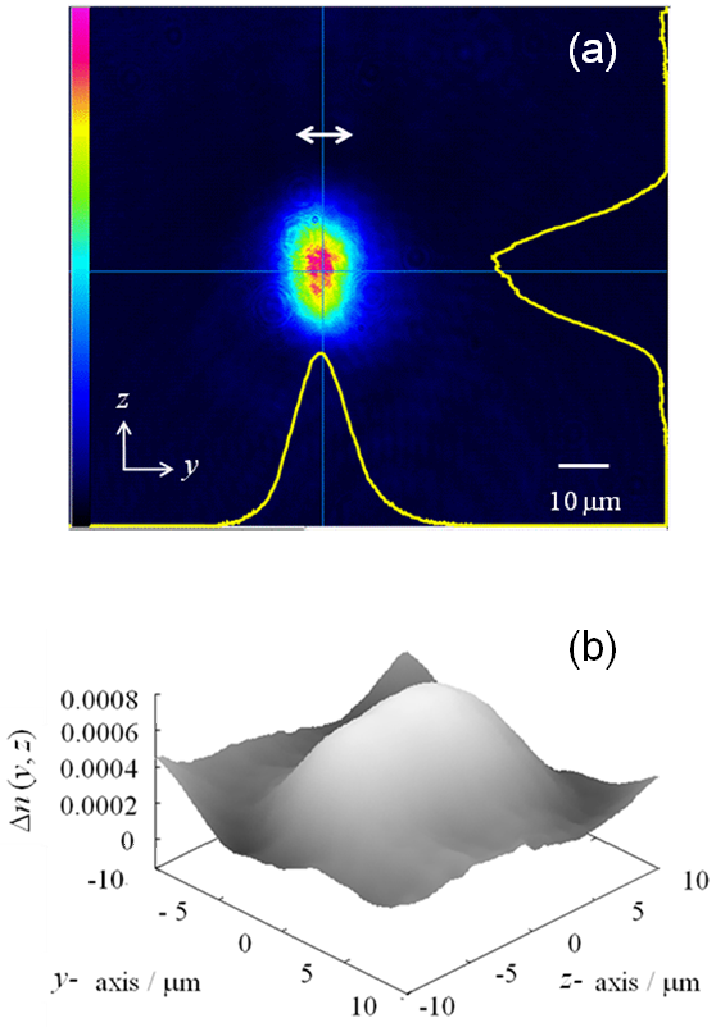

Fig. 4.2 (a) NF pattern for light guided through a waveguide at a pulse energy of 1.0 mJ, pulse duration of 200 fs, and scanning velocity of 10 mm s^{-1}. Double-headed arrows indicate the polarization direction of the guided light. (b) Δn (x,y) distribution calculated from the NF pattern in (a).

Fig. 4.3 shows the NF patterns of light guided through the waveguide written inside a $LiTaO_3$ crystal at various pulse energies and pulse durations. All the writing experiments shown in Fig. 4.3 were carried out at a scanning velocity of 10 μm s^{-1}. It was determined that the guiding performance strongly depends on the pulse energy and pulse duration. To determine the optimal irradiation conditions, we used Δn_{eff} as a parameter. Fig. 4.4 shows a contour map of Δn_{eff} as a function of the pulse energy and pulse duration. Accordingly, the optimal irradiation conditions to obtain maximum Δn_{eff} involve a pulse energy between 0.8 and 1.2 μJ and a pulse duration of 100–200 fs.

From the results shown in Fig. 4.3 and Fig. 4.4, we classified the beam guiding performance of the waveguides into three categories: (a), (b), and (c), as shown in Fig. 4.3. In category (b), clear NF images were observed if the optimal pulse duration was selected. Although NF images could be observed at a shorter pulse duration in category (a), the intensities were much less than those in category (b). In category (c), guiding light was not clearly observed at any pulse duration.

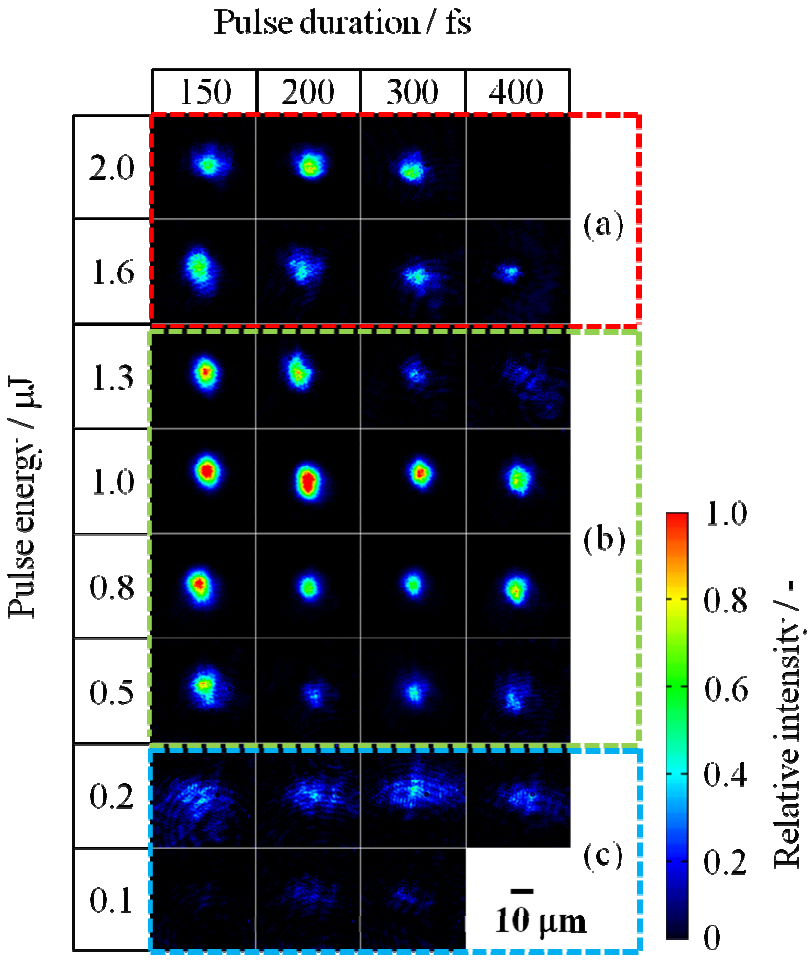

Fig. 4.3 NF patterns for various pulse energies and pulse durations.

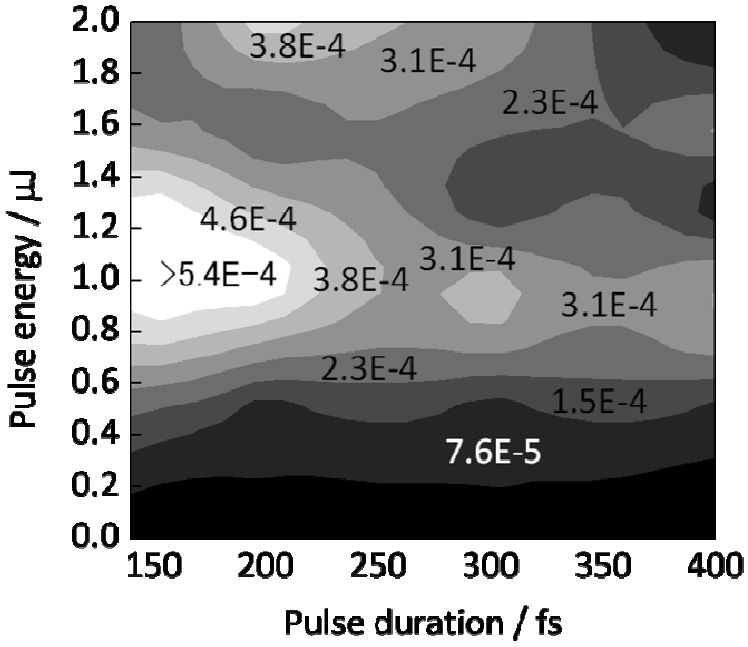

Fig. 4.4 Contour map of Δn_{eff} for various pulse energies and pulse durations at a scanning velocity of 10 μm s^{-1}.

To investigate the relationship between the structure and the guiding performance of the waveguides, representative transmission microscopic images for each category are shown in Fig. 4.5. In category (a), a void-like structural change occurred in the center of the photoexcited region and a surrounding bright region was observed. This suggests that a large thermal expansion occurred in the photoexcited region during laser exposure, which resulted in significant distortion of the surrounding region. In contrast, the structures induced in categories (b) and (c) do not have strong bright regions. In category (b), the central region is a little darker and the surrounding region is a little brighter than the outer regions while only a dark region was observed in category (c). Considering that light guiding was observed in category (b) and not in category (c), this difference suggests that the dark and bright regions are both essential to create a waveguide.

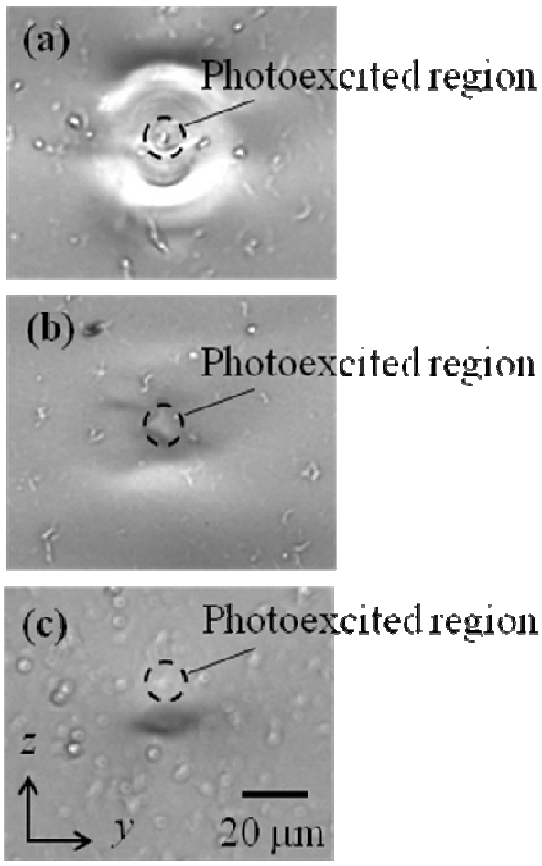

Fig. 4.5 Representative transmission microscope images for each category in Fig. 4.3. Dotted circles indicate the photoexcited regions.

Fig. 4.6 (a) shows the μ-Raman spectrum in the $x(zz)\bar{x}$ configuration measured in the cross section of the waveguide. In this configuration, the Raman spectrum consists of four transverse optical (TO) phonon modes [9]. The spectra in red and blue correspond to the unirradiated and irradiated regions, respectively, as shown in Fig. 4.6 (b). Both spectra exhibited no appreciable changes in the Raman intensity and number of modes. The Raman shift and the line width of the Raman $A_1(TO_4)$ mode observed at ~598 cm^{-1} is focused on, because this mode is isolated from the other modes, which enables facile comparison of the unirradiated and irradiated regions. The spatial map of the line width in Fig. 4.6 (c) suggests that there is no noticeable degradation of the crystal lattice and no change in the crystal orientation after irradiation. A maximum shift of 2 cm^{-1} was observed in the irradiated region, as shown in Fig. 4.6 (d).

From Fig. 4.7, the maximum compressive residual stress was estimated to be 600 MPa based on Reference [10]. We believe that this local compressive stress is closely related to the increase in Δn in the irradiated region.

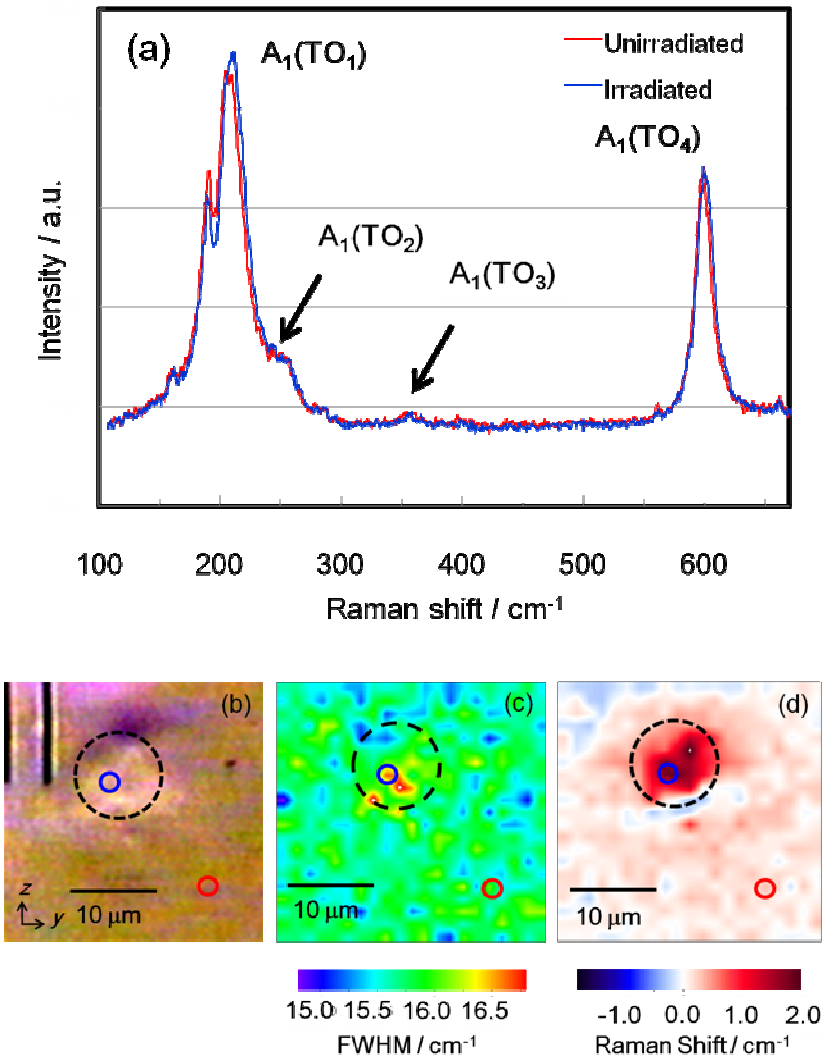

Fig. 4.6 (a) Raman spectrum of the $x(zz)\bar{x}$ configuration, (b) transmitted microscope image, (c) spatial map showing the line width, and (d) the Raman shift for the $A_1(TO_4)$ mode at the waveguide cross section. The dotted circles in (b), (c), and (d) indicate the position of the waveguide.

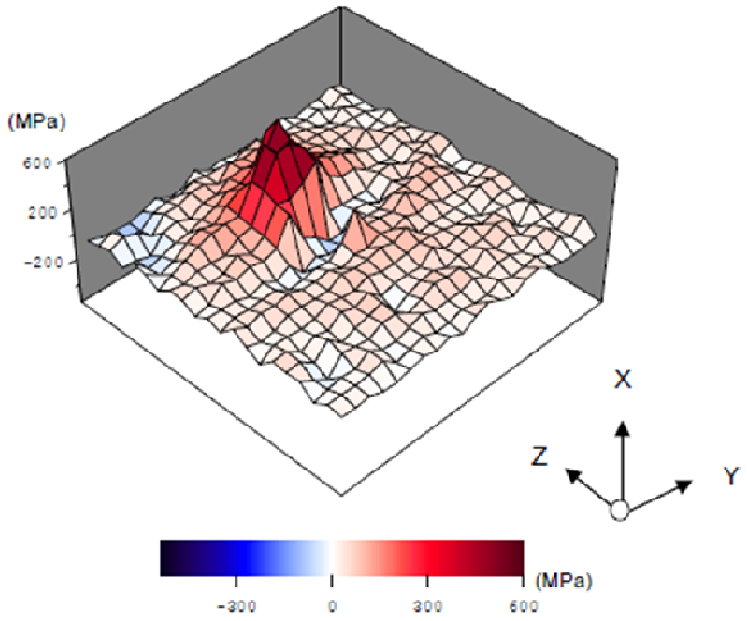

Fig. 4.7 Distribution of stress corresponding to Fig. 4.6 (b).

Observing the structure with a polarized microscope elucidates the origins of the bright and dark regions in the transmission microscope images; the direction of stress cannot be determined from the μ-Raman measurements. The images of the structure formed at a pulse energy of 1.0 μJ and a pulse duration of 200 fs were observed using a polarized microscope at a wavelength of 546 nm with a liquid-crystal universal compensator (LC-PolScope CRi) [11]. Using this microscope, the retardance as well as the slow axis azimuth can be obtained by analyzing the images captured at various settings of the liquid-crystal universal compensator. Fig. 4.8 (a–c) show the transmission image, the corresponding retardance, and the azimuth distributions of the birefringence of the structure, respectively. In Fig. 4.8 (c), the color indicates the slow axis azimuth of the birefringence. Because birefringence can be generated by loading stress in the slow axis, the azimuth indicates the direction of stress. Therefore, Fig. 4.8 (c) indicates that the stress was loaded in the y-direction in the central region and that compression occurred in that direction. Because compression in one direction generates expansion in the corresponding vertical direction, it is expected that the surrounding region was compressed in the z-direction, which results in birefringence of the slow axis in the z-direction. In the transmission image, the darker region likely originated from the material compressed in the y-direction while the bright region likely corresponds to the material compressed in the z-direction.

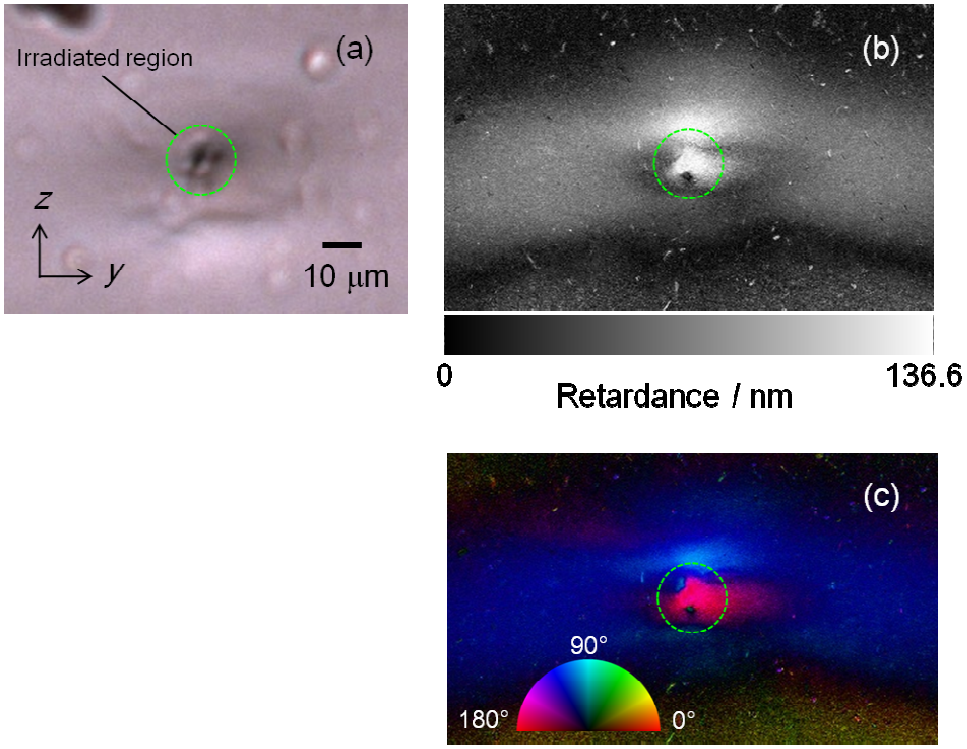

Fig. 4.8 (a) Transmission microscope image, (b) corresponding retardance distribution of the birefringence, and (c) distribution of slow axis azimuth of the birefringence of the structure. The colored spoke of the semicircular wheel in (c) indicates the slow axis azimuth of the birefringence.

The birefringence observed using the polarized microscope indicated that the polarization dependence of light guiding in the waveguide should be examined. Fig. 4.9 shows the intensity of the guided linearly polarized light through the waveguide plotted against the polarization direction, θ. The light was most intense when the polarization direction was parallel to the y-axis. The polarization-dependent intensity was fitted by $I_0\cos(2\theta)$ (i.e., the solid curve in Fig. 4.9), which indicates that only light polarized in the y-direction can be guided through the waveguide in a $LiTaO_3$ crystal. The origin of the polarization dependence can be explained by the birefringence in the waveguide. Observations using the polarized microscope showed that the slow axis of the birefringence in the waveguide was parallel to the y-axis; therefore, this birefringence should select only y-polarized light.

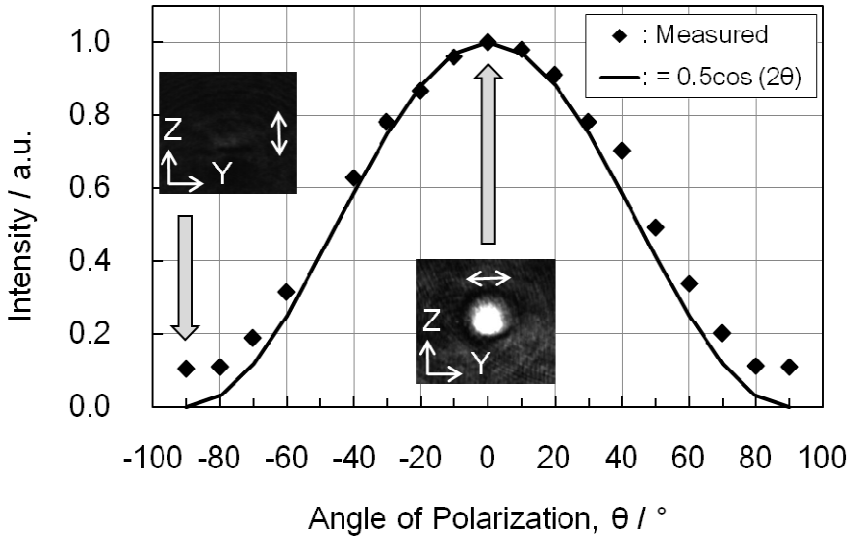

Fig. 4.9 Polarization dependence of waveguide on guided linearly polarized light. Double-headed arrows indicate the polarization direction of the guided light.

4.4. Applications

4.4.1. SHG light through waveguide

It was discovered that second-harmonic light can be generated by guiding a strong laser beam through the waveguide. We used a Nd:YVO_4 laser operating at 700 mW to directly input incident light at a wavelength of 1064 nm directly into the induced structure of the sample without using a phase-matching structure such as quasi-phase matching (QPM)(Fig. 4.10). Fig. 4.11 shows the SHG performance of the induced structures formed at a pulse energy and pulse duration of 1.0 μJ and 200 fs, respectively. This figure confirms that the ferroelectric properties were preserved after photoexcitation by femtosecond laser pulses.

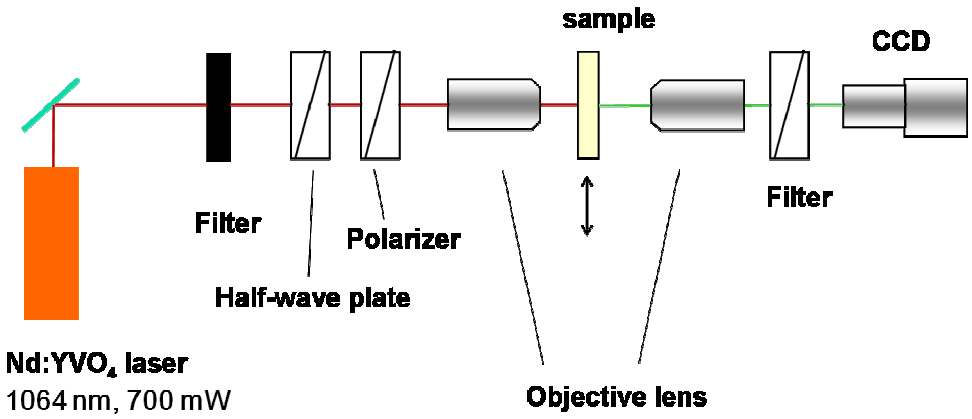

Fig. 4.10 SHG observation setup for optical waveguides written in $LiTaO_3$ using femtosecond laser pulses.

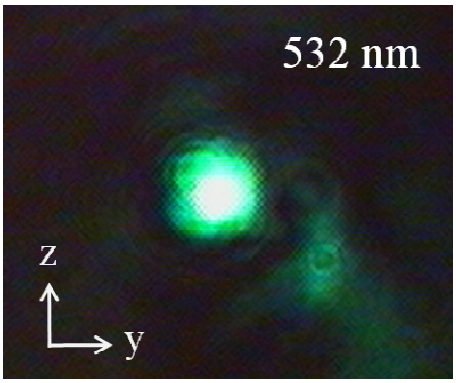

Fig. 4.11 SHG performance of induced structure.

4.4.2. Fabrication of optical polarization modulator using $LiTaO_3$ with direct writing waveguide

Metal diffusion waveguides are widely used for optical modulators, optical switches, and so on [2]. The waveguide fabricated by irradiation with femtosecond laser pulses is also expected to work as a light guide for EO optical devices.

For EO devices, direct writing of a waveguide using femtosecond laser pulses was performed using a $LiTaO_3$ wafer, as shown in Fig. 4.12. In this case, an objective lens with an NA of 0.8 was focused 50–100 μm beneath the surface of the z cut of the $LiTaO_3$ substrate. The substrate was translated along the x direction at a speed of 10–500 μm s^{-1}, as shown in Fig. 4.12.

Fig. 4.13 shows the transmission optical microscope image of the cross section of a $LiTaO_3$ substrate with an induced structure and the near field pattern for 632.8 μm laser light through the waveguide. The induced structure acts as a waveguide, and both TE and TM modes were propagated. The cross-sectional shape of the structure is elliptical, which is due to the incident direction of the writing beam.

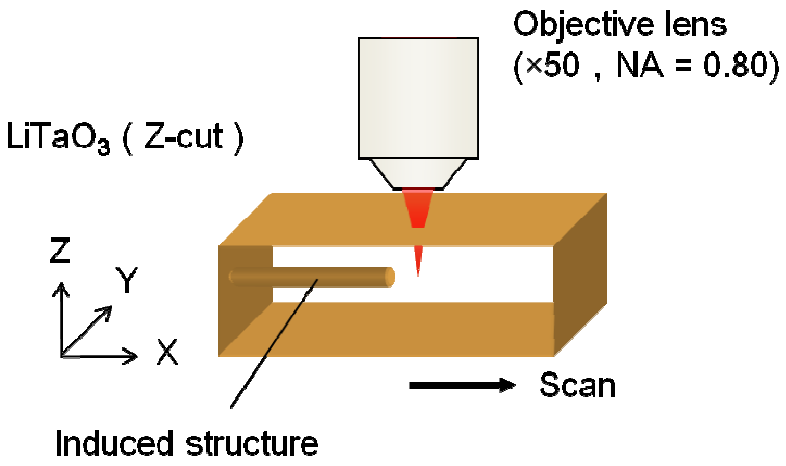

Fig. 4.12 Schematic of the writing procedure of a waveguide for the modulator using a femtosecond laser. The $LiTaO_3$ wafer was translated at 10–500 μm s^{-1} perpendicular to the incident direction.

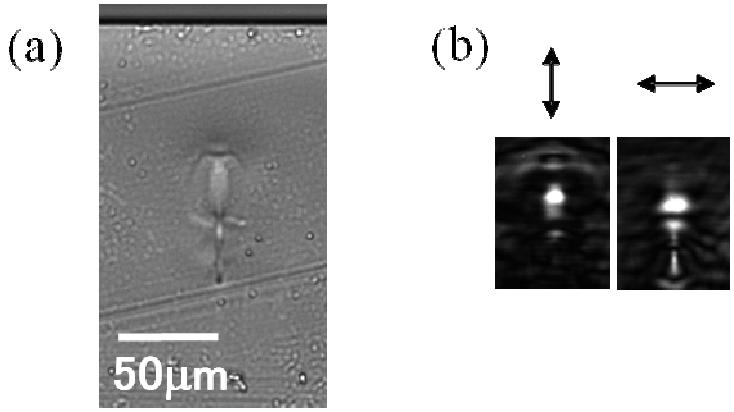

Fig. 4.13 (a) Transmission optical microscopic image of the waveguide from the cross-sectional perspective, and (b) image of the near-field output light of the waveguide for orthogonal light.

Next, the formed waveguides were examined to determine whether they are suitable for practical use. An optical polarization modulator was fabricated using the substrate imprinted with the waveguide by direct writing. Fig. 4.14 shows the structure of the optical polarization modulator. It consists of a waveguide and electrodes, which formed both principal planes (z cut).

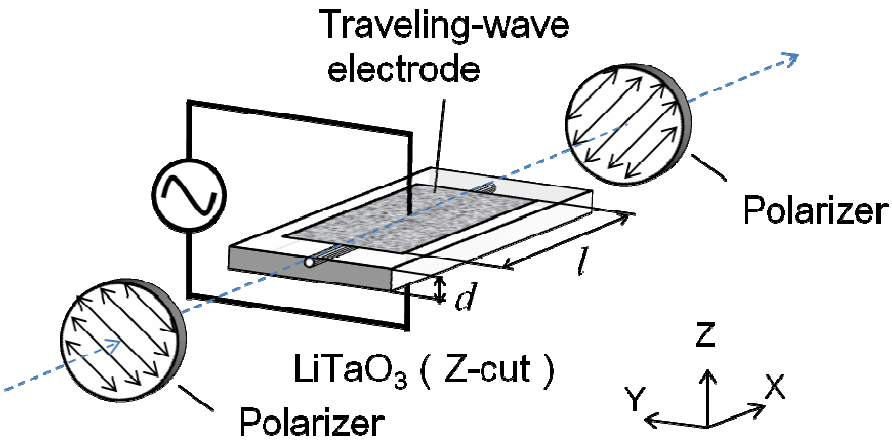

Fig. 4.14 Schematic illustration of the modulator.

Fig. 4.15 shows the modulation response of the modulator using a direct writing waveguide. The loading voltage for the operation was ±50 V with a frequency of 150 Hz. The light wavelength was 632.8 nm.

The modulation signal followed the loading AC voltage. From the results shown in Fig. 4.15, the half-wave voltage, V_π, was estimated to be 55 V; V_π is defined according to Eq. (4-3), which can be used to calculate the complex electro-optic constant, r_c.

$$V_\pi = \frac{\lambda d}{n_e^3 r_c l} \tag{4-3}$$

Alternatively, the complex electro-optic constant, r_c, can be calculated using the following equation:

$$r_c' = r_{33} - \left(\frac{n_o}{n_e}\right) r_{13} \tag{4-4}$$

where r_{33} is 30.3 pm V^{-1} and r_{13} is 7.0 pm V^{-1} according to literature data [12].

Via Eqs. (4-3) and (4-4), r_c and r_c' were determined to be 22.2 and 23.3 pm V^{-1}, respectively. Because both values are similar, the waveguide worked effectively.

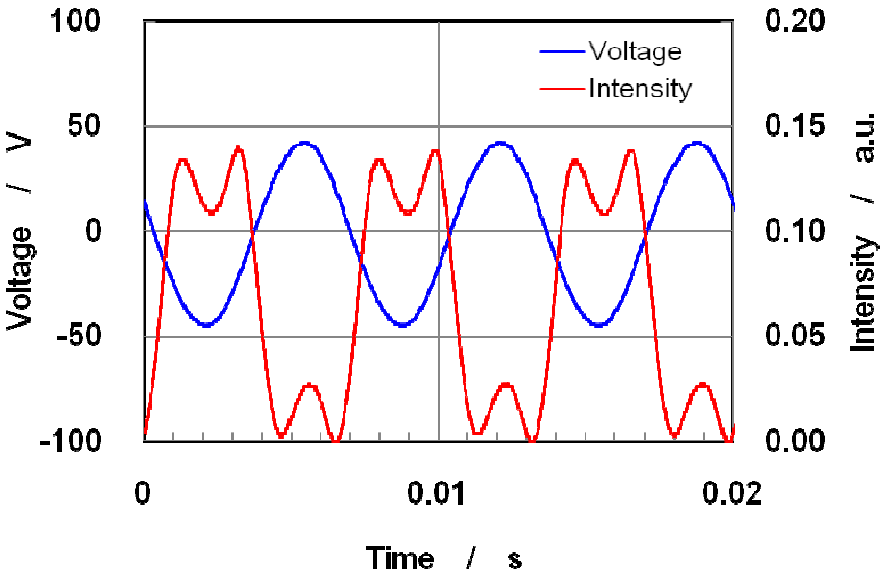

Fig. 4.15 Measured signal of $LiTaO_3$ modulator for the loading voltage of ± 50V.

4.5. Conclusion

An optical waveguide was successfully written inside a $LiTaO_3$ crystal by irradiation with focused femtosecond laser pulses. The optimal conditions to obtain maximum refractive index changes were determined by writing waveguides using different pulse energies and pulse durations. The polarization selectivity of the waveguide is attributed to the birefringence in the guiding region due to stress distribution around the photoexcited region.

A non-linear optical device, i.e., SHG, and an electro-optical device, i.e., polarization modulator, incorporating waveguides fabricated by irradiation with femtosecond laser pulses were investigated. Both devices were successful.

References

[1] H. Murata, A. Takahashi, and Y. Okamura, IEICE Trans. Electron., **E92-C**, 5 (2009).

[2] R. V. Schmidt and I. P. Kaminow, Appl. Phys. Lett., **25** (1974).

[3] W.-L. Chen, D.-J. Chen, and W.-S. Wang, IEEE Photon. Technol. Lett., **7**, 203 (1995).

[4] K. M. Davis, K. Miura, N. Sugimoto, and K. Hirao, Opt. Lett., **21**, 3 (1996).

[5] K. Miura, J. Qiu, H. Inouye, T. Mitsuyu, and K. Hirao, Appl. Phys. Lett., **71**, 3 (1997).

[6] N. Takeshima, Y. Narita, S. Tanaka, Y. Kuroiwa, and K. Hirao, Opt. Lett., **30**, 3 (2005).

[7] W. Watanabe, T. Asano, K. Yamada, K. Itoh, and J. Nishii, Opt. Lett., **28**, 3 (2003).

[8] I. Mansour and F. Caccavale, J. Lightwave Technol., **14**, 6 (1996).

[9] Y. Repelin, E. Husson, F. Bennani, and C. Proust, J. Phys. Chem. Solids, **60**, 7 (1999).

[10] A. Jayaraman and A. A. Ballman, J. Appl. Phys., **60**, 3 (1986).

[11] R. Oldenbourg, Nature, **381**, 811 (1996).

[12] P. V. Lenzo, E. H. Turner, E. G. Spencer, and A. A. Ballman, Appl. Phys. Lett., **8**, 81 (1966).

Summary

In the present study, the author focused on the modification of single crystals to either improve their electrical and optical characteristics or increase their functionality. Initial approaches include the substitution of metal ions into the crystal lattice and composition control, which is similar to successful approaches for the synthesis of functional ceramics. However, direct modification by femtosecond laser pulses was eventually employed. Because oxide single crystals are transparent, lasers can be used as powerful modification tools.

In Chapter 1, the author reviewed three important technologies or techniques related to this thesis. The first two technologies are concerned with crystal growth. One is the Czochralski method, which is one of the most suitable and widely applied techniques for the production of crystal materials for electrical and optical components. Another method is the DC-CZ method, which enabled us to obtain an ideal material. The femtosecond laser is a new tool for the modification of transparent materials such as single crystals.

In Chapter 2, traditional approaches for substitution into the crystal were performed. Piezoelectric properties such as the piezoelectric constants and electromechanical coupling factors were improved by substituting Ga in the langasite structure with Al. Here, the author defined elemental substitution as one of the modifications that involved the appropriate selection of a substitution element to improve the piezoelectric properties.

In Chapter 3, the author discussed a new $LiTaO_3$ single crystal with

zero-birefringence indices. $LiTaO_3$ with zero birefringence has already been reported, but no studies concerning the growth of the crystal for practical applications have been published. In this study, we grew a large $LiTaO_3$ crystal with zero birefringence using the DC-CZ method. The author also fabricated an EO polarization modulator using the $LiTaO_3$ wafer that had excellent performance.

In Chapter 4, the author applied the femtosecond laser as a new tool for crystal modification to fabricate waveguides. The index change of the waveguide fabricated using this method was a tenth of that of conventional methods such as metal diffusion. However, wavelength conversion and polarization modulation performance were successfully demonstrated.

List of Publications

Chapter 1

1. K. Shimamura, **M. Kumatoriya**, and T. Fukuda: Journal of Crystal Growth, **147**, pp.99-103 (1995) “Effect of starting melt composition on crystal growth of calcium niobium gallium garnet.”

2. H. Sato, **M. Kumatoriya**, and T. Fujii: Journal of Crystal Growth, **242**, pp.177-182 (2002) “Control of the facet plane formation on solid-liquid interface of LGS.”

Chapter 2

3. T. Fukuda, H. Takeda, K. Shimamura, H. Kawanaka, **M. Kumatoriya**, S. Murakami, J. Sato, and M. Sato: Proceedings of the eleventh IEEE international symposium on applications of ferroelectrics, ISAF 98, 315–319 (1998) “Growth of New Langasite Single Crystal for piezoelectric Applications.”

4. V. V. Kochurikhin, **M. Kumatoriya**, K. Shimamura, H. Takagi, and T. Fukuda: Journal of Crystal Growth, **181**, 452–454 (1997) “Czochralski growth of $Sr_3Ga_2Ge_4O_{14}$ single crystals for piezoelectric applications.”

5. H. Takeda, R. Uecker, **M. Kumatoriya**, K. Shimamura, P. Reiche, and T. Fukuda: Crystal Research and Technology, **32**, 939–945 (1997) “Growth and Characterization of $Na_2Ca_2Ge_6O_{14}$ Single Crystals.”

6. M. Kadota, J. Nakanishi, T. Kitamura, and **M. Kumatoriya**: Proceedings of 1998 IEEE Ultrasonic symposium, **1**, 311–314 (1998) “Surface Acoustic Wave Properties on Various Rotated Y-cut Langasite Crystal Substrates Grown by Czochralski Method.”

7. M. Kadota, J. Nakanishi, T. Kitamura, and **M. Kumatoriya**: Japanese Journal of Applied Physics, **38**, 3288–3292 (1999) “Properties of Leaky, Leaky Pseudo, and Reyleigh Surface Acoustic Waves on Various Rotated Y-cut Langasite Crystal Substrate.”

8. **M. Kumatoriya**, H. Sato, J. Nakanishi, T. Fujii, M. Kadota, and Y. Sakabe: Journal of Crystal Growth, **229**, 289–293 (2001) “Crystal Growth and Electromechanical Properties of Al Substituted Langasite ($La_3Ga_{5-x}Al_xSiO_{14}$).”

9. H. Takeda, **M. Kumatoriya**, and T. Shiosaki: Applied Physics Letters, **79**, 4201–4203 (2001) “Effect of Aluminum Substitution in $La_3Ga_5SiO_{14}$ Crystals on their Structure and Piezoelectricity.”

10. H. Takeda, **M. Kumatoriya**, and T. Shiosaki: Key Engineering Materials, **216**, 43–46 (2002) “Structure and Piezoelectric Properties of Al-substituted Langasite ($La_3Ga_{5-x}Al_xSiO_{14}$) crystals.”

Chapter 3

11. **M. Kumatoriya**, H. Sato, T. Takagi, M. Nakamura, S. Takekawa, M. Geho, T. Fujii, and K. Kitamura: Journal of Crystal Growth, in press, “Growth and Optical Characterization of Zero-birefringence Controlled $LiTaO_3$ Crystal for High Refractive Index Applications.”

12. **M. Kumatoriya**, T. Takagi, J. Ushizawa, and M. Geho: Journal of Crystal Growth, to be submitted (2011) “Effect of Heavy MgO Doping on Improving Optical Properties of Zero-Birefringence Controlled $LiTaO_3$ Crystal.”

13. **M. Kumatoriya**, H. Murata, Y. Okamura, M. Geho, and N. Wada: “Optical Polarization Modulator Using Zero-Birefringence Controlled $LiTaO_3$ Crystal,” to be submitted.

Chapter 4

14. **M. Kumatoriya**, M. Nakabayashi, M. Sakakura, Y. Shimotsuma, T. Fujii, K. Miura, and K. Hirao: Optical Review, **18**, 166–170 (2011), “Optical Properties of a Waveguide Written Inside a $LiTaO_3$ Crystal by Irradiation with Focused Femtosecond Laser Pulses.”

15. **M. Kumatoriya**, M. Nakabayashi, K. Miura, K. Hirao, and A. Ando: IOP Conf. Series: Materials Science and Engineering **18**, 102004 (2011) “Characterization of Structures Induced in $LiTaO_3$ by Femtosecond Laser Pulses.”

Acknowledgments

The present dissertation was carried out under the direction of Professor Kazuyuki Hirao at the Graduate School of Engineering at Kyoto University.

First, the author wishes to express his sincere gratitude to Professor Kazuyuki Hirao of Kyoto University for his helpful advice and discussions. The author also expresses his gratitude to Professor Kiyotaka Miura and Professor Katsuhisa Tanaka of Kyoto University for their instructive suggestions.

Much gratitude goes to Dr. Hiroshi Takagi, Vice President and Director of Materials Department Group of Murata Manufacturing Co., Ltd. for providing the opportunity to the author for conducting this study. The author wishes to express his grateful thanks to Mr. Tsuneo Murata, President of Murata Manufacturing Co., Ltd. for allowing the author to continue this study. The author is grateful to Mr. Hideharu Ieki, Executive Vice President and Director of Technology & Business Development unit of Murata Manufacturing Co., Ltd. for his understanding and for enabling the author to continue this study. The author also expresses his true gratitude to Dr. Yukio Sakabe, former Executive Vice President of Murata Manufacturing Co., Ltd., Dr. Michio Kadota, Director of Kadota's Laboratory of Murata Manufacturing Co., Ltd., and Mr. Takashi Fujii, Manager of the Product Development Department of Murata Manufacturing Co., Ltd. for giving precise advice and encouragement. In addition, the author expresses his special thanks to Dr. Akira Ando, General Manager of the Functional Materials Research Department of Murata Manufacturing Co., Ltd. for his considerable assistance and helpful advice. The author also would like to thank Mr. Nobuyuki Wada, General

Manager of the Analysis Center of Murata Manufacturing Co., Ltd. and Dr. Keisuke Kageyama, General Manager of Research Center for Next Generation Technology of Murata Manufacturing Co., Ltd. for their support.

The author is also grateful to Professor Tsuguo Fukuda of Tohoku University, Professor Emeritus Mitsuru Ishii of the Shonan Institute of Technology, Fellow Dr. Kenji Kitamura of the National Institute for Material Science, and Professor Yasuyuki Okamura of Osaka University for their valuable and strict guidance. Group leader Dr. Kiyoshi Shimamura, Dr. Shunji Takekawa, and Dr. Masaru Nakamura of the National Institute for Material Science, Associate Professor Hiroaki Takeda of the Tokyo Institute of Technology, Associate Professor Hiroshi Murata of Osaka University, and Dr. Vladimir V. Kochurikhin of the Science Academy of Russia are gratefully acknowledged for their useful discussions and technical advice. The profitable discussions and suggestions from Associate Professor Dr. Yasuhiko Shimotsuma, Dr. Masaaki Sakakura, and Mr. Miki Nakabayashi of Kyoto University are also gratefully acknowledged.

Further, the author wishes to express his heartfelt thanks to his excellent colleagues Mr. Masaru Fujino, Mr. Mikio Geho, Mr. Nobuhiko Tanaka, Dr. Takenori Sekijima, Mr. Takashi Takagi, Dr. Hideto Sato, Mr. Jisaburo Ushizawa (presently at Oxide Corporation) of Murata Manufacturing Co., Ltd., who helped with much of the experimental work and provided useful discussions. The author would like to thank Mr. Gensaku Imae and Mr. Toshihiro Terada of Murata Manufacturing Co., Ltd. for their assistance with precision cutting and polishing of crystals. The author also appreciates the generous support in the compositional, structural, and thermal analyses received from Mr. Haruyuki Yorita, Mr. Toshiyuki Tamura, Mr. Toshikatsu Usuda, Mr. Kenji

Akiyama, Mr. Yasuhiro Motoyoshi, and Mr. Yoshihiro Takase of Murata Manufacturing Co., Ltd.

Heartfelt thanks to all the students and staff of Hirao's laboratory and Miura's laboratory of the Kyoto University for their helpful discussions and excellent assistance.

Finally, the author would like to express his sincere appreciation to his beloved sons Kenji and Shogo who have been a continual source of encouragement for confronting difficult challenges and to his wife, Maya, who supported him in every possible way and helped him keep his life in proper perspective and balance. This dissertation is dedicated to her with deepest gratitude.

Kyoto, Spring 2012

Makoto Kumatoriya